Dissertation

An ex vivo organotypic rat femur slice culture – A novel tool for the investigation of bone regeneration and postnatal endochondral development

Submitted by

Vanessa Etschmaier, M.Sc.

For the Academic Degree of

Doctor of Medical Science (Dr. scient. med.)

at the

Medical University of Graz

Department of Orthopedics and Traumatology

Under the Supervision of

Research Prof. Priv.-Doz. Mag.rer.nat. Dr.scient.med. Birgit Lohberger

2023

Declaration

I, Vanessa Etschmaier, hereby declare that this thesis is my own original work and that I have fully acknowledged by name all of those individuals and organizations that have contributed to the research for this thesis. Due acknowledgement has been made in the text to all other material used. Throughout this thesis and in all related publications I followed the “Standards of Good Scientific Practice and Ombuds Committee at the Medical University of Graz”.

Graz, 9.11.2023 Vanessa Etschmaier

.

Disclosures

Parts of this thesis have been published, submitted or are currently prepared for submission under the terms of the Creative Commons Attribution License (CC BY, https://creativecommons.org/licenses/by/4.0/), which permits distribution, unrestricted use, and reproduction of data, text, or article if the original work is properly cited. All co-authors have agreed to the inclusion of their published data in the dissertation and permission to reproduce illustrations and figures from their own publications has been granted.

1) **Published in Cells** (IF 6.0; 5-year IF: 6,7)

Etschmaier V, et al. "Disruption of Endochondral Ossification and Extracellular Matrix Maturation in an Ex Vivo Rat Femur Organotypic Slice Model due to Growth Plate Injury" in *Cells* vol. 12,13 1687. 22 Jun. 2023, doi:10.3390/cells12131687 [1]

The following co-authors contributed to my published publication

Vanessa Etschmaier [1], Muammer Üçal [1,3], Birgit Lohberger [2], Markus Absenger-Novak [4], Dagmar Kolb [5,6], Annelie Weinberg [2], Ute Schäfer [1]*

[1] Research Unit for Experimental Neurotraumatology, Medical University of Graz, 8036 Graz, Austria.

[2] Department of Orthopaedics and Trauma, Medical University Graz, 8036 Graz, Austria.

[3] Bio-Tech-Med Graz, 8010 Graz, Austria.

[4] Center for Medical Research, Core Facility Imaging, Medical University of Graz, 8036 Graz, Austria.

[5] Center for Medical Research, Core Facility Ultrastructure Analysis, Gottfried Schatz Research Center, Medical University of Graz, 8010 Graz, Austria.

[6] Division of Cell Biology, Histology and Embryology, Gottfried Schatz Research Center, Medical University of Graz, 8010 Graz, Austria

Author Contributions

Conceptualization, V.E., U.S. and A.W.; methodology, V.E., M.A.-N. and D.K.; formal analysis, B.L., M.Ü. investigation, V.E., M.A.-N., D.K.; resources, A.W., and U.S.; writing—original draft preparation, V.E., M.Ü., B.L. and U.S.; writing—review and editing, V.E., M.Ü., B.L., A.W. and U.S.; visualization, V.E.; supervision, U.S.; project administration, A.W. and U.S.; funding acquisition, A.W. and U.S. All authors have read and agreed to the published version of the manuscript.

2) Published in Cells (IF 6.0; 5-year IF: 6,7)

Etschmaier V, et al. "Proton and Carbon Ion Irradiation Changes the Process of Endochondral Ossification in an Ex Vivo Femur Organotypic Culture Model" in *Cells* vol. 12,18 2301. 18 Sep. 2023, doi.org/10.3390/cells12182301 [2]

The following co-authors contributed to the submitted publication

Vanessa Etschmaier [1], Dietmar Glänzer [1], Nicole Eck [1], Ute Schäfer [2], Andreas Leithner [1], Dietmar Georg [3,4] and Birgit Lohberger [1,*]

[1] Department of Orthopaedics and Trauma, Medical University Graz, 8036 Graz, Austria

[2] Department of Neurosurgery, Research Unit for Experimental Neurotraumatology, Medical University of Graz, 8036 Graz, Austria

[3] Department of Radiation Oncology, Medical University of Vienna, 1090 Vienna, Austria

[4] MedAustron Ion Therapy Center, 2700 Wiener Neustadt, Austria

Author Contributions

Conceptualization, V.E., B.L., and U.S.; methodology, V.E., D.G. (Dietmar Glänzer), N.E., and B.L.; formal analysis, B.L.; investigation, V.E., D.G. (Dietmar Glänzer), N.E., and B.L.; resources, A.L. and D.G. (Dietmar Georg); writing—original draft preparation, V.E. and B.L.; writing—review and editing, V.E., A.L., D.G. (Dietmar Georg), and B.L.; visualization, V.E.; supervision, B.L.; project administration, B.L.; funding acquisition, B.L. and D.G. (Dietmar Georg). All authors have read and agreed to the published version of the manuscript.

3) Submitted to the Journal of Bone&Joint Research (IF 4.6)

Etschmaier V, et al. "Ex Vivo Organotypic Bone Slice Culture Reveals Preferential Chondrogenesis After Sustained Growth Plate Injury"

The following co-authors contributed to this manuscript

Vanessa Etschmaier [1], Muammer Üçal [2,3], Birgit Lohberger [1*], Annelie Weinberg [1], Ute Schäfer[2]

[1] Department of Orthopaedics and Trauma, Medical University Graz, 8036 Graz, Austria

[2] Department of Neurosurgery, Research Unit for Experimental Neurotraumatology, Medical University of Graz, 8036 Graz, Austria

[3] Bio-Tech-Med Graz, 8010 Graz, Austria.

Author Contributions

Study design: U.S, A.W, V.E, Data collection and analysis: V.E, M.Ü, and B.L interpretation: V.E, M.Ü, U.S, A.W, B.L and writing the manuscript: V.E, M.Ü, B.L, U.S

.

Acknowledgements

As a doctoral student, I was supported by the CAMed project (COMET-Project 871132) which was funded by the Austrian Federal Ministry of Transport, Innovation and Technology (BMVIT) and the Austrian Federal Ministry for Digital and Economic Affairs (BMDW) and the Styrian Business Promotion Agency (SFG) and the Medical University of Graz through the doctoral school Bone, Muscle, and Joint program.

I would like to extend my heartfelt gratitude to my supervisors: Prof. Ute Schäfer, Prof. Annelie Weinberg, Muammer Üçal, PhD, and ResProf. Birgit Lohberger. Firstly, I wish to express my appreciation to Prof. Ute Schäfer for granting me the invaluable opportunity to conduct my doctoral research within her esteemed research group. I am sincerely thankful to the team at FE Experimental Neurotraumatology, particularly Silke Patz, Gerda Grünbacher, Ulrike Zefferer, and Muammer Üçal, for their consistent guidance and unwavering support. Their presence has been a source of solace and encouragement, especially during challenging times. My heartfelt gratitude extends to all of them.

Secondly, I extend my thanks to Prof. Annelie Weinberg and ResProf. Birgit Lohberger for their mentorship throughout the scientific challenges I encountered, which have undoubtedly contributed to my growth as a scientist. I hold in high regard the collaborative opportunity extended by Birgit and her continuous support, both of which I deeply appreciate.

Thirdly, I acknowledge that my educational journey would not have been possible without the love and unwavering support of my family, my husband's family and friends. Your incredible presence in my life fills me with gratitude, and I am truly blessed to have such continuous support.

Lastly, my deepest appreciation goes to my husband, Martin. Your unwavering support has been the cornerstone of my success. You have been my rock during the toughest moments, providing me with the strength to persevere in the face of challenges. With all my heart, thank you.

Table of Contents

List of Figures

List of Tables

Abbreviations

Acan	Aggrecan
Alpl	Alkaline phosphatase
BAO	Bone-associated osteoclasts
Bmp	Bone morphogenetic protein
c-Cas 3	Cleaved Caspase 3
C-ions	Carbon ions
Col10a1	Type X collagen
Col1a1	Type I collagen
Col2a1	Type II collagen
COMP	Cartilage oligomeric matrix protein
Ct	Cycle threshold
CZ	Calcification zone
DIV	Days in vitro
DPBS	Dulbecco phosphate buffer saline
ECM	Extra cellular matrix
GAG	Glycosaminoglycan
GP	Growth plate
GPI	Growth plate injury
Gy	Gray
H&E	Hematoxylin and Eosin staining
Hh	Hedgehog
HIER	Heat induced epitope retrieval
HRP	Horseradish peroxidase
HZ	Hypertrophy zone
IHC	Immunohistochemistry
Ihh	Indian hedgehog
LET	Linear energy transfer
MMP	Matrix metalloproteinase
Mmp13	Matrix metallopeptidase 13
MSC	Mesenchymal stem cells
Non-IR	Non-irradiated control
Oc	Osteocalcin
Opg	Osteopotegerin
Opn	Osteopontin
Osx	Osterix

OTC	Ex vivo organotypic culture
OZ	Ossification zone
PG	Proteoglycan
PT	Particle therapy
PTHrP	Parathyroid hormone-related protein
PZ	Proliferation zone
Rank	Receptor Activator of Nuclear Factor Kappa-B
RankL	Receptor Activator of Nuclear Factor Kappa-B Ligand
RBE	Relative biological effectiveness
RT	Radiation therapy
Rt	Room temperature
RT-PCR	Real-time polymerase chain reaction
Runx2	Runt related transcription factor 2
RZ	Resting zone
SOBP	Spread-Out Bragg peak
Sox9	SRY box transcription factor
STEM	Scanning transmission electron microscopy
TRAP	Tartrate-resistant acid phosphatase staining
VAO	Vessel-associated osteoclasts
Vegf	Vascular endothelial growth factor

Zusammenfassung

Das postnatale longitudinale Knochenwachstum erfolgt in erster Linie innerhalb der Wachstumsfuge durch die Proliferation und osteogene Differenzierung von Chondrozyten über die endochondrale Ossifikation. Kommt es in Folge von Verletzungen, Krankheiten oder durch Therapiestrategien zu Veränderungen in der Wachstumsfugenorganisation, kann dies zu erheblichen Komplikationen in der Skelettentwicklung führen. Regenerationsprozesse, die von der Wiederherstellung des ursprünglichen Wachstumsfugenzustandes abweichen, können zu erheblichen negativen Komplikationen führen, wie z. B. einem vorzeitigen Verschluss der Wachstumsfuge oder einem Wachstumsstillstand, der zu einer Verkürzung der Gliedmaßen und/oder einer Winkeldeformität führt. Derzeit gibt es keine präventive biologische Behandlung für die Behandlung von pathologischen Prozessen der Wachstumsfuge. Ein Grund dafür ist der noch immer nicht vollständig verstandene pathologische Regenerationsmechanismus, der zu den wachstumsbedingten Problemen führt. Es fehlt unter anderem an neuen, einfach zu handhabenden Forschungsmodellen, die eine Echtzeituntersuchung des pathologischen Regenerationsprozesses ermöglichen.

In dieser Dissertation habe ich ein organotypisches Ex-vivo-Femurmodell (OTC) weiterentwickelt, um pathologische Regenerationsprozesse nach 1) Wachstumsfugenverletzung ähnlich Salter Harris III und IV und 2) Partikelbestrahlung (PT) mit Protonen oder Kohlenstoffionen (C-Ionen) in den MedAustron-Anlagen zu untersuchen. Ich verwendete ein 300 µm dickes OTC und setzte die Kultur jeweils den beiden Versuchsbedingungen aus, mit anschließender in-vitro-Kultivierung für bis zu 15 Tage. Ich führte Elektronenmikroskopie, Genexpressionsanalyse, Lebend-/Totfärbung, histologische Untersuchungen und Immunhistochemie durch und legte Augenmerk auf die postnatalen endochondralen Ossifikationsprozesse.

Bei der Untersuchung der Wachstumsfugenverletzung beobachteten wir Regenerationsprozesse, die mit einer traumabedingten Veränderung der strukturellen Architektur und Organisation einhergingen, sowie eine ausgeprägte Beeinträchtigung der Chondrozytenreifung mit Bevorzugung der Chondrogenese gegenüber der Osteogenese im OTC Modell. Darüber hinaus wurden nach der PT pathologische Regenerationsprozesse beobachtet, die sich durch einen anfänglichen Verlust proliferierender Chondrozyten mit der Bildung von Chondrozytenklustern, eine verringerte Osteogenese und Chondrogenese in Verbindung mit einer Störung der Reifung/Zusammensetzung der extrazellulären Matrix (ECM) auszeichnen.

In beiden Studien sind die mit dem OTC Modell erzielten Ergebnisse mit der In-vivo-Situation vergleichbar, was dieses neue Knochenentwicklungs- und -regenerationsmodell zu einem

leistungsfähigen Werkzeug macht, um die wissenschaftlichen Erkenntnisse weiter voranzutreiben.

Abstract

Postnatal longitudinal bone growth primarily occurs within the growth plate (GP) through the proliferation and osteogenic differentiation of chondrocytes via endochondral ossification. When changes in the GP organization occur due to injuries, illness, or as a result of therapy, this can lead to significant complications concerning the skeletal development. Regenerative processes following sustained injury and illness that diverge from restoring the original state can have significant negative complications such as premature closure of the GP or growth arrest resulting in limb shortening and/or angulation deformity. Currently, no preventative biological treatment is available for the GP pathological processes. One reason is the still no fully understood pathological regeneration mechanism, which leads to the growth-related issues. The lack of new, easy-to-handle research models that allow real-time investigation of the pathological regeneration process is still missing.

In this dissertation, I modified an ex vivo femur organotypic model (OTC) to investigated pathological regeneration processes following 1) GP injury similar to Salter Harris III and IV and 2) particle irradiation with proton or carbon ions (C-ions) at the MedAustron facilities. I utilized a 300 µm thick OTC and exposed the culture to the two experimental conditions, respectively, with subsequent in vitro cultivation for up to 15 days. I conducted electron microscopy, gene expression analysis, live/dead staining, histological examinations, and immunohistochemistry and analyzed key markers of endochondral ossification.

Regarding the GPI investigation, we observed regeneration processes coupled with trauma-induced alteration of structural architecture and organization, as well as a pronounced impairment of chondrocyte maturation with a preference for chondrogenesis over osteogenesis within the ex vivo organotypic GPI model. Moreover, following PT, pathological regeneration processes indicated an initial loss of proliferating chondrocytes with the formation of chondrocyte clusters, reduced osteogenesis and chondrogenesis coupled with a disruption in extracellular matrix (ECM) maturation/composition.

In both studies, the results obtained from the ex vivo femur organotypic model are comparable to the in vivo situation, making this new bone development and regeneration model a powerfool tool to further advance the scientific knowledge.

1 Introduction

1.1 Bone development

Ossification, or osteogenesis, is the process of bone development. Depending on the type of bone, such as long or flat bones, it follows one of the two processes: endochondral (indirect) or intramembranous (direct) ossification. Around the embryonic fifth- or sixth-week, mesenchymal cells begin to condense, forming mesenchymal tissue and differentiate into chondrocytes (endochondral ossification) or osteoblast (intramembranous ossification). During the endochondral ossification, the chondrocytes first establish a hyaline cartilage template that will gradually be replaced by bone. This process takes time and is typically completed postnatally during our mid-twenties [3].

1.1.1 Intramembranous ossification

Intramembranous ossification is the process of direct transformation from mesenchymal stem tissue to bone. When mesenchymal stem cells differentiate to osteoblasts, they begin to produce and secrete an unmineralized collagen-proteoglycan matrix capable of calcium binding, known as osteoid. Once the calcium is bound, the matrix hardens, enclosing the osteoblasts and leading to their differentiation into osteocytes. The continuous production of osteoid contributes to the formation of trabecular/cancellous/spongy bone, which is covered by the fibrous membrane called periosteum. The periosteum houses stem cells and precursor cells that eventually transform into osteoblast and initiate osteoid production. This parallel process result in the formation of different bone layers known as compact/cortical bone [3, 4].

1.1.2 Endochondral ossification

The endochondral ossification requires the formation of a cartilage template from mesenchymal tissue before it is gradually replaced by bone tissue (Fig. 1). Therefore, mesenchymal cells derived from the mesoderm condense and differentiate into chondrocytes. Quick proliferation, coupled with the production and secretion of extra cellular matrix (ECM), follows to form the hyaline cartilage template. The template is encapsulated by a layer of fibrous membrane called the perichondrium. Once the template is completed, chondrocytes in distinct areas, the primary and later the secondary ossification centers, start to undergo hypertrophy. Simultaneously, they begin secreting specific, more mature ECM components such as collagen X (Col10a1) and fibronectin. With the changed ECM, calcification processes begin, which restricts nutrients from permeabilizing to the hypertrophic chondrocytes, leading to their apoptosis. As they undergo apoptosis, they create space for blood vessels to invade the area and expand it further. The invaded blood vessels are further accompanied by osteogenic precursor cells. At the same time, this marks the transition of the perichondrium into the periosteum. The diaphysis is the first to be replaced by bone. It begins with the formation of the so-called periosteal collar, a thick layer of compact bone, which replaces the periosteum. Next, the primary ossification center forms in the middle of the diaphysis, and the cartilage template is replaced by bone from there towards the ends but stops at the metaphysis. At the end of the long bones, called epiphysis, the proliferation and maturation of chondrocytes continue, resulting in ongoing bone elongation. Similar to the primary center, in the middle of the epiphysis, the secondary ossification center forms, resulting in a gradual closure of the growth plate (GP) until we reach skeletally maturity, and the epiphyseal line is the last remnant of bone development [3, 5].

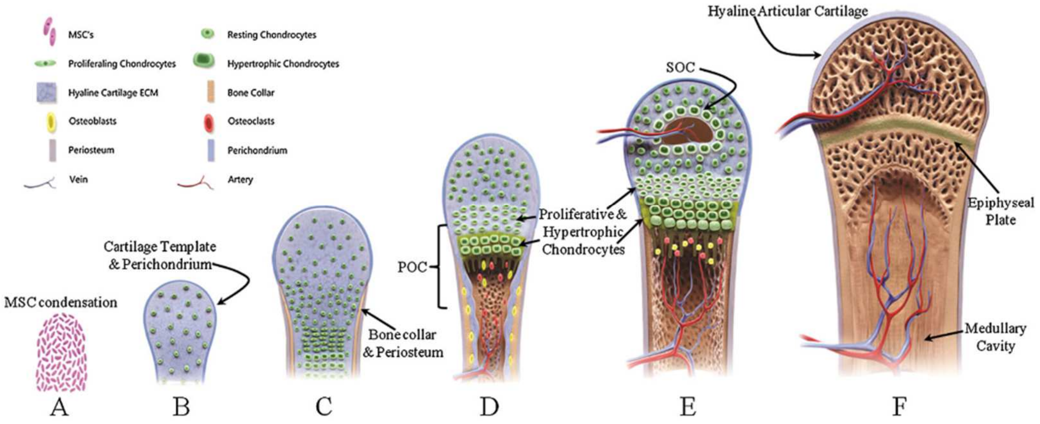

Figure 1. Stages of endochondral ossification. First, mesenchymal stem cells condense (A) and begin to differentiate into chondrocytes and form the hyaline cartilage template by secreting extracellular matrix (ECM) (B). The development of the bone collar follows, establishing the primary ossification center (C), which is then followed by the formation of the epiphyseal growth plate (GP) (D). Subsequently, the secondary ossification center forms (E). Finally, the epiphysis transforms into bone tissue, the growth plate (GP) closes, and the epiphyseal line is the last remnant of bone development (F). Reproduced from [6] with permission to reuse granted by Prof. Fergal J O'Brien.

1.2 Growth plate development

The GP, also known as the active growth zone, sits at the end of long bones, is a highly structured cartilage tissue and measures approximately 800 - 1000 µm in thickness [7]. As bone development and endochondral ossification process, the GP is gradually replaced by bone tissue until we reach full skeletal maturity [3]. The GP consists of chondrocytes in varying states of maturation, which are embedded in the ECM as well as produce it, collaborating harmoniously to facilitate the longitudinal elongation of long bones [8, 9]. Interestingly, the supply of nutrients to chondrocytes occurs through diffusion from the adjacent periosteum, as the GP is avascular and aneural [10]. The varying maturation stages and different composition of the ECM allow the separation of the GP into discrete regions, conventionally identified as the resting zone (RZ), proliferation zone (PZ), hypertrophy zone (HZ), calcification zone (CZ), and ossification zone (OZ) (Fig. 2) [8, 9]. The importance of each zone and the properly orchestrated process of endochondral ossification through these zones was recently studied by Abed and colleagues [11]. They conducted two separate experiments: 1) surgical removal of the PZ and HZ, leaving only the RZ, and 2) surgical removal and placement of the RZ alongside the PZ and HZ. In the first experiment, a proper GP formed in most of their samples, while in some, only the PZ was re-established, and not the rest of the GP. In the second experiment, they observed a 90-degree shift in the orientation of RZ chondrocytes, with these chondrocytes aligning in perpendicular columns to the adjacent surface of the ectopic RZ. Consequently, a complete GP developed perpendicular to the long axis of the bone in a time-dependent manner. However, when analyzing the original GP more closely, two distinct observations were made. Firstly, chondrocytes of the PZ far away from the transplanted RZ did not demonstrate a shift in orientation, illustrating the significance of spatial associations with the RZ. Secondly, chondrocytes adjacent the placed RZ did not undergo hypertrophy, and thus preventing the ongoing ossification of the neighboring PZ cartilage [11].

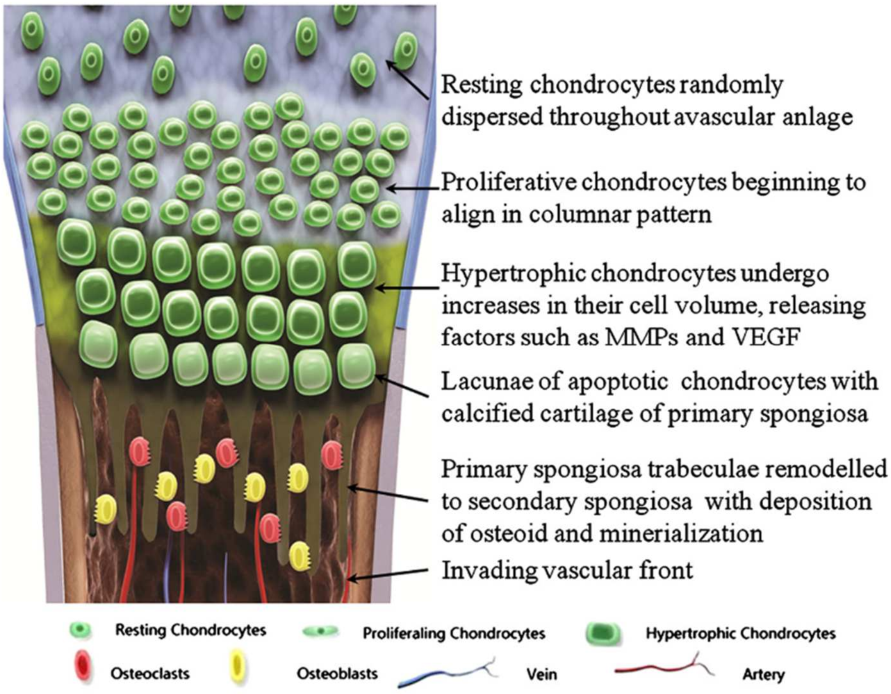

Figure 2. Growth plate (GP) anatomy. The GP is highly organized into distinct zone based on the maturation stage of the chondrocytes. The chondrocytes in the resting zone (RZ) are quiescent and hold a stem cell like population. As they move closer to the metaphysis, chondrocytes proliferate (proliferating zone – PZ), arrange into a columnar pattern, enlarge in cell size and become hypertrophic (hypertrophic zone – HZ). Tissue degradation allows for blood vessels to invade and the transformation into bone tissue takes place. Reproduced from [6] with permission to reuse granted by Prof. Fergal J O'Brien.

1.2.1 Resting zone

The RZ is home of irregularly distributed, mostly quiescent chondrocytes, and it serves various crucial functions that impact the entire GP [8]. It not only possesses stem cell-like characteristics but it is also capable of orchestrating the correct differentiation into proliferative and hypertrophic chondrocytes in a non-cell autonomous manner [12]. Within the RZ, a distinct stem-cell like population expressing parathyroid hormone-related protein (PTHrP$^+$) was observed, responsible for the upkeep of the gradually diminishing pool of proliferating chondrocytes [11, 13]. While the secretion of PTHrP is essential in preserving the proliferation state and preventing the differentiation into pre-hypertrophic state [14], to keep the stem-cell like state, PTHrP$^+$ cells further maintain a Wnt inhibitory environment [15]. Furthermore, the RZ produces a morphogen responsible for guiding the proper orientation and alignment of the proliferating chondrocytes into the columnar position, and a morphogen that prevents the premature terminal hypertrophic differentiation of adjacent PZ chondrocytes, therefore regulating the structural integrity of the GP [11]. Interestingly in the context of GP injury (GPI), a drill hole experiment demonstrated that these PTHrP$^+$ cells are able to migrate toward the injury site and differentiate into osteoblast [13].

1.2.2 Proliferating zone

When the RZ chondrocyte leave their quiescent state, they transition into flat and columnar proliferating chondrocytes [13]. To slow down their differentiation into pre-hypertrophic chondrocytes, the Indian hedgehog (Ihh) – PTHrP feedback loop plays a vital role. Ihh, which is produced by pre-hypertrophic and hypertrophic chondrocytes, induces chondrocyte proliferation and inhibits their terminal transition by stimulating RZ chondrocytes to express PTHrP. Once PTHrP is expressed, it binds to receptors found on proliferating and pre-hypertrophic cells, initiating signaling that slows down their differentiation into hypertrophic cells [14, 16, 17].

1.2.3 Hypertrophic zone

Although the RZ and PZ are necessary for bone elongation, the actual elongation takes place during the hypertrophic maturation of chondrocytes. As the proliferating chondrocytes become pre-hypertrophic and, finally, terminal hypertrophic, chondrocytes increase their cell volume by 10-20-fold, along with a transition of their metabolic and molecular profile. While it was believed that once chondrocyte reach the terminal hypertrophic state, they will undergo apoptosis [18], recent lineage tracing results demonstrated the plasticity of hypertrophic chondrocyte to transdifferentiate into osteoblasts, further contributing to trabecular bone formation [19–21]. Interestingly, transcription factors, especially the SRY box transcription factor (Sox9) or Runt related transcription factor 2 (Runx2), appear to play a pivotal role in process of transdifferentition. The expression of Sox9 limits transdifferentiation [21], while Runx2 is necessary for this process [20]. During early chondrogenesis, mesenchymal stem cells differentiate either toward chondrocytes under the influence of Sox9 or toward osteoblasts under the influence of Runx2 [22]. In the postnatal GP, Sox9 plays a crucial role in sustaining columnar proliferation within the chondrocytes, delaying their progression to the pre-hypertrophic stage, and effectively inhibiting their transdifferentiation into the osteoblast lineage. This is achieved through the downregulation of β-cantenin signaling and suppression of Ruxn2 expression [23]. Runx2 on the other hand, serves as a master regulator for osteoblast and chondrocyte differentiation, driving maturation into the terminal hypertrophic stage and playing a crucial role in cell survival, transdifferentiation, and skeletal mineralization [24–27]. Furthermore, the transdifferentiation of hypertrophic chondrocytes into osteoblasts is now considered an important repair mechanism during bone fracture regeneration [28].

1.2.4 The extra cellular matrix of the growth plate

The hyaline cartilage template gradually matures, mineralizes, and calcifies before being replaced by bone tissue. With the differentiation and maturation of the GP chondrocytes, the ECM also undergoes substantial changes and transitions [3]. The ECM provides essential structural support for chondrocytes [29, 30], and plays an important role in regulating and influencing various aspects of cell dynamics and behavior [31]. This includes critical functions such as cell survival, proliferation, polarity, differentiation, adhesion, and migration. Additionally, the ECM contributes to the mechanical support of tissues and is intricately involved in mechanisms related to growth, regeneration, and the healing process [29–31]. The fundamental importance of the ECM is further highlighted by studies that focus on genetic mutations in the genes responsible for ECM proteins. These mutations typically result in short stature or severe skeletal dysplasia, emphasizing the significance of proper ECM development and maturation during bone elongation [32–34].

The primary components of the GP ECM are collagens, which form a dense network with proteoglycans and other non-collagenous proteins to create the ECM (Fig. 3) [35]. The most highly expressed collagens found in the ECM are the type II (Col2a1), type IX, type XI as well as Col10a1 [34]. Col2a1, the most widespread collagen throughout the epiphysis and GP, is mainly expressed by resting and proliferating chondrocytes [36]. Col2a1 is able to form thick (40 nm) and thin (16 nm) fibrils [37], giving the GP a structural support network, which is favorable for chondrocytes arrangement and other ECM components [38, 39]. Mutations concerning the COL2A1 gene usually result in GP anomalies and chondrodysplasias, which can range from mild skeletal abnormalities to lethal forms [40, 41]. Contrary to the widespread distribution of Col2a1 in the GP, Col10a1 is specifically expressed by hypertrophic chondrocytes and is, therefore, an excellent marker for the HZ. Mutations in the COL10A1 gene can result in skeletal or hematopoietic defects [42, 43], affecting GP organization and disrupting endochondral ossification, resulting in dwarfism or, in severe cases, lethality [44, 45].

In addition to collagens, proteoglycans such as aggrecan (Acan), perlecan, decorin, fibromodulin and lumican, along with non-collagenous proteins like matrilins, cartilage oligomeric matrix protein (COMP), tenascin-C, and link proteins are important ECM components [46–48]. Proteoglycans (PG) are constructed of proteins which are connected to Glycosaminoglycan (GAGs), which are negatively charged polysaccharide chains. While one sugar chain is always either a N-acetylglucosamine or N-acetylgalactosamine the second sugar chain can be either (1) hyaluronan or hyaluronic acid, (2) chondroitin sulfate, (3) dermatan sulfate, (4) heparan sulfate, and (5) keratin sulfate [31]. One of the most abundant PG in the ECM is Acan. Its structure resembles a bottlebrush architecture with a semirigid character [49, 50]. Acan is highly negatively charged through its chondroitin sulfate side chains, which establish an osmotic environment that retains water. This creates a hydrogel like texture, allowing the cartilage tissue to withstand high levels of compression [51]. Mutations in the ACAN gene can result in conditions such as spondyloepiphyseal dysplasia, abnormal craniofacial structures, short limbs or a disorganized GP with augmented expression of other ECM proteins [40, 52, 53].

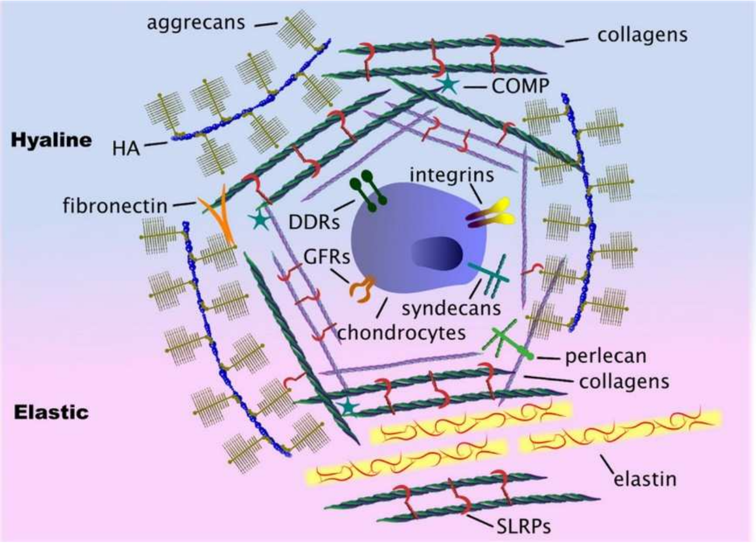

Figure 3. The cartilage extra cellular matrix (ECM) composition. The primary components of the growth plate (GP) ECM are collagens, which form a dense network with proteoglycans and other non-collagenous proteins to create the ECM. Reproduced from [54] with permission was obtained from the Copyright Clearance Center (CCC).[1]

1.2.5 Cartilage tissue degradation and bone tissue formation

As postnatal bone development progresses, the ECM also undergoes transformation in preparation for tissue calcification. This process begins when chondrocytes become

---

[1] https://www.copyright.com/

hypertrophic, increase in cell size, and start producing Col10a1 along with alkaline phosphatase, matrix metalloproteinases (Mmps) [55, 56] and vascular endothelial growth factor (Vegf) [57]. The members of the Mmp family are zinc-dependent proteases with the ability to cleave a range of substrates, including ECM proteins, extracellular non-ECM proteins and cell surface receptors [58]. While Mmp-13 is the primary collagenase expressed for degrading the fibrillar collagen network along with Acan [59, 60], Mmp-9 is responsible in cleaving non-cartilage collagens as well as Acan [59]. This coupled ECM degrading activity is pivotal for removing transverse cartilage septa which would hinder the longitudinal vessel invasion [60]. The importance of Mmp-13 within the GP and long bone development became clear in Mmp-13 null mice studies. The loss of Mmp-13 resulted in profound anomalies concerning the GP cartilage including increased hypertrophic areas, delayed endochondral ossification with development and vascularization of primary ossification centers [61].

Beside the tissue degradation via Mmps, the infiltrating blood vessels promote the recruitment of osteoclasts to further assist the degradation of mineralized cartilage and osteoprogenitors or chondrocytes to initiate the process of osteogenesis. As osteoprogenitors mature or hypertrophic chondrocytes transdifferentiate, they expression of Runx2 signifies the commitment to become pre-osteoblast. Subsequentially, the expression of osterix (Osx) marks the commitment to transition into osteoblast [62]. Mature osteoblast start producing osteoid, which serves as the foundation for building bones, and are characterized by the presence of specific markers such as Osteopontin (Opn) or Osteocalcin (Oc) [63]. Once osteoblast get embedded in the osteoid they form osteocytes, the most abundant cell type in the mature mineralized bone [64].

Besides osteoblast, osteoclasts play a critical role during postnatal long bone development by resorbing bone tissue and thus balancing bone formation. The Osteopotegerin (Opg) - Receptor Activator of Nuclear Factor Kappa-B Ligand (RankL) - Receptor Activator of Nuclear Factor Kappa-B (Rank) pathway, drives the osteoclasts differentiation and activation. This pathway either activates the differentiation and activation of precursor osteoclasts through the binding of RankL to the receptor or inhibits it by the binding of Opg [65, 66].

1.3 Growth plate injury

Injuries in children and adolescents are common. In 2022, 109.700 children under the age of 15 were so seriously injured in Austria that they required medical treatment [67]. Among childhood injuries, bone fractures account for 11% among young children and up to 22% within the age group 15 to18 year-olds. Moreover, boys are significantly more likely to sustain bone fractures compared to girls [68]. In the majority of bone fracture instances, long bones compose the predominant site of injury [69], and in 15 -30% of these injuries, the GP is also affected [70]. In 1963, based on findings derived from experimental studies conducted on animals, Salter and Harris developed a classification system for GPI [71]. Based on the type of GPI and the extent of involvement of the metaphysis and epiphysis, GPIs are categorized into one of five groups: Salter Harris I – V (Fig. 4) [70].

Salter Harris I: When longitudinal force is applied to the bone, it can result in the separation of the epiphysis from the metaphysis. In this scenario, the fracture line typically runs horizontally through the growth plate, often at the HZ, which is the weakest part [70]. The incidence to sustain a Salter Harris I injury is around 5%, with clinically good prognosis [72].

Salter Harris II: In contrast to type I, in Salter Harris II, the fracture line runs horizontally through the GP and extends into the metaphysis at the end [70]. It is the most commonly diagnosed epiphyseal fracture, accounting for 75% of cases. Furthermore, it has favourable prognosis [72].

Salter Harris III: This represent an intra-articular fracture that extend from the epiphysis through the HZ of the GP [70]. Salter Harris III GPI account for 10% of the epiphyseal fractures and have a higher chance of developing growth disturbances than type I and II [72].

Salter Harris IV: This type also represents an intra-articular fracture, with the fracture line running from the articular cartilage, through the epiphysis, the GP and metaphysis. Salter Harris IV also account for 10% of epiphyseal fractures and has higher chances for the developing of growth disturbances than type I and II [70, 72].

Salter Harris V: Salter-Harris V is the rarest category and results from a crush or compression injury to the growth plate, often associated with conditions such as electric shock, frostbite, or irradiation. The force transmitted through the entire epiphysis and growth plate leads to disruption of the germinal matrix, the HZ, and the vascular supply. These injuries account for only about 5% of cases and are typically diagnosed retrospectively. They often have a poor prognosis due to the subsequent growth arrest that may occur [70, 72].

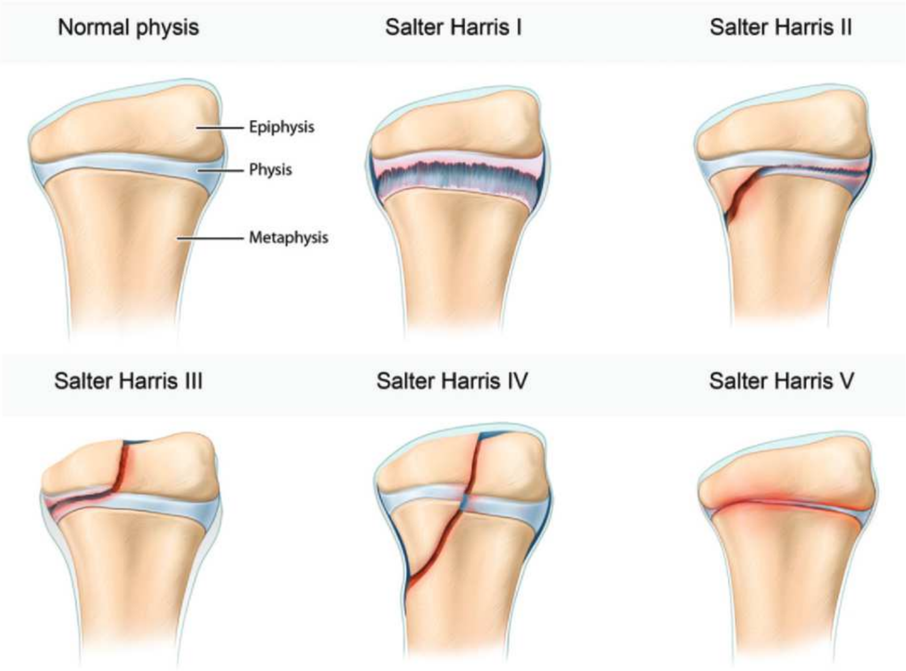

Figure 4. Classification of growth plate injury (GPI) after Salter-Harris. Following the Salter-Harris system, GPI is categorized into one of five Salter-Harris types (I-V) based on the extent of damage and the direction of the injury. As the Salter-Harris type increases in number, the likelihood of encountering complications also increases. Reproduced from [73] with permission to reuse granted by Prof. Chaturvedi as well as permission was obtained through the Copyright Clearance Center (CCC).[2]

1.3.1 GPI regeneration phases

To identify the physiological and pathophysiological regeneration processes following GPI, various animal models were established. The most commonly used animal models in GPI research include mice, rats, rabbits, miniature pigs and sheep models. While the proximal tibia is the most common used bone in GPI studies, the distal femur is the second most used bone. Moreover, excision, drilling, incision and trocar removal are typical methods for introducing a GPI. Notably, all these animal models exhibited bony repair and/or bone growth defects that closely resemble the clinical outcomes observed in humans [74, 75].

---

[2] https://www.copyright.com/

With the aid of these research models, four regeneration phases following GPI are recognized as leading to unwanted bony repair, namely: 1) the inflammatory phase, 2) the fibrogenic phase, 3) the osteogenic phase, and 4) the remodelling phase (Fig. 5) [76, 77].

The inflammatory phase: The immediate reaction to a sustained GPI, days 1 – 3, is the infiltration of the injury site with inflammatory cells such as neutrophils, macrophages/monocytes, and lymphocytes which is coupled with the upregulation of inflammatory cytokines and mediators [76, 78]. Neutrophil depletion studies utilizing neutralizing antibodies, demonstrated an increased area of bone bar together with an upregulation in bone related genes Runx2 and Oc, while cartilage related genes Sox9 and Col2a1 were downregulated [78].

The fibrogenic phase: At days 3 – 7 the fibrogenic phase replaces the inflammatory phase. This phase is marked by the appearance of mesenchymal cells, marked by their vimentin expression [79]. These vimentin-positive cells contains populations ranging from mesenchymal stem cells (MSCs), osteoprogenitor, and chondroprogenitor cells, all playing pivotal roles in the regeneration process [80, 81]. These cells further express certain growth factors such as bone morphogenetic proteins (BMPs), platelet-derived growth factor and fibroblast growth factor 2 as well as the receptors for BMPs and platelet-derived growth factor [76, 82, 83].

The osteogenic phase: After the fibrogenic phase, the osteogenic phase takes over from day 7 onwards. On this day, the first bony trabecular are observed, along with the presence of bone matrix proteins such as Oc and cells immuno-positive for Runx2 and alkaline phosphatase (ALP) [79]. This phase also marks the beginning of bone bridge development [75].

The remodelling phase: On day 14, the first signs of bone remodelling become apparent, characterized by an increased presence of mesenchymal stem cells and osteoclasts within the bony trabecular [83]. Osteogenic-related genes, such as Oc, are highly expressed, while chondrogenic-related genes like Sox9 and Col2a1 are downregulated [76]. Furthermore, an increase in Vegf expression was observed [84]. Vegf is crucial not only for stimulating angiogenesis but also for osteoblast differentiation and osteoclast recruitment [85].

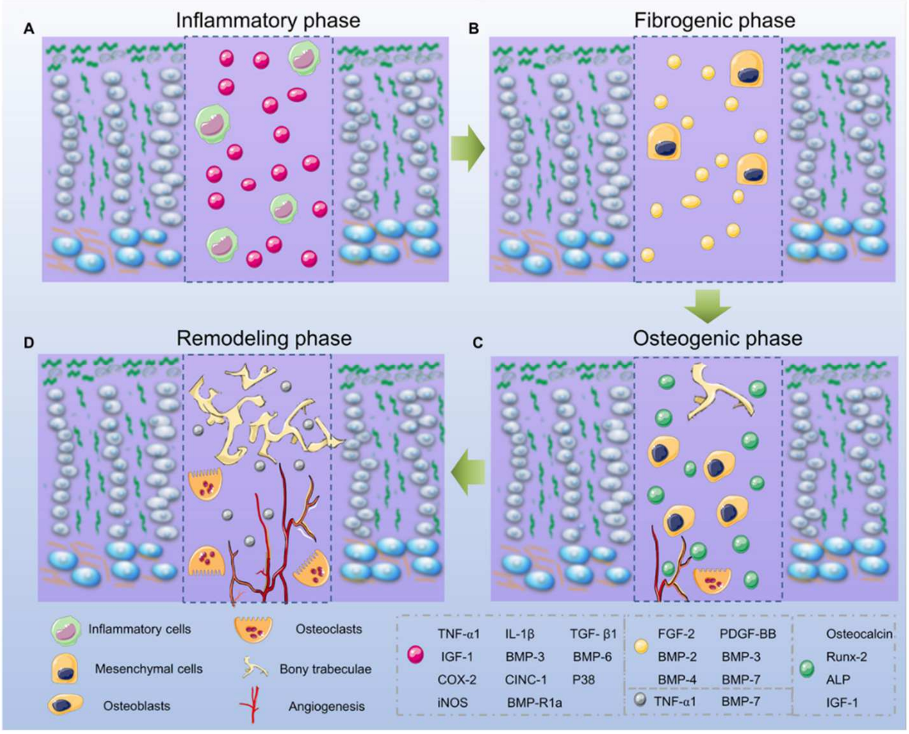

Figure 5. Regeneration phases following growth plate injury (GPI) which lead to bony repair. A) The inflammatory phase, **B)** the fibrogenic phase, **C)** the osteogenic phase, and **D)** the remodeling phase. Reproduced from [86] by Wang, Li, Wang, Bai, Wang, Liu, Bao, Ren, Liu and Wang; licensed under the Creative Commons Attribution License (CC BY).[3]

1.3.1 Current treatment of negative complications following GPI

Regenerative processes following sustained GPI that diverge from restoring the original state can have significant negative complications such as premature closure of the GP or growth arrest resulting in limb shortening and/or angulation deformity. These problems arise from the disruption of the physiological postnatal endochondral ossification process and the formation of bone bridges during injury recovery [87]. Currently, no biological therapy exists to prevent bone bridge formation, as the pathological repair mechanism following GPI, which lead to the growth-related issues, remain unknown. As of today, the only available treatment for complications resulting from a sustained GPI is corrective surgery, which may involve resection of the developed bony bar, the interpositional implantation of materials and limb lengthening [75]. External frames or scaffold such as the Ilizarov frame are used to stabilize and stretch the limb after surgical osteotomy to correct limb length discrepancies. However, due to the

---

[3] https://creativecommons.org/licenses/by/4.0/legalcode.en

severity of this surgery, numerous issues are observed ranging from pin site infections to lengthy lengthening time. A more recent method, however only available for adults, is the utilization of an internal implanted nail named ‘Fitbone’ [75, 88]. On the contrary, bone angulation deformities treatment includes the surgical removal of the bony bar followed by the insertion of interpositional materials, such as fat, muscle, bone wax, cement of polymeric silicone materials named as Langenskiold method [89, 90].

As these surgeries are severe, complex and the success rate is low, the need for a biological treatment option for GPI complications is undisputed. Therefore, more research into the pathological regeneration processes leading to the unwanted bony repair is necessary. This also included the establishment of new GPI models to aid the already undertaken efforts in GPI research.

1.4 Radiation therapy

Radiation therapy (RT) using X-ray radiation, in conjunction with chemotherapy and surgery, is one of the gold standard therapy strategies to address a diverse spectrum of malignancies [91]. When planning a treatment strategy for pediatric patients eventually occurring long-term effects have to be taken under consideration. Two significant concerns arise in this context: first, the potential for developing secondary malignancies, and secondly, their vulnerability to the harmful impact of radiation on the growth and function of normal tissues and organs, which can lead to substantial medical complications and undesirable cosmetic results [92, 93]. Although RT is highly successful in the treatment of those malignancies, it also has negative effects on bone tissue and bone development such as disturbances in bone growth, osteoradionecrosis, pathologic fracture, and radiation-induced neoplasms [94]. Long-term follow-up examinations have revealed significant growth disturbances in pediatric oncology patients treated with RT. These disturbances manifest as chest and rib asymmetry, scoliosis, kyphosis, pain at the radiation site, leg-length inequality, and, in some instances, the emergence of secondary tumors [95, 96]. When comparing photon to proton therapy, a retrospect study found that secondary malignancies occurred in 5.2% of patients treated with protons versus 7.5% of patients treated with photons, with a median duration of follow up of 6.7 years after [97]. Exposing growing bone and the still active GP to radiation results in acute cell death, proliferative arrest, and the accelerated differentiation and maturation of chondrocytes. This results in the loss of a profound amount of chondrocytes, hindering the ongoing bone elongation process [98–100].

1.4.1 Radiation effect on the cellular level

When cellular structures like cells or tissues get hit by radiation direct and indirect effects follow. The most well establish direct effect of radiation is the DNA damage via double or single strand breaks, resulting in an immediate increased rate of apoptosis [101, 102]. Moreover, cells undergoing apoptosis in response to radiation damage typically perish during interphase within a few hours following irradiation, regardless of whether mitosis occurs in the interim. These cells exhibit specific morphological changes, such as the loss of normal nuclear structure and the degradation of DNA, which can be visualized through a characteristic "laddering" pattern on DNA blots [103]. Furthermore, radiation can also induce a G1/S arrest, resulting in the removal of the radiated damaged cells [104] or inhibit mitosis, resulting in a radiation-induced reproductive failure [103]. Indirect effects of radiation include the development of free radicals derived from the ionization itself or via the excitation of the liquid environment of the cells. These free radicals in turn also lead to DNA damage, resulting in cell death [101].

1.4.2 Differences between X-ray and particle irradiation

X-rays fall under the category of short-wavelength electromagnetic radiation, with wavelengths measuring less than 10 nm. They find common use in both diagnostic and therapeutic applications. The gray (Gy) and the rad serve as units for absorbed dose, representing the amount of energy deposited into a given mass of tissue (1 Gy is equivalent to 100 rads). X-rays have the capability to disrupt the normal structure of cellular biochemical compounds through both direct and indirect mechanisms. The detrimental effects of radiation on living organisms can manifest in two primary forms. The first type is dose-dependent and results in immediate clinical damage, often associated with cell death. However, even lower radiation doses can lead to cell damage. On the other hand, stochastic effects emerge some time after exposure and involve genetic harm to the cells. These effects can potentially lead to the development of cancer or the transmission of cell mutations to offspring [105].

Lately, particle therapy (PT) employing protons or heavy ions such as carbon ions (C-ions) represents the latest advancement in radiation therapy (RT), with promising studies suggesting reduced adverse effects and improved patient survival rates following treatment [106]. Contrary to RT, PT exhibit a distinct advantage in terms of dose delivery, characterized by a sharp rise in dose at a precisely defined depth known as the Bragg peak (Fig.6), followed by a rapid decrease beyond this point. This unique property enables the creation of a highly conformal high-dose region, allowing for precise coverage of the target volume while minimizing the impact on adjacent healthy tissues [107]. Moreover, the speed at which charged particles disperse their energy while crossing a material, such as tissue, increases with the particle mass and can be expressed as the linear energy transfer (LET). While protons possess higher LET than photons, their radiobiologic properties are similar [108]. Conversely, C-ions have a higher LET compared to protons, leading to an enhanced relative biological effectiveness (RBE). As a result, C-ion therapy is well-established as the most effective method for treating radioresistant bone tumors [109].

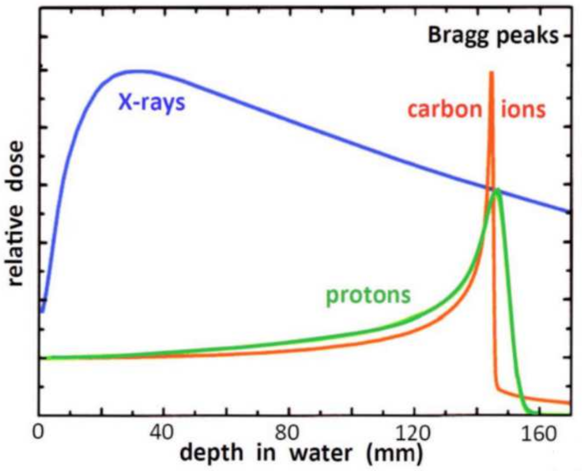

Figure 6. Comparison of the energy deposition of RT vs PT. X-rays (blue line) exhibit high-energy wavelengths from the outset and lose them as they penetrate deeper into the tissue. In contrast, protons (red line) and C-ions (green line) maintain low-energy wavelengths until they reach their defined depth, known as the Bragg peak. At this precise depth, the particles release all their energy into the specific tissue, thus protecting the surrounding tissues both before and after this point. Reproduced from [110], licensed under the Creative Commons Attribution License (CC BY).[4]

1.4.3 MedAustron proton and C-ions irradiation in vitro set-up

In order to investigate the effect proton and C-ions have on biological samples, Lohberger at al. together with the MedAustron facilities established the dose and LET distribution for these conditions in the novel water phantom designed for in vitro experiments (Fig. 7). These findings include a comparative analysis of measured and calculated dose values. For the in vitro investigations, they found proton energies ranging from 66.5 to 135.6 MeV were necessary to achieve clinically relevant target size and isoeffective range depth. When the measurement

---

[4] https://creativecommons.org/licenses/by/4.0/

flask was placed at the midpoint of the Spread-Out Bragg Peak (SOBP), variations in proton dose-averaged LET remained insignificant, with a consistent value of 2.9 keV/μm (Fig. 7A). The positioning error, with a reproducibility of 0.55% on the dose measurements, was determined to be 300 μm. In contrast, for carbon ions, the LET values were higher, and the LET distribution exhibited a steeper profile. Carbon ions with energies ranging from 170 to 230 MeV/u presented a LET range between 50 and 150 keV/μm. Even at the central position within the carbon ion SOBP, the impact of positioning errors remained less than 0.5%, with an LET value of 55.2 keV/μm (Fig. 7B). The LET values were determined through Monte Carlo calculations and were directly obtained from the treatment planning system. For reference, photon irradiation was carried out using a 200 kV beam generated by a YXLON unit. In radiobiological experiments, the following filtration setup was employed: 3 mm of beryllium, 3 mm of aluminum, and 0.5 mm of copper. The cell layer was positioned at a distance of 40 cm from the exit window of the beam source [111].

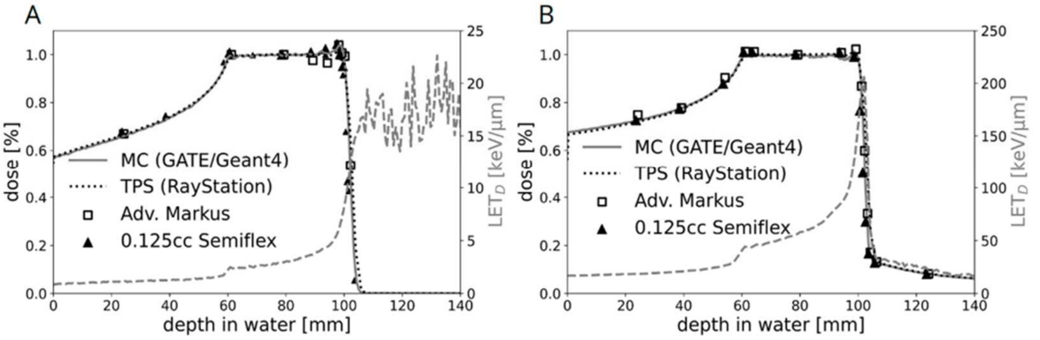

Figure 7. The percentage depth dose curves for (A) proton and (B) C-ion Spread-Out Bragg Peaks (SOBP) utilized in cell irradiation are presented. Notably, an excellent agreement was observed between the predicted dose distributions generated by the treatment planning system and Monte Carlo simulations. The respective Linear Energy Transfer (LET) spectrum demonstrates an increase with depth in water. C-ions exhibit significantly higher LET values compared to protons, as evident from the contrasting scales on the mirrored y-axis (25 keV/μm versus 250 keV/μm). In the case of protons, the LET beyond the fall-off region lacks physical relevance, as no particles are delivered beyond this depth. Reproduced from [111], permission to reuse granted by Prof. Birgit Lohberger, licensed under the Creative Commons Attribution License (CC BY).[5]

---

[5] https://creativecommons.org/licenses/by/4.0/

1.5 Ex vivo models

To study the regeneration of GPI, conventional 2D cell culture, utilizing primary or immortalized cells is a fast and cost-effective way to gain first insights. However, translating findings obtained in vitro to the actual in vivo situation is often challenging [112]. To understand the intricate architecture of bone tissue, developmental processes and endochondral ossification, animal studies are still the gold standard, because the interaction of the different cartilage and bone tissue cell types and changes in ECM composition cannot be mirrored in vitro. With regard to GPI, currently used animal models include mice, rats, rabbits, miniature pigs and sheep models [74, 75]. Alongside the ethical concerns, animal models come with significant costs, demand a substantial workforce, and large sample size [113–115].

Beside the discrepancy between conventional 2D cell culture and animal experiments, the 3R initiative to ‘reduce, refine and replace’ animal models in scientific research accelerated the development of 3D models such as ex vivo organotypic cultures (OTCs). These models were developed to achieve an in vivo-like 3D structure with characteristic biological function. These models replicate in vivo conditions by accurately reproducing specific cellular behaviours, morphological changes, cell maturation, differentiation, and migration within the tissue microenvironment [116]. Derived from whole organ cultures, OTCs offer better supply of nutrients and metabolites, achieving a longer in vitro survival of ex vivo tissue. The term 'organotypic' was first used in a report from 1954 on the differentiation of an embryo's eye from a chicken. Shortly thereafter, reports of organotypic cultures from lung, heart , intestine and the CNS tissue followed [117]. With advances in cultivation techniques, such as the semipermeable membrane technique and the roller tube technique, organ slices with a thickness of 100 to 500 µm remained viable for several weeks [113, 118]. Bone with its hard calcified tissue nature and the complex architecture remained challenging to utilize in an OTC setting [119, 120]. Recently, OTC for linear bone growth studies (mouse metatarsal culture), bone and cartilage developmental mechanisms (mouse femoral head culture) or bone responses to mechanical loading (bovine trabecular core culture) were developed [118, 121, 122]. Sriveena et al. established a 300 µm thick distal femur OTC from 5-day old Sprague Dawley rats which demonstrated to mimick the in vivo cellular transitions and endochondral microenvironment during the 15-day in vitro cultivation period [118].

The establishment of such models play a pivotal role in bridging the gaps in our current understanding of GPI pathology and therapeutics, ultimately contributing to the advancement of medical knowledge and the enhancement of patient care. These models provide convenient access to various cell types, enable real-time imaging of physiological and pathophysiological endochondral processes, and facilitate straightforward treatment or modification during in vitro cultivation. These qualities make ex vivo models ideal candidates for further enriching scientific knowledge.

1.6 Hypothesis and Aims of this dissertation

Postnatal longitudinal bone growth primarily occurs within the GP through the proliferation and osteogenic differentiation of chondrocytes within the growth plate, in a process termed endochondral ossification [3]. When changes in the GP organization occur due to injuries, illness, or as a result of therapy, this can lead to significant complications concerning the skeletal development. Regenerative processes following sustained injury and illness that diverge from restoring the original state can have significant negative complications such as premature closure of the GP or growth arrest resulting in limb shortening and/or angulation deformity. These problems arise from the disruption of the physiological postnatal endochondral ossification process and the formation of bone bridges during injury recovery. Currently, there is no treatment to prevent bone bridge formation, as the pathological repair mechanism following GPI, which lead to the growth-related issues, remain unknown [87].

Hence, the aim of this dissertation was to examine the underlying physiological and pathological changes in the GP within an ex vivo bone culture following two distinct experimental conditions:

1) The first condition involved inducing a GPI characterized by a fracture extending through the entire GP, the metaphysis, and reaching into the bone marrow cavity, closely resembling Salter Harris III and IV type fractures.
2) The second condition entailed exposing the ex vivo bone culture to a single 8 Gy proton or C-ions irradiation.

The objectives of this dissertation were to assess how the two types of injuries impact the physiological postnatal GP development and our investigation will provide insight into the specific mechanisms and alterations in cellular and tissue responses within the ex vivo bone culture setting.

2 Material and Methods

2.1 Preparation and culturing of organotypic cultures (OTC)

To prepare the OTC's, the method published by Srinivasaiah et al. [118] was modified. Femurs from four-day-old postnatal Sprague Dawley rats (12.0 g +/- 2.1 g) were harvested immediately after decapitation and washed with ice-cold Dulbecco phosphate buffer saline (DPBS) (Invitrogen, Waltham, USA). The femurs were then placed in molten agar, which was poured into pre-cooled stainless steel mold (Sakura, Tokyo, Japan) and placed on ice to form an agar block. The agar block was adhered to a sample plate using cyanoacrylate glue for tissue culture (Roti® coll 1; Carl Roth, Karlsruhe, Germany). After calibration of the VT1000 Leica vibratome (Leica Biosystems, Wetzlar, Germany) according to the manufacturer's instructions, 300 µm thick coronal sections were made under buffered conditions using ice-cold 1x DPBS and a stainless steel razor blade (Gillette Procter & Gamble, Boston, USA) at an amplitude of 1.5 mm and a section speed of 0.06 mm/s with a steady blade angle. To mimic a Salter-Harris type III and IV GPI, a 2 mm razor blade was used to cut through the distal GP and metaphysis of the left femur. Slices from the right femur of the same animal were not injured and served as controls. OTC's were then briefly washed in Minimum Essential Medium Eagle (Sigma-Aldrich, St. Louis, USA) containing penicillin (100 U/mL) and streptomycin (100 µg/mL) (Invitrogen) and transferred to 6-well plate with a Millicell cell culture insert of 30 mm with a pore size of 0.4 µm (MERK KGAA, Darmstadt, Germany). Osteogenic medium supplementing MEM with 5 % horse serum (Invitrogen), 1 % penicillin/streptomycin, 1x Insulin-Transferrin-Selenium (Gibco, Invitrogen), 100 µm ascorbic acid (Sigma-Aldrich), 10 mM β-glycerophosphate (Sigma-Aldrich), 10 nM dexamethasone (STEMCELL Technologies, Vancouver, Canada), and 0.01 µg/ml TGFβ-3 (Invitrogen) was added to each well. 500 µl of the medium was replaced daily with fresh medium. The 6-well plates were incubated at 37° C with 5 % CO_2 in a humidified atmosphere. OTC's were harvested and post processed at the day of preparation 0, 1, 3, 7, and 15 days of in vitro cultivation (DIV).

2.2 Ethical statement

Male and female adult Sprague Dawley rats were obtained from Charles Rivers, housed and bred under standard conditions with 12h:12h light-dark cycle and ad libitum access to food and water in the animal facility of Biomedical Research at the Medical University Graz in accordance with §25 of Animal Testing Act 2012.

2.3 Live and Dead staining

Utilizing vital fluorescent dyes to stain and visualize cells constitutes a versatile and commonly employed method within the field of cell biology. This technique enables the differentiation between viable and non-viable cells through a dual staining process. Viable cells are identified by their green fluorescence due to the presence of intracellular esterase activity, utilizing calcein-AM, while non-viable cells exhibit red fluorescence due to compromised plasma membrane integrity, as indicated by ethidium homodimer-1 staining in red fluorescence [123].

Cultivated but unfixed OTC's were rinsed in 1x DPBS and immersed in a live/dead staining solution for 40 minutes (min) containing 2 µM calcein acetoxymethyl and 4 µM ethidium homodimer-1 (Gibco) in 1x DPBS (Gibco) containing calcium and magnesium. OTC’s which were submersed in 1:1 70% ethanol:DMSO for 60 min represented dead tissue and served as negative controls. After exposure to the staining solution, OTC’s were washed three times with 1x DPBS before being transferred to a 6-well plate with little 1x DPBS to avoid dehydration. Confocal laser imaging was performed using a Zeiss SM 510 microscope (Carl Zeiss Microscopy GmbH, Jena, Germany) under a 10x objective with an excitation wavelength of 488 nm and 543 nm and an open pinhole. Sections were observed on 0, 1, 3, 7, and 15 DIV. Dead cells within the injury area were quantified using the maximum projection image and a fix threshold (21-255) and the ZM 2009 software (Zen 2009; Carl Zeiss Microscopy GmbH).

2.4 Electron microscopy

Electron microscopy allows for the visualization of cells and tissue at super low resolution. This method utilizes an electron beam instead of a light which moves over the ultrathin tissue section. This grants for the exploration of the intricate details of tiny structures and particles [124].

OTC’s were fixed for 120 min in 2.5 % (wt/vol) glutaraldehyde (Carl Roth) and 2 % (wt/vol) paraformaldehyde (PFA, MERK KGAA) in 0.1 M cacodylate buffer (Sigma-Aldrich) with a pH of 7.4. Next, post-fixed for 2 h at room temperature (Rt) in 1 % (wt/vol) osmium tetroxide (Sigma-Aldrich) was followed by dehydration using a graded series of alcohol. OTC’s were infiltrated with ethanol and TAAB epoxy resin (pure TAAT epoxy resin; TAAB Berks, UK) and replaced in TAAB epoxy resin for 8 h, transferred into embedding molds, and polymerized at 60° C for 48 h. Ultrathin bone sections with a thickness of 70 nm were prepared utilizing a UC 7 Ultramicrotome (Leica Biosystems) and stained with lead citrate (Sigma-Aldrich) for 5 min and platin blue (Sigma-Aldrich) for 15 min. The electron micrographs were captured using a Tecnai G2 transmission electron microscope (FEI, Eindhoven, Netherlands) with a Gatan ultrascan 1000 CCD charged couple device (CCD) camera (–20° C), and the acquisition software Digital Micrograph (Gatan Inc., Pleasanton, USA). The acceleration voltage was 120 kV.

2.5 Tissue processing for histological and immunohistochemistry evaluations and analyzes

For histological evaluation, cultured OTC's were fixed overnight at 4° C in 2 mL 4 % PFA (MERK KGAA) in DPBS (GIBCO) without decalcification. Next, fixed OTC's were processed by a Sakura Tissue Processor VIP 5E-F2 processor (Sakura) and finally embedded in paraffin (see detailed protocol in Table 1). Serial sections of 5 µm thickness were prepared using an HM 360 Rotation microtome (Hyland Scientific GmbH, Berlin, Germany) and mounted onto Superfrost^{TM} Plus Adhesion slides (Carl Roth) and put on a heating platform (42° C) to dry. For each histological and immunohistochemical (IHC) staining, three sections at different depths of the dorso-ventral axis of the OTC’s were used in chronological order to ensure accuracy and reliability of the gained data. All experiments were performed at least 3 times.

Table 1. Detailed tissue processing protocol used within the Tissue Tek-VIP to process the paraformaldehyde fixed OTC into paraffin blocks.

Step	Reagent	Con (%)	Time (h)
1	Formalin	6	01:00
2	Formalin	6	01:00
3	Ethanol	70	01:00
4	Ethanol	80	01:00
5	Ethanol	96	01:00
6	Ethanol	96	01:00
7	Ethanol	100	01:00
8	Ethanol	100	01:00
9	Tissue Clear		01:00
10	Tissue Clear		01:00
11	Paraffin		01:00
12	Paraffin		01:00

13	Paraffin	02:00
14	Paraffin	02:00
		Total 16:00 h

Histological and IHC staining’s required sufficient de-paraffination and rehydration before the staining process. The detailed protocol for these steps can be found in Table 2.

Table 2. De-paraffination and rehydration steps performed before each histological and immunohistochmistry (IHC) staining.

Step	Reagent	Con (%)	Time (h)
0	60° C		Over night
1	Xylol		00:10
2	Xylol		00:10
3	Xylol:Ethanol	100	00:05
4	Ethanol	100	00:05
5	Ethanol	90	00:02
6	Ethanol	70	00:02
7	Aqua dest.		00:02
8	Aqua dest.		00:02
			Total 00:38 h

2.6 Histological staining techniques

To qualitatively examine tissue sections using light microscopy, various dyes with distinct affinities for tissue, cellular, or extracellular matrix components are employed, alongside specific techniques. The choice of dye and protocol determines the visualization achieved: from depicting tissue morphology (Hematoxylin and Eosin (H&E)) to revealing tissue composition such as collagens, proteoglycans, or mineralization (Movat-Pentachrome, Safranin O-Fast Green, Alizarin Red S). Additionally, specific cell types can be stained by targeting their respective enzyme activities, as seen with tartrate-resistant acid phosphatase (TRAP) staining [125]. All staining´s were performed on a minimum sample size of n ≥ 3 animals per time point and 3 technical replicates.

2.6.1 Hematoxylin and Eosin staining (H&E)

For morphological examination, the rehydrated sections were immersed in Mayer's hematoxylin (Gatt-Koller, Absam, Austria) for 3 min, followed by a 10-minute rinse under warm running tap water. Subsequently, they were briefly washed in distilled water and 95 % ethanol before being stained with eosin (Gatt-Koller) for 1 min. The stained sections were then dehydrated in a series of alcohols of increasing concentration for 2 min each, culminating in a double wash with xylene. Finally, the sections were mounted using Rotimount (Carl Roth).

This stain results in nuclei and calcified material stained in blue or dark-purple, while cytoplasm and extracellular matrix such as collagen will be stained in up to five shades of pink [126].

2.6.2 Movat-Pentachrome staining

To assess tissue composition and endochondral ossification during in vitro cultivation, de-waxed and rehydrated sections were stained with Movat-Pentachrome staining. Rehydrated sections were stained with a 0.1 % solution of Alcian blue (Carl Roth) (20 min at 56° C and 10 min at RT) before stabilizing in 10 % alkaline ethanol (Carl Roth) (5 min). Next, staining with Weigert's iron hematoxylin (A+B 1: 1, Carl Roth) (10 min) and brilliant crocein (Sigma-Aldrich) - acid fuchsin (Carl Roth) (10 min) followed. A quick rinse in 0.5 % glacial acetic acid (Thermo Fisher Scientific Inc.) was followed by differentiating with 5 % phosphotungstic acid (Carl Roth) (20 min). Lastly, Gatinais saffron staining (Chroma-Waldeck Gmbh&Co. KG, Münster, Germany) (60 min) finished the protocol with subsequent clearing in Roticlear (Carl Roth) and mounting with Rotimount (Carl Roth). Between each staining step sufficient washing steps under running tap water and aqua destillata were conducted. Table 3 holds the recipes for the mentioned staining solutions and buffers.

This staining results in structures being stained as follows: cell nuclei (black), cytoplasm (reddish), elastic fibers (red), collagen connective tissue (light yellow), mineralized tissue/bone (dark yellow) and mineralized cartilage (dark green-blue) [127, 128].

Table 3. Preparation of staining solutions and buffers for Movat-Pentachrome staining.

5 % Alcoholic Hematoxylin		
Hematoxylin	12.5 g	Carl Roth
100% Ethanol	fill up to 500 mL	MERK KGAA

10 % Ferric Chloride		
Iron(III)-Chloride	50 g	Carl Roth
Deionized water	fill up to 500 mL	

Verhoeffs´s Iodine Solution		

Iodine	2 g	Carl Roth
Potassium Iodine	4 g	Carl Roth
Deionized water	fill up to 100 mL	

Verhoeffs´s Elastic Stain Working Solution

5 % Alcoholic Hematoxylin	100 mL	
10 % Ferric Chloride	50 mL	
Verhoeff´s Iodine Solution	50 mL	

2 % Ferric Chloride Differentiating Solution

10 % Ferric Chloride	100 mL	
Deionized water	fill up to 500 mL	

5 % Sodium Thiosulfate

Sodium thiosulfate pentahydrate	25 g	Sigma Aldrich
Deionized water	fill up to 500 mL	

3 % Glacial Acetic Acid

Acetic acid glacial	15 mL	Thermo Fisher Scientific
Deionized water	fill up to 500 mL	

1 % Alcian Blue Stock

Alcian blue 8 GS	5 g	Carl Roth, C.I. 74240
Deionized water	485 mL	
Acetic acid glacial	15 mL	Thermo Fisher Scientific

Crocein Scarlet Acid Fuchsion Stock

Solution A:		
Crocein Scarlett	0.5 g	Sigma Aldrich, C8822
Deionized water	497.5 mL	
Glacial Acetic Acid	2.5 mL	Thermo Fisher Scientific
Solution B:		
Acid Fuchsin	0.1 g	Carl Roth, C.I. 42685
Deionized water	99.5 mL	

Glacial Acetic Acid	0.5 mL	Thermo Fisher Scientific

use 8 parts of Solution A + 2 parts of Solution B

5 % Phosphotungstic Acid Solution

Phosphotungstic acid hydrate	25 g	Carl Roth
Deionized water	fill up to 500 mL	

Alcoholic Saffron Solution

Saffron du Gatinais	1g	Chroma Waldeck
Pure ethanol	fill up to 100 mL	MERK KGAA

Extract for at least 48 h in a + 60° C oven under airtight conditions and store at + 4° C

1 % Acetic Acid Solution

Acetic acid glacial	5 mL	Thermo Fisher Scientific
Deionized water	fill up to 500 mL	

2.6.3 Safranin O-Fast Green staining

To analyze proteoglycan composition, de-paraffinization and rehydration, sections were stained with Weigert's iron hematoxylin solution for 10 min (see Table 4) and washed under running tap water for another 10 min. The procedure continued with 0.1 % fast green stain (F7252, Sigma-Aldrich) for 5 min, differentiation in a 1 % acetic acid solution (15 seconds (sec), and final staining with a 0.1 % Safranin O (C.I. 50240, Carl Roth) solution for 5 min. Lastly, dehydration was accomplished by 2 min in 95 % ethanol, 100 % ethanol and xylen, with two changes of each step. Finally, sections were mounted with Rotimount (Carl Roth).

Safranin O has an affinity for glycosaminoglycans, and areas of positive staining indicate the presence of proteoglycans (PG) in cartilage [129]. Proteoglycan positive staining was indicated by red staining, nuclei are stained black and the background will be stained green [130].

Table 4. Recipe for Weigert’s Hematoxylin staining solution.

Weigert’s Hematoxylin

Stock solution A		
Hematoxylin	1 g	Carl Roth

95% Ethanol	100 mL	MERK KGAA
Stock solution B		
29% Ferric chloride in water	4 mL	Sigma-Aldrich
Distilled water	95 mL	
Hydrochloric acid, concentrated	1 mL	Carl Roth

2.6.4 Alizarin red S staining

Alizarin Red S staining is used to identify calcium deposits within the OTC’s. Deparaffinized and rehydrated sections were stained in 40 mM Alizarin red solution (pH 4.1; Alizarin Red S C.I. 58005, Carl Roth) for 2 min and dehydrated in acetone (MERK KGAA) and acetone-xylene solution (1:1), for 20 dips each. The sections were then cleared in Roticlear (Carl Roth) (2 x 3 min) and mounted with Rotimount (Carl Roth).

Here, Alzarin Red S and calcium form a complex in a chelation process which produces a bright red stain [131].

2.6.5 Tartrate-resistant acid phosphatase (TRAP) staining

Deparaffinized and rehydrated sections were placed in a 0.2 M acetate buffer (pH 4.5) that contained 50 mM tartaric acid (Sigma-Aldrich) and 0.2 M sodium acetate trihydrate (Sigma-Aldrich) at RT for a duration of 20 min. Next, slides were put into the staining solution and incubated at 37° C for 2 h. The sections were washed with distilled water and counterstained using Mayer's hematoxylin for 12 sec, followed by differentiation with a 1 % Ammonium Hydroxide solution (10 dips). Finally, the sections were washed briefly with distilled water and mounted using Aquatex (MERK KGAA). The recipes for these procedures can be found in Table 5.

Active osteoclasts express tartrate-resistant acid phosphatase (TRAP) which removes a phosphate from the napthol AS-BI phosphate substrate which in turn forms a complex with the diazoniuzm salt appearing as red precipitate. Therefore, the red staining correlates with the number of active osteoclasts [132].

Table 5. Preparation of staining solutions and buffers for TRAP staining.

Acetate Buffer

50 mM Tartartic acid L(+)	7.5 g	Sigma-Aldrich
0.2 M Sodium acetate trihydrate	27.22 g	Sigma-Aldrich
Deionized water	fill up to 1 L	

Staining solution

Acetate Buffer	1000 mL	
Napthol AS-MX Phosphate	0.5 g	Sigma-Aldrich
Fast Red	1.1 g	Sigma-Aldrich

Ammonium Water

Ammonium hydroxide	0.625 mL	Carl Roth
Deionized water	fill up to 1 L	

2.7 Immunohistochemistry (IHC)

In addition to histological staining methods, IHC is frequently utilized to depict the spatial arrangement of proteins within cells or the ECM. IHC relies on the targeted binding of antibodies (such as anti-protein Ki67) to their corresponding antigens (protein Ki67). Moreover, this technique facilitates not only qualitative data but also quantification, enabling measurements like positive cell count or positive pixel count [133, 134]. To gain further knowledge of the distribution of extracellular matrix proteins, chondrogenesis and osteogenesis markers, IHC was performed with the kit Ultra Vision LP/HRP rabbit/ mouse (Epredia, Michigan, USA), which included: protein block, primary antibody enhancer and the horseradish peroxidase (HRP) reagent. After deparaffinization and rehydration, sections were treated with either 1 mM EDTA pH 8.0 and a decloacking chamber (95° C, 10 min) or 10 mM + 0,05 % Tween-20 Sodium citrate buffer pH 6.0 and a 60° C over night water bath for antigen retrieval (HIER). Hydrogen peroxidase (MERK KGAA) and protein block steps and subsequent incubation with the primary antibody over night at 4° C followed. On mouse origin primary antibodies, a bridging step (primary antibody enhancer) was performed, before all sections were treated with HRP-enzyme with subsequent development of the positive staining with AEC (DAKO, Agilent, Glostrup, Denkmark) and counter staining with hematoxylin (Gatt-Koller). The optimized steps of the IHC protocol for each antibody can be found in Table 6. At least three biological replicates and three sections per replicate were stained for analysis. Recipes for IHC buffers can be found in Table 7.

Primary antibodies included: Ki67 (Abcam, Cambridge, UK), Acan, Sox9, cleaved Caspase 3 (Asp175; c-Cas3), Runx2, Osx (Sp7), Opg (Tnfrsf11b), Col2a1, Col10a1, Opn (Spp1, Novus Biological, Minneapolis, USA), Bmp2 and Vimentin (Santa Cruz Biotechnology, Dallas, USA).

Table 6. Detailed information of used antibodies with respective IHC protocol.

Host	**1st antibody**	**Company**	**Ref. Num.**	**HIER**	**Dilution**	**H_2O_2 block [min]**	**Protein block [min]**
rabbit	**Ki67**	Abcam	ab16667	EDTA	1:200	30	25
rabbit	**Acan**	Abcam	ab36861	EDTA	1:300	30	35
rabbit	**Sox9**	Abcam	ab26414	EDTA	1:300	25	40
rabbit	**c-Cas3**	Abcam	ab2302	EDTA	1:200	25	20
rabbit	**Runx2**	Abcam	ab236639	EDTA	1:100	25	35
rabbit	**Osx**	Abcam	ab209484	EDTA	1:100	20	20
rabbit	**Opg**	Abcam	ab73400	EDTA	1:250	20	15
mouse	**Col10a1**	Invitrogen	MA14-9771-82	EDTA	1:100	10	25
mouse	**Col2a1**	Invitrogen	MA5-12789	Sod.-Cit.*	1:100	25	25
mouse	**Opn**	Novus Biologicals	NB110-89062	Sod.-Cit.*	1:250	20	15
rabbit	**Bmp2**	Invitrogen	PA5-85956	Sod.-Cit.*	1:100	30	40
rabbit	**Vimentin**	Santa Cruz	Sc-5565	Sod.-Cit.*	1:250	10	15

*Sod.-Cit. = Sodium-Citrate

Table 7. Recipes for HIER buffer reagents used within the IHC protocol.

10 X TBS

Trizma Base	121 g	Sigma Aldrich
Deionized water	fill up to 500 mL	
Adjust pH to 7,4 with about 50 ml 37% HCl		
Deionized water	fill up to 2 L	

1 X TBS-T

10 X TBS	100 ml	
Triton X-100	250 µl	Sigma Aldrich
Deionized water	fill up to 1 L	

EDTA buffer pH 8.0

EDTA	0.37 g	Sigma Aldrich
Deionized water	fill up to 1 L	

Sodium citrate buffer pH 6.0

Sodium citrate tribasic dehydrate	2.94 g	Sigma Aldrich
Deionized water	fill up to 1 L	
Tween-20	500 µL	MERK KGAA

2.8 Image Quantification

First, whole object slides were scanned using the Aperio ScanScope (Leica Biosystems). Subsequently, images were generated using the Image Scope software (v12.4.0.50.43, Leica Biosystems) and Photoshop (24.3, Adobe, San Jose, USA). Quantitative analyses were conducted using ImageJ (v1.53f51) (National Institutes of Health, Bethesda, USA) (Fig. 8). Briefly, images were initially split into Red-Green-Blue channels using the preinstalled Deconvolution setting AEC-H. The red channel was then converted into a grayscale image (8-bit). Subsequently, an automated threshold process was used to explicitly eliminate the background from the positive stained cells followed by a positive particle count or positive cell count. This was performed for the proximal epiphysis of at least 3 sections per OTC and for at least 3 biological replicates (animals). Data was statistically analysed with IBM SPSS Statistic 26 (version 6, New York, USA) and graphs were created by GraphPad InStat software (GraphPad Prism 9.3.1 (471), Boston, USA) (see 2.10 Statistical Analysis).

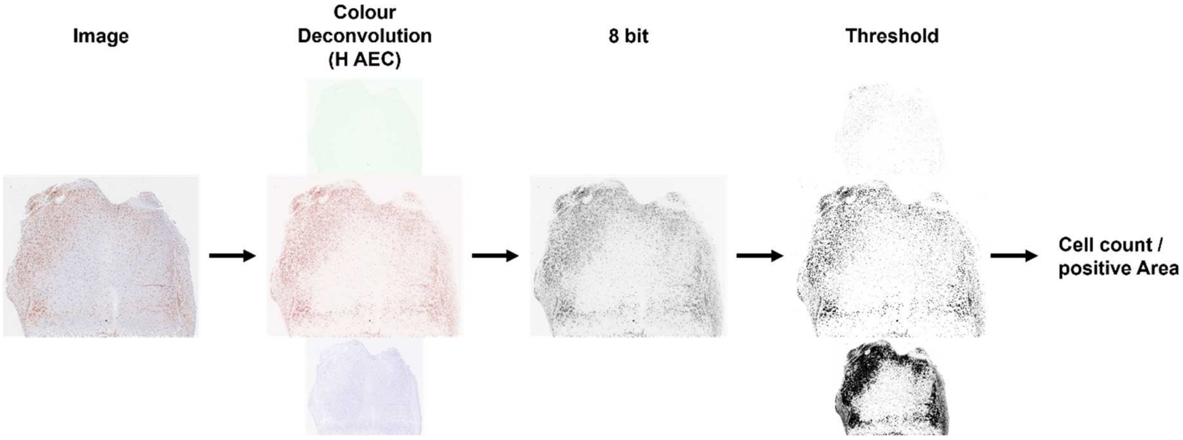

Figure 8. Schematic overview of the image quantification process. Proximal epiphysis were truncated at the transition from the hypertrophic to the mineralization zone. This was followed by colour deconvolution (H AEC) and transformation of the Red channel image into an 8 bit image. Next, optimal threshold was identified and after making a binary image/mask positive cell count or positive stained area (pixels) were counted.

2.9 Quantitative Reverse Transcription Polymerase Chain Reaction

Real-time polymerase chain reaction (RT-PCR) is a method that involves the simultaneous amplification and detection of genetic material during the PCR process. During the PCR process fluorescent dyes incorporate into the amplified product, allowing the measurement of fluorescence intensity and its correlation with the concentration of the PCR product. PCR reactions are distinguished by the specific PCR cycle at which the initial detection of target amplification occurs. This crucial parameter is commonly known as the cycle threshold (Ct), representing the point in time when the fluorescence intensity surpasses the background fluorescence level. As a result, a higher amount of target cDNA in the initial sample correlates with a pronounced increase in fluorescent signal with a subsequent lower Ct value [135, 136]. After incubation, OTC's were shock frozen in liquid nitrogen and tissue pulverization was achieved with mortar and pestle on dry ice with liquid nitrogen. Total RNA was isolated using RNeasy Plus mini kit (Qiagen, Hilden, Germany) according to the manufacturer's instructions. RNA purity and integrity was analyzed by RNA gel as well as with a Bioanalyzer System (Agilent Technologies, Inc., California, USA), which resulted in RIN scores ≥ 8.50. Subsequently cDNA was prepared using LunaScript® RT SuperMix Kit (NEB, Massachusetts, USA) following the instructions. Quantitative gene expression for target and housekeeping genes (see Table 8) was done with SsoAdvanced Universal SYBR Green Supermix (Bio-Rad Laboratories, Inc., Hercules, USA) run on a Biorad CFX384 Real-Time PCR System (Biorad) and quantification cycle values (Ct) were exported for statistical analysis. Data normalization

and post-processing was achieved by GeneX software (version 7.0, MultiD Analyses AB, Göteborg, Sweden). The suitability of six housekeeping genes, namely actin beta (β-Actin), TATA-Box Binding Protein (TBP), Beta-2-Microglobulin (B2M), 18S ribosomal RNA (18sRNA), Glyceraldehyde 3-phosphate dehydrogenase (Gapdh) and Hypoxanthine-guanine phosphoribosyltransferase (Hprt1), was evaluated by examining the stability in gene expression levels throughout the cultivation as well as in control and GPI conditions with the GeneX software (version 7.0). Three of those housekeeping genes, namely 18sRNA, Gapdh and Hprt1, were deemed suitable for data normalization. ΔΔCT values were exported and the $2^{-\Delta\Delta CT}$ method was used for gene expression quantification and statistical analysis. Statistic was calculated with IBM SPSS Statistic 26 (version 6) and graphs were generated with GraphPad InStat software (GraphPad Prism 9.3.1 (471)). Targets included: collagen type I alpha 1 chain (Col1a1), Col2a1, Col10a1, Ihh, matrix metallopeptidase 13 (Mmp13), Oc, Ogp, Rank, RankL, Runx2, Sox9, Osx, Opn, Alpl, Trap, Vegfa, Bmp2 and PthrP.
For each time point at least 6 animals were utilized for qPCR.

For each time point, at least 4 animals were utilized and 3 technical replicates were performed.

Table 8. List of primer sequences used for gene expression analysis by qRT-PCR.

		Primer Sequence	
	Genes	**Forward**	**Reverse**
House keeping genes	*18sRNA*	ACTGCCATTAAGGGTGTGGG	GATGGTGATCACACGCTCCA
	Gapdh	CCTGCACCACCAACTGCTTAGC	GCCAGTGAGCTTCCCGTTCAGC
	Hprt1	GCGAAAGTGGAAAAGCCAAGT	GCCACATCAACAGGACTCTTGTAG
Chondrogenic related genes	*Sox9*	GAGCACTCCGGGCAATCTC	GCCCCTCTCGTTTCAGATCAA
	Col1a1	GTACATCAGCCCAAACCCCA	TCGCTTCCATACTCGAACTGG
	Col2a1	GGCCAGGATGCCCGAAAATTA	GTCACCTCTGGGTCCTTGTTC
	Ihh	TCAGACCGCGACCGAAATAA	CGAGTGCTCAGACTTGACAGA
	PthrP	ACAAGGGCAAGTCCATCCAA	TTGGGAGCAGGTTTGGAGTT
	Col10a1	CCTCTGAGCACCAGAATCCA	CGTCAAGGACACTAGCAGCA
	Mmp13	CTTCTGGCACACGCTTTTCC	TTGTAGCCTTTGGAGCTGCTT

Osteogenic related genes	*Runx2*	GCGCATTCCTCATCCCAGTA	GGTGGGGAGGATTGTGTCTG
	Sp7 (Osx)	ATCCATGCAGGCATCTCACC	ACCTAACCAATTGCCCCCAG
	Spp1 (Opn)	CCAGCCAAGGACCAACTACA	AGTGTTTGCTGTAATGCGCC
	Bglap (Oc)	CTCAACAATGGACTTGGAGCC	GTCCGCTAGCTCGTCACAAT
	Alpl	CGGTTGGTAGCCTCCTTCTG	GACGTTCCGATCCTGAGTGG
Osteoclastogenic related genes	*Tnfrsf11b (Opg)*	CTCACTTGGCCTCCTGCTAA	TTTGGTCCCAGGCAAACTGT
	Tnfrsf11a (Rank)	GGGAAAACGCTGACAGCTAAT	CACACACTTCTTGCTGGCTG
	Tnfsf11 (RankL)	CGACTCTGGAGAGCGAAGAC	TTGTAATTCCCTTTGCACGGC
	Acp5 (Trap)	CAATGACAAGAGGTTCCAGGAGA	GGCAATTTGTGCCGAGACAT
Other	*Vegfa*	CTGCTCTCTTGGGTGCACTGG	CACCGCCTTGGCTTGTCACAT
	Bmp2	AAGCCAAACACAAACAGCGG	GCCACGATCCAGTCATTCCA

2.10 Statistical Analysis

To conduct statistical analyses, IBM SPSS Statistic 26 (version 6) and GraphPad InStat software (GraphPad Prism 9.3.1 (471)) were utilized. Data were subjected to the Kolmogorov-Smirnov test to determine normality. As the data distribution in all samples significantly deviated from normal distribution, non-parametric tests were used to test the statistical significance of the observed differences. For single comparisons, the Mann-Whitney U test was used, whereas for multiple comparisons, the Kruskal-Wallis H test followed by pairwise analysis with Bonferroni correction was used. For all statistical analyses, a difference was considered statistically significant at $p \leq 0.05$.

2.11 Physical parameters of particle irradiation

All experiments related to particle irradiation (Part 2) and research were carried out at MedAustron, the Austrian center for ion therapy and research [137]. The experimental setup in the research room included a horizontal beam line with advanced features such as an active spot scanning technique and active energy variation for both proton and C-ions. To ensure precise and standardized positioning of samples within measurement phantoms, a high precision robot couch and a laser positioning system were utilized. For the proton ion irradiation experiments, a treatment plan was developed using a SOBP of 4 cm and a field size of 17 x 9 cm². The RayStation v7.99 treatment planning system (TPS; RaySearch Laboratories, Stockholm, Sweden), was employed for treatment planning. The dose calculation was performed using a Monte Carlo v4.3 dose engine [138]. The maximum proton energy used in these experiments was 124.7 MeV, resulting in a range of 101.2 mm at the 80% dose level in water. Similarly, for the C-ion IR experiments, a treatment plan with a 4 cm SOBP was created, using the same field sizes, TPS, and dose engine. The maximum C-ion energy used was 238.6 MeV/u, resulting in a range of 101.1 mm at the 80% dose level in water. To ensure a flat SOBP, ripple filters were employed in both cases. The energy layers for both proton and C-ion experiments were spaced either 1 mm or 2 mm apart. Pencil beam scanning was used as the radiation delivery technique, and no range shifters were employed to modify the beam. The LET values for both proton and C-ion IR were determined directly from the treatment planning system using Monte Carlo calculations.

The experimental procedure involved irradiating bone slices from the left leg with either 8 Gy of proton or 8 Gy of C-ions. In contrast, the bone slices from the corresponding right leg were not irradiated and served as control samples. The selection of the 8 Gy dosage was made to effectively demonstrate its impact on postnatal endochondral ossification within the proximal femur epiphysis.

2.12 Workflow and experimental setup

This dissertation combines the results of two individual studies based on the ex vivo rat femur culture [118] which was modified to investigate the regeneration processes and endochondral ossification after **1)** GPI [1] and **2)** particle irradiation (proton or C-ions) [2] (Fig. 9).

To examine physiological and pathological processes following GPI (Part one) we introduced an injury similar to Salter-Harris classification type III and IV followed by cultivation for up to 15 days in vitro (DIV) (Fig. 8, Part one).

Part two of the dissertation focuses on the postnatal endochondral ossification after the ex vivo cultures underwent either 8 Gy proton or C-ion IR at the MedAustron facilities before in vitro cultivation for up to 14 days (Fig. 8, Part two).

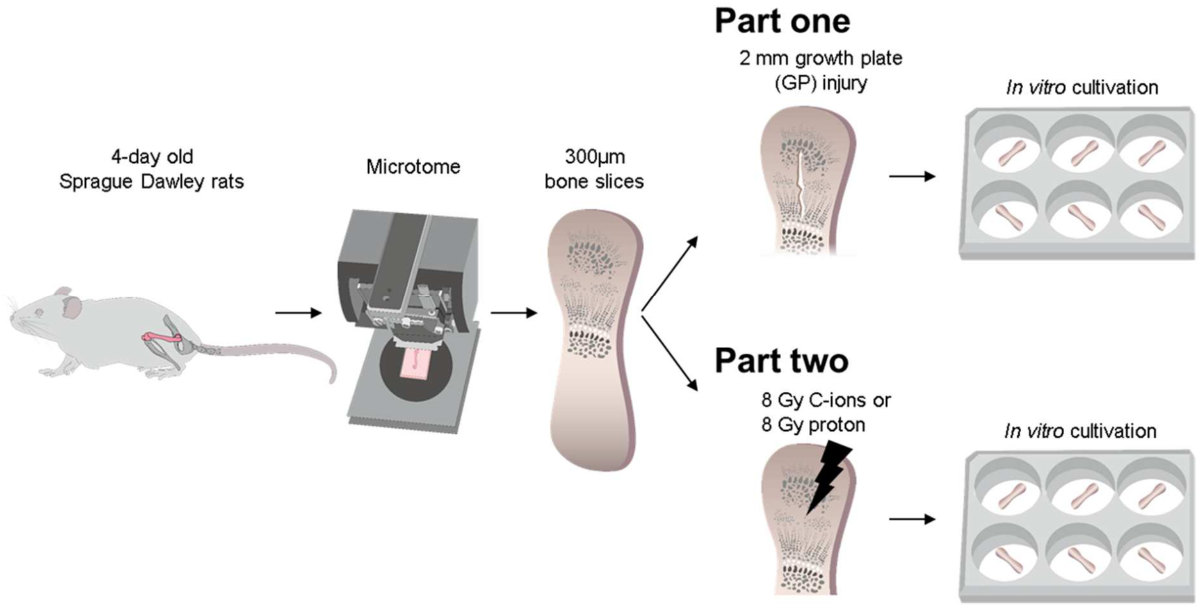

Figure 9. Schematic overview of the dissertation projects. Femurs were harvested and processed into 300 µm ex vivo bone cultures. In part one, a 2 mm long growth plate injury (GPI) was induced within the bone slices (OTC) to investigate regeneration processes during in vitro cultivation. In part two, the OTCs were subjected to 8 Gy proton or carbon ions (C-ions) irradiation at MedAustron facilities, followed by in vitro cultivation (DIV). Reproduced and modified from [1, 2] under the terms of CC BY.

Part One

3 Results Part One

3.1 Organotypic bone culture viability

In order to validate the established OTC's protocol and to evaluate the impact of GPI on tissue viability and survival in an in vitro setting, we conducted live/dead staining on unfixed OTC's at the time points: 0, 1, 3, 7, and 15 DIV (Fig. 10a). Our data confirms the survival of the OTC's during the 15-day cultivation time. Further, our observations revealed the presence of dead cells and/or tissue initially within the injury site at 0 DIV, which gradually disappeared by 7 DIV. Following 7 DIV, we observed elongated, viable cells surrounding and lining the edges of the injury site. These cells increased in number and eventually covered the entire injury site by 15 DIV.

Moreover, the quantification of dead cells within the GPI area demonstrated a consistent and significant increase in the number of dead cells throughout the cultivation period for both injured samples (0-7 DIV: $p = 0.044$; 0-15 DIV: $p = 0.003$) and non-injured control bone slices (0-7 DIV: $p = 0.01$; 0-15 DIV: $p = 0.01$) (Fig. 10c-d). However, no statistically significant differences were observed when comparing the injured and control OTCs at the respective time points (Fig. 10b). Representative control images can be found in Fig. 46b.

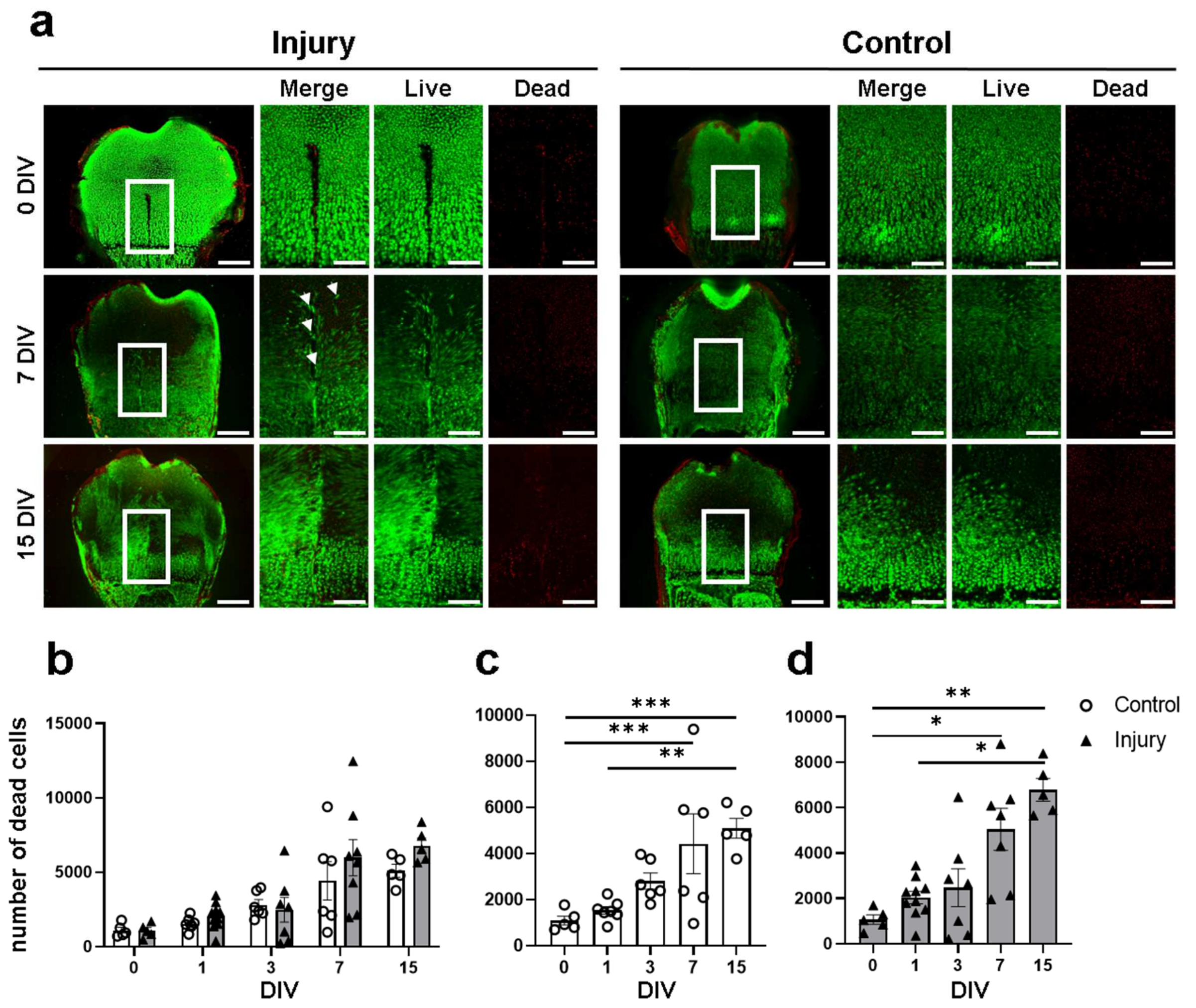

Figure 10. Tissue survival and regeneration was assessed by live/dead staining. a) Representative images of unfixed proximal femur ex vivo cultures (OTCs) with and without growth plate injury (GPI) at 0-, 7-, and 15-days of in vitro cultivation (DIV). White rectangles indicate the regions depicted at higher magnification alongside. Elongated cells surrounding and lining the injury area are marked by white arrows. Live cells are shown in green, while dead cells are in red. Scale bars: 500 µm (proximal femur) and 250 µm (magnified area). **b-d)** Quantification of dead cells was conducted, and the statistical significance of observed differences was assessed using the Kruskal-Wallis Test for temporal changes and the Mann-Whitney-U Test for injury vs. control comparisons. Data are presented as mean ± SEM with a minimum sample size of n ≥ 3 animals per time point and 3 technical replicates. Significance levels are denoted as *$p \leq 0.05$, **$p \leq 0.01$ and ***$p \leq 0.001$; circles (controls, white) and triangles (injury, grey). **d)** An outlier (injury 7 DIV) was excluded in the graph for better visual examination. Reproduced from [1] under the terms of CC BY.

3.2 Regeneration of growth plate injury (GPI) within the ex vivo organotypic culture (OTC)

Our injured OTC’s exhibited regeneration processes during the 15-day in vitro cultivation as indicated by the performed live/dead staining (Fig. 11a). To confirm the occurrence of the regenerative process, we examined the injury site using histological and IHC staining’s at the specific time points. H&E and Movat-Pentachrome staining revealed injured tissue at 0 DIV and the initiation of regeneration at 1 DIV (Fig. 11a,b). Over the course of the 15-day period, the number of cells within the injury cleft increased, and fibers and tissue originating from dissolving chondrocytes were observed adjacent to the injury. The nuclei in the cells closest to the injury were oriented towards the injury cleft. At 7 DIV, cell aggregates (Fig. 11a-c, 7 DIV, black dashed oval) were observed in the hypertrophic zone, and at 15 DIV, they were observed in the upper part of the injury, suggesting the possible migration of bone marrow cells along the injury cleft.

Col2a1 IHC staining exhibited positive staining within the injury site at 0 DIV, but not in the rest of the epiphysis (Fig. 11c). By 1 DIV, the edge of the injury cleft showed intense Col2a1 staining, indicating the initiation of regeneration processes due to increased Col2a1 production by surrounding chondrocytes. Fibers within the injury cleft also exhibited positive staining for Col2a1 at 3 DIV, as well as in the rest of the epiphysis. The cell aggregates observed in H&E and Movat-Pentachrome staining at 7 DIV were embedded in an intensely stained Col2a1 matrix. By 15 DIV, the majority of the injury site was filled with a Col2a1-positive matrix embedded with small cells.

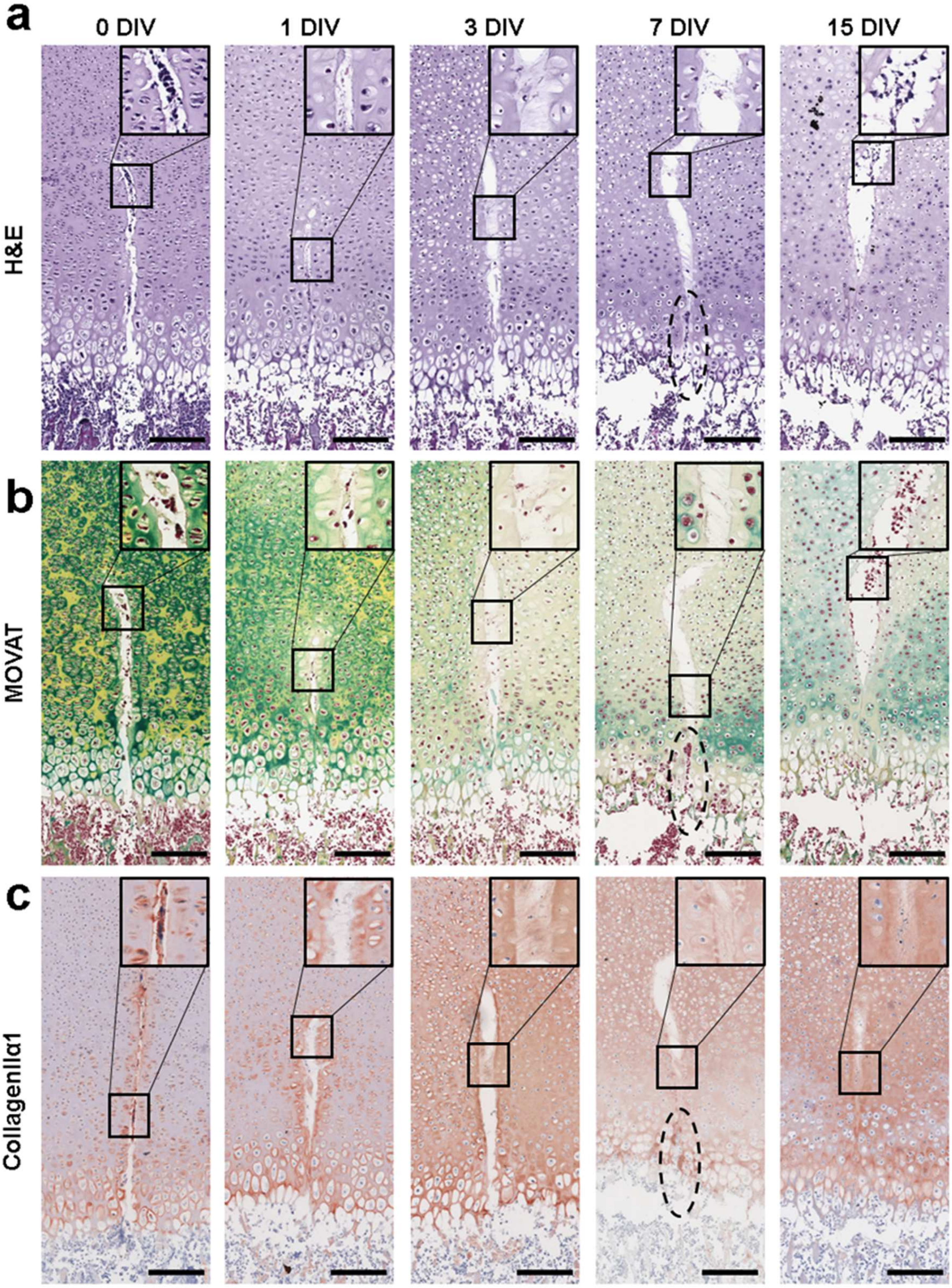

Figure 11. Regeneration of growth plate injury (GPI) in an ex vivo bone slices model (OTC) under in vitro culture. a-c) The regenerative process was assessed using Hematoxylin

and Eosin (H&E) staining, Movat-Pentachrome histological staining, and immunohistochemistry (IHC) staining for type II collagen (Col2a1). Representative images of the injured area of OTC's at 0, 1, 3, 7, and 15 days of in vitro cultivation (DIV) are presented, along with a magnified view of newly formed structures within the injury site (indicated by black squares, magnification 40 µm). Cell aggregation (black dashed ovals) was observed in all staining techniques at 7 DIV. Scale bar: 150 µm. Part of this figure adapted from [1] under the terms of CC BY.

We further assessed the injury area, specifically examining the cells invading the lesion by performing IHC to evaluate their proliferation potential and differentiation status. In this analysis, we found proliferating cells within the injury lesion at 0, 1, and 7 DIV, as evidenced by positive Ki67 staining (Fig. 12a). Conversely, apoptosis was only observed at 15 DIV, as indicated by slight positive c-Cas3 staining (Fig. 12b). Furthermore, we detected the presence of stem cells within the injury lesion at 0, 7, and 15 DIV, marked by positive Vimentin staining (Fig. 12c). Additionally, positive staining for the chondrogenesis regulator Bmp-2 was noted at 0, 1, and 3 DIV in cells within the injury lesion (Fig. 12d). This data suggests that there is a migration of stem cells into the injury area, where they proliferate and differentiate toward the chondrogenic lineage. Representative control images can be found in Fig. 46a.

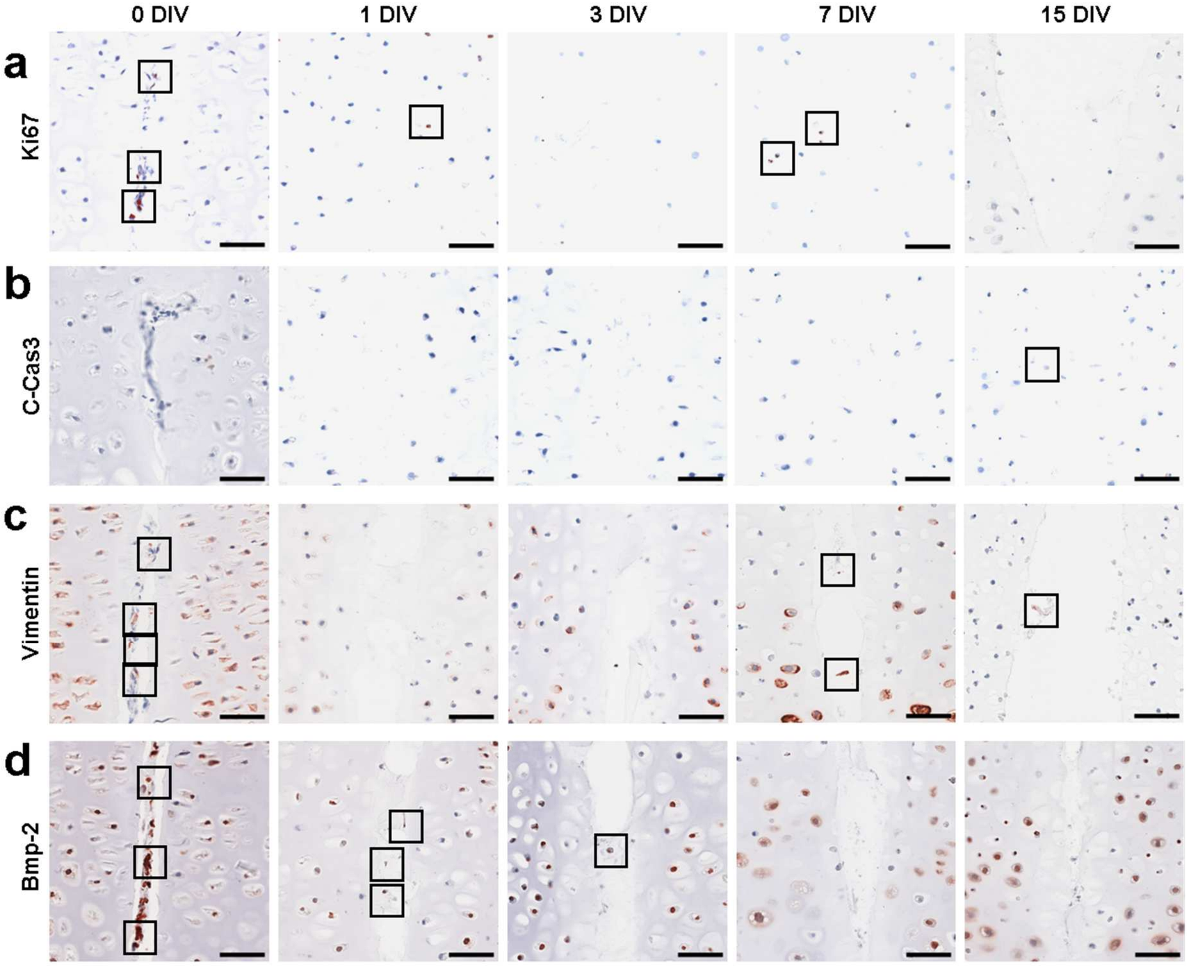

Figure 12. Cells within the growth plate injury (GPI) exhibit proliferation and stem cell abilities. a-d) The regenerative process was assessed using immunohistochemistry (IHC) staining for Ki67 (proliferation marker), cleaved Caspase 3 (c-Cas3, apoptosis marker), Vimentin (stem cell marker) and bone morphogenetic protein 2 (BMP-2, chondrogenesis regulation marker). Representative images of the injured area of OTC's at 0, 1, 3, 7, and 15 days of in vitro cultivation (DIV) are presented. Positive staining (red) is indicated by the black square. Scale bar: 150 µm.

Next, we visualized the injury cleft and focused on immigrated cells by scanning transmission electron microscopy (STEM) with field emission mode in combination with ATLAS TM at 0 and 7 DIV (Fig. 13). This method allowed for imaging of a larger area of the injury cleft which was later recorded by the transmission electron microscope. At 0 DIV, cell fragments (purple stars), erythrocytes (yellow arrows) and chondrocytes (red arrows) were detected within the injury site (Fig. 13a,b). However, at 7 DIV, we observed cell clusters containing stem cells (black arrow heads), fibroblasts (black arrows), and chondrocytes (white arrow heads) producing collagen fibers (black star) within the injury site (Fig. 13c,d). The clusters were particularly located at the area of trabecular spicules upwards the DZ within the injury cleft, suggesting that the regeneration of GPI progresses from the trabecular spicules upwards. The observed cells were identified based on their characteristic ultrastructural morphology and were validated by comparison to stem cell pellets (Fig. 13e) or chondrocytes (Fig. 13f) and fibroblast (Fig. 13g) from a non-injured bone slice. This data together with the live/dead and IHC data suggests that there is a migration of stem cells into the injury area, where they proliferate and differentiate toward the chondrogenic lineage.

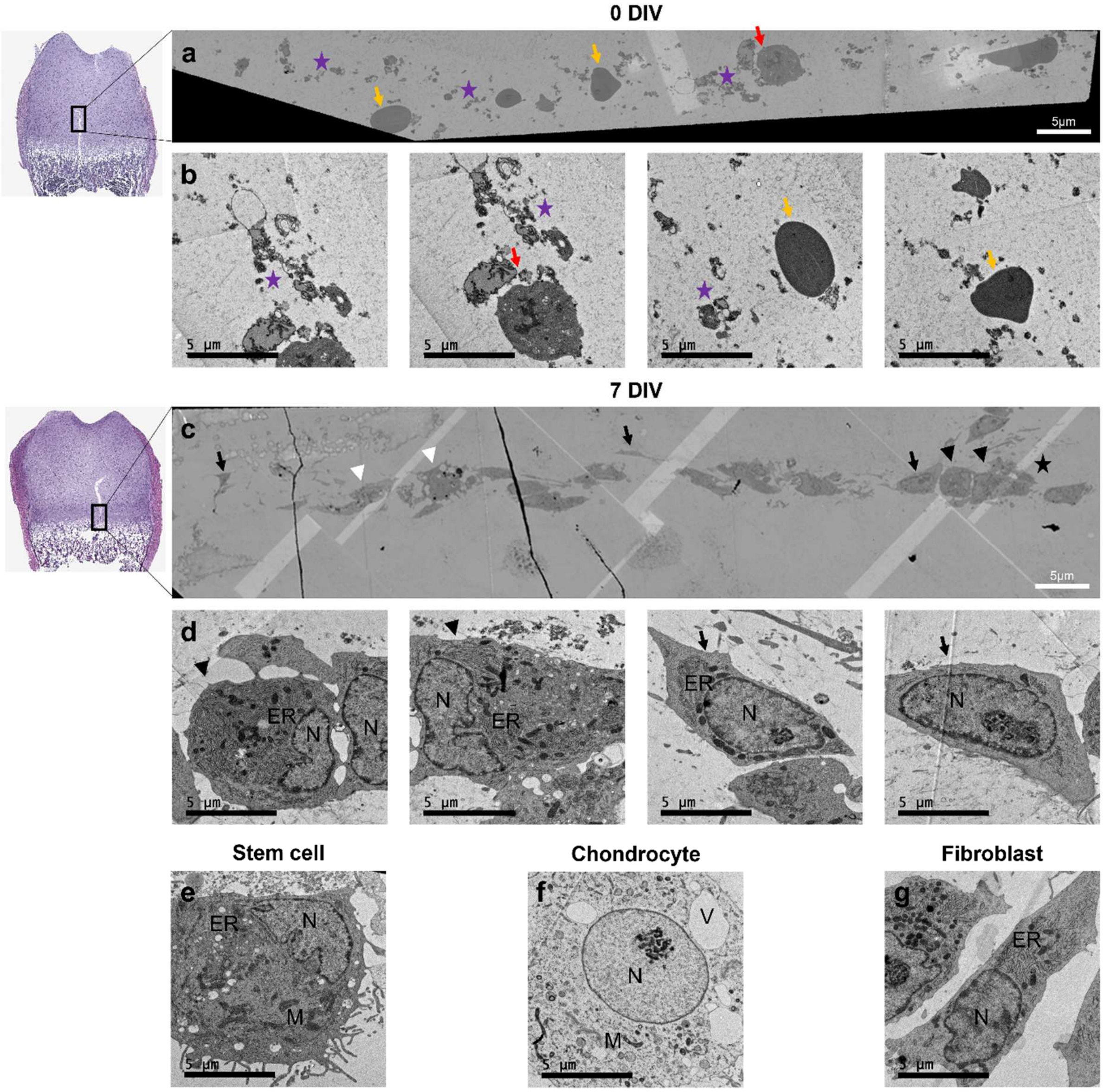

Figure 13. Stem cell infiltration and fiber production by chondrocytes and fibroblasts. Representative scanning transmission electron microscopy (STEM) images at **a)** 0 and **c)** 7

days of in vitro cultivation (DIV) providing an overview of the injury area. ATLAS transmission microscopy (TM) of cells located within the injury cleft at **b)** 0 DIV, indicating the presence of cell fragments (purple stars), erythrocytes (yellow arrow) and chondrocytes (red arrow) and **d)** at 7 DIV, indicating stem cells (black arrowheads), chondrocytes (white arrowhead), fibroblasts (black arrow) and collagen fibers (black star). Scale bar: 5 µm. Reproduced with modifications from [1] under the terms of CC BY.

3.3 Influence of growth plate injury (GPI) on the endochondral ossification in non-injured adjacent areas

To investigate the underlying effect of GPI on postnatal endochondral ossification in the ex vivo bone model, the injured OTC's and their corresponding controls were morphologically analyzed at 0, 1, 3, 7, and 15 DIV using H&E, Movat-Pentachrome, Safranin O-Fast Green (Fig. 14a-c). Differences between GPI and control OTCs were observed from 7 DIV onwards, hence the distinct zones, transition zone (TZ, yellow square), middle zone (MZ, red square), and deep zone (DZ, blue square) at these time points are described in more detail in the following.

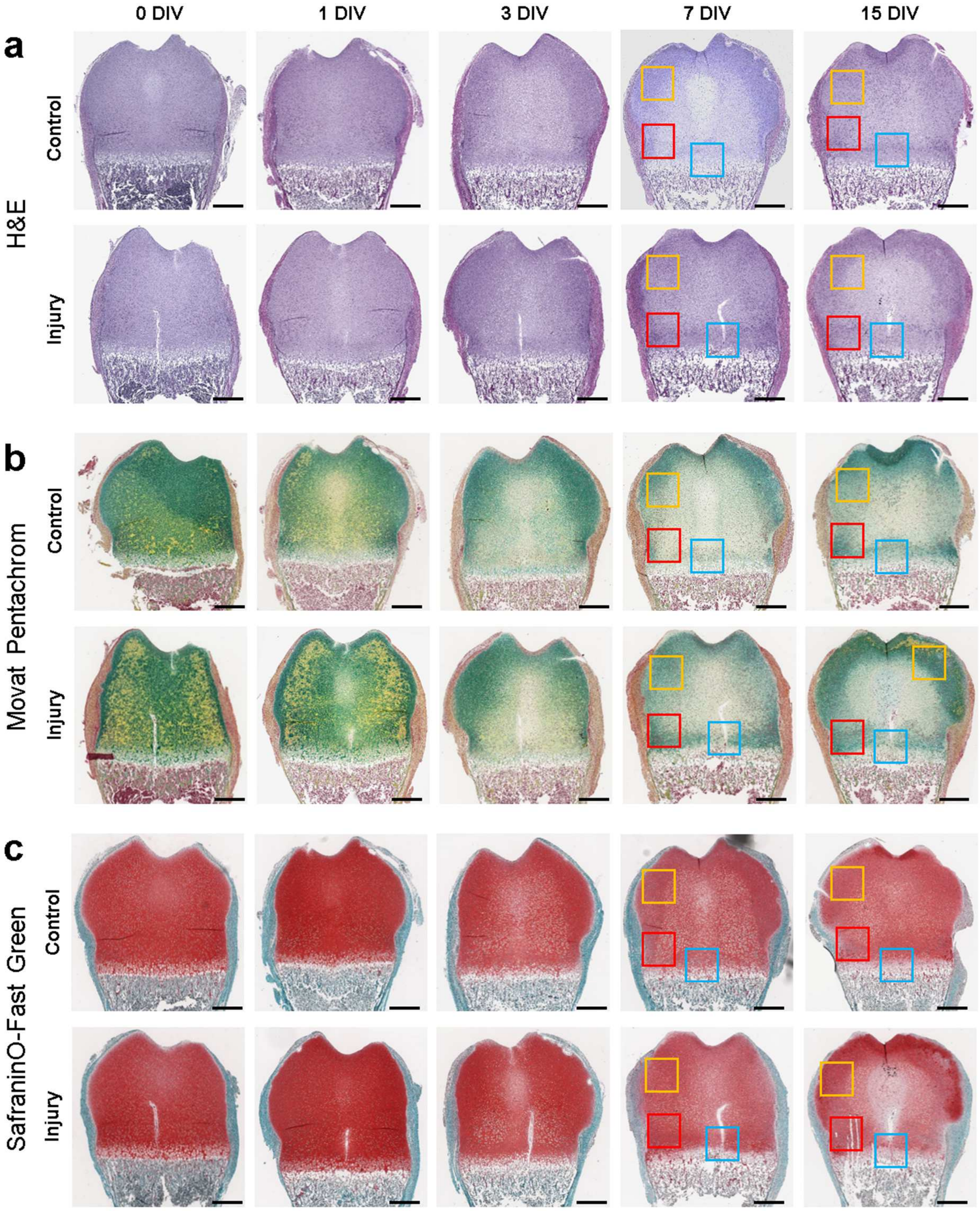

Figure 14. Representative images of ex vivo bone cultures (OTC) with without growth plate injury (GPI) which underwent histological staining using various techniques. Images of injured and control proximal femur OTC at 0, 1, 3, 7, and 15 days of in vitro cultivation (DIV) stained with **a)** Hematoxylin and Eosin stain (H&E), **b)** Movat-Pentachrome, and **c)** Sarfanin O-Fast Green stain. The colored squares indicate transition zone (TZ, yellow square),

middle zone (MZ, red square), and deep zone (DZ, blue square) for following detailed investigation. Scale bar: 500 µm. Reproduced from [1] under the terms of CC BY.

Morphological evaluation of the regeneration process and endochondral ossification was performed by H&E staining (Fig. 15). At 7 DIV, control OTC presented a well-structured organization of the epiphysis and GP. The TZ contained a large number of chondrocytes (black arrows), whereas pre-hypertrophic chondrocytes were adjacent to the potential secondary ossification center (red arrows). The MZ contained proliferating (blue arrows) and isogenic groups of (pre-)hypertrophic chondrocytes (orange arrows). The DZ exhibited an intact hypertrophic zone (black bracket). Contrary, injured OTC at 7 DIV revealed impaired structural organization and chondrocyte transition. The TZ displayed randomly distributed metabolic active chondrocytes (yellow arrows) and pre-hypertrophic chondrocytes (red arrows). In the MZ high number of proliferating chondrocytes were observed (black dashed circle). In the DZ, the hypertrophic and calcification area was markedly decreased to only a few layers of hypertrophic chondrocytes (black bracket). The density of cells further was reduced, compared to the control. Notably, cell aggregates were observed within the injury cleft in the DZ (red dashed oval).

At 15 DIV, the control OTC contained randomly distributed active (yellow arrows) and pre-hypertrophic chondrocytes (red arrows) within the TZ, as seen at 7 DIV in the TZ of injured OTC. MZ exhibited metabolic active (yellow arrows), isogenic groups of pre-hypertrophic (orange arrows) and proliferating chondrocytes (black dashed circle). In the DZ, the previous observed intact hypertrophic zone decreased (black bracket), cell density was reduced, and no columnar formation were observed. Injured OTC at 15 DIV displayed a more organized manner of chondrocyte transition in the TZ, where chondrocytes (black arrow) transitioned into pre-hypertrophic chondrocytes (red arrows) adjacent to the potential secondary ossification center. However, in the MZ, a cluster of multicellular columns (black dashed oval) towards the hypertrophic zone was observed. The TZ was similar to the control OTC. Furthermore, some injury OTC showed the closure of the injury cleft at the hypertrophic area (red dashed oval).

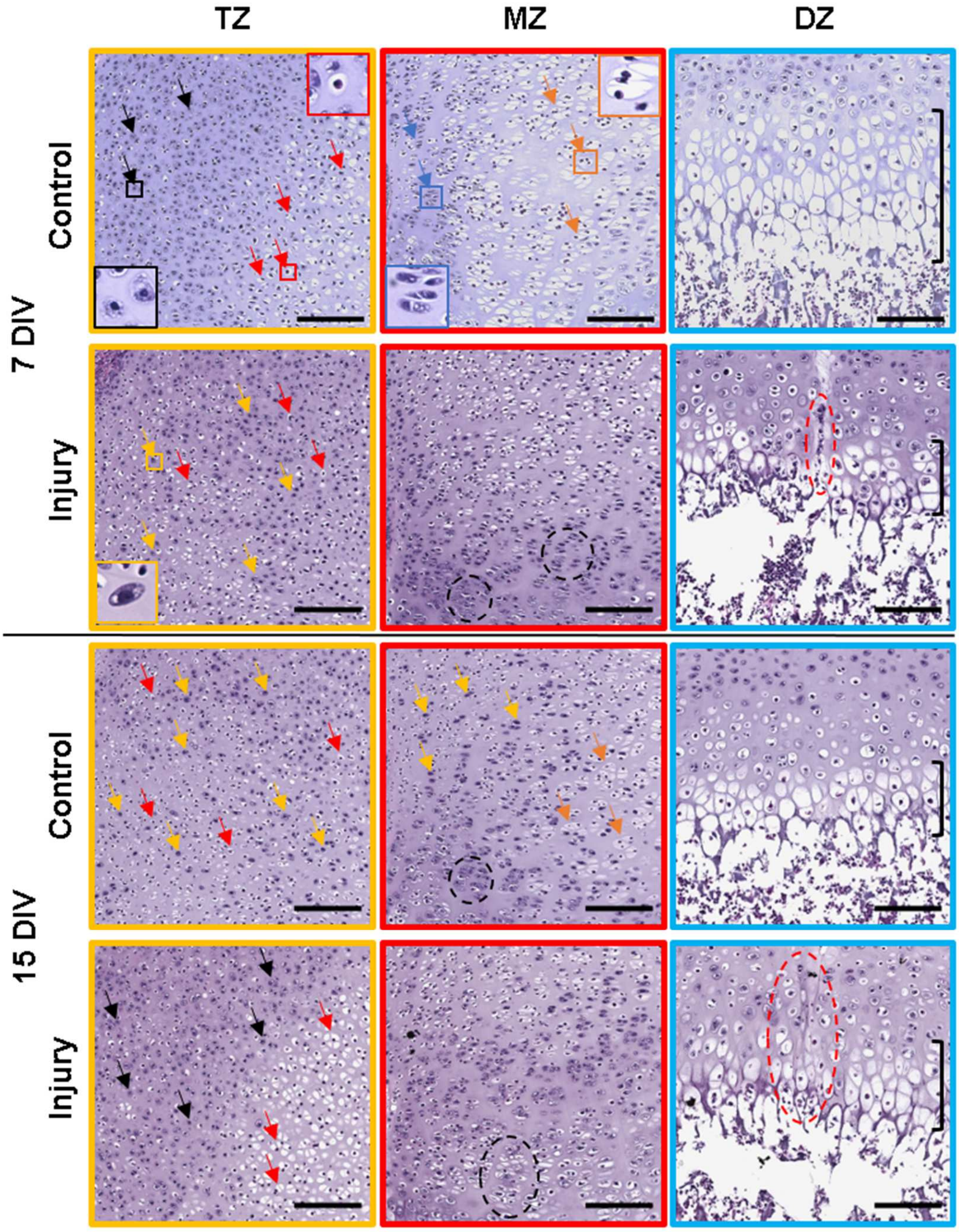

Figure 15. Structural and organization was influenced by the growth plate injury (GPI). Representative images of ex vivo bone cultures (OTC) with GPI and respective controls cultured for 7 and 15 days of in vitro cultivation (DIV) stained with Hematoxylin and Eosin (H&E). The colored squares indicate transition zone (TZ, yellow square), middle zone (MZ, red square) and deep zone (DZ, blue square). Chondrocytes at different maturation state are indicated by black arrow - chondrocytes (highlighted in a black box with higher magnification), red arrow - pre-hypertrophic chondrocytes (highlighted in a red box with higher magnification),

blue arrow - proliferating chondrocytes (highlighted in a blue box with higher magnification), orange arrow - isogenic group of (pre-)hypertrophic chondrocytes (highlighted in an orange box with higher magnification), yellow arrow - metabolic active chondrocytes (highlighted in a yellow box with higher magnification), black bracket - hypertrophic zone. Additionally, black dashed circle - stacks of proliferating chondrocytes and the black oval - clusters of multicellular columns. The scale bar: TZ/MZ/DZ: 150 µm and higher magnification: 40 µm. Reproduced from [1] under the terms of CC BY.

We conducted Movat-Pentachrome staining to investigate the impact of GPI on cartilage maturation and endochondral ossification (Fig. 16). In control OTC, at 7 DIV, we observed significant cartilage staining in the TZ adjacent to the prospective articular cartilage and in the MZ next to the zone of Ranvier (black stars). The inter-territorial matrix along the DZ had marginal cartilage staining. However, in injured OTC, we detected significant cartilage staining throughout the entire TZ and adjacent to the hypertrophic area in the MZ and DZ (black stars). By 15 DIV, clear differences between injured and control OTCs were observed in the distal femurs. In control OTC, cartilage was limited to the emerging articular cartilage area (see Fig. 14b, 15 DIV) and the area adjacent to the zone of Ranvier (MZ, black stars). In contrast, in injured OTC, a wide "ring" of intensely stained cartilage was present around the epiphysis (see Fig. 14b, 15 DIV), indicating an intensified secretion/assembly of cartilage proteins in this area (TZ, black stars). Here, also beginnings of ECM mineralization were observed (TZ, black arrows), which were not visible in control OTC.

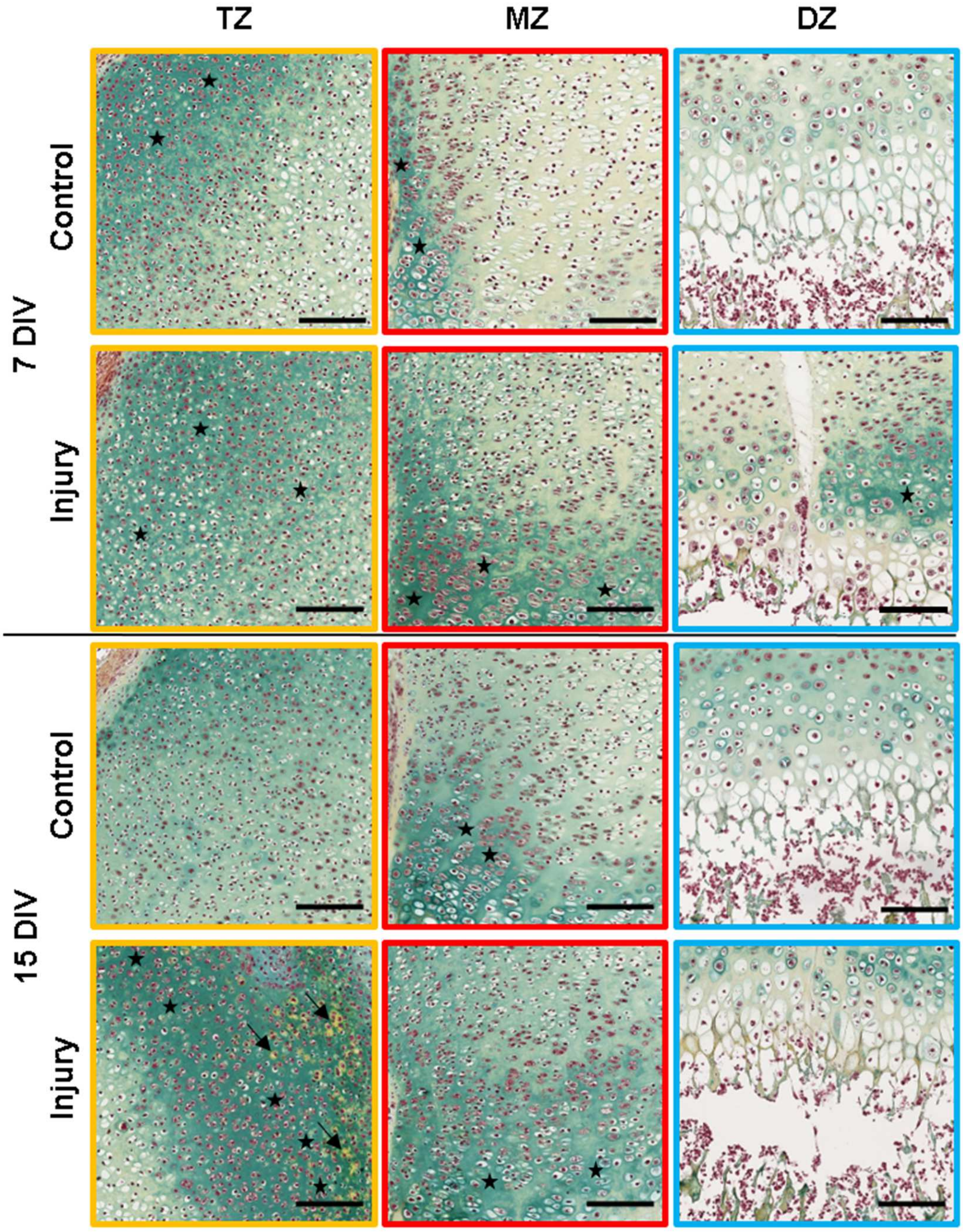

Figure 16. Injury-associated changes in extracellular matrix (ECM) generation. Representative images of ex vivo bone cultures (OTC) with growth plate injury (GPI) and respective controls cultured for 7 and 15 days of in vitro cultivation (DIV) stained with Movat-Pentachrome staining. The colored squares indicate transition zone (TZ, yellow square), middle zone (MZ, red square) and deep zone (DZ, blue square). This staining results in structures being stained as follows: cell nuclei (black), cytoplasm (reddish), elastic fibers (red), collagen connective tissue (light yellow), mineralized tissue/bone (dark yellow, black arrows)

and mineralized cartilage (dark green-blue, black stars). Scale bar: 150 µm. Reproduced from [1] under the terms of CC BY.

To investigate the impact of GPI on the secretion of ECM proteins, we conducted Safranin O-Fast green staining, which indicates the presence of PG in the tissue (Fig. 17). At 7 DIV, no significant differences were observed between control and injured OTCs. At 15 DIV, intensive PG staining was limited to the emerging articular cartilage in OTC and the periphery of the epiphysis in injured OTC (see Fig. 14c, 15 DIV, dark red staining). Interestingly, a strongly increased number of chondrocytes exhibited intensively stained cell membranes within the TZ and MZ due to GPI compared to the control (black arrows). The observed time-dependent differences in proteoglycan staining patterns between control and injured slices correspond to the Movat-Pentachrome staining patterns (see Fig. 14 and Fig. 16).

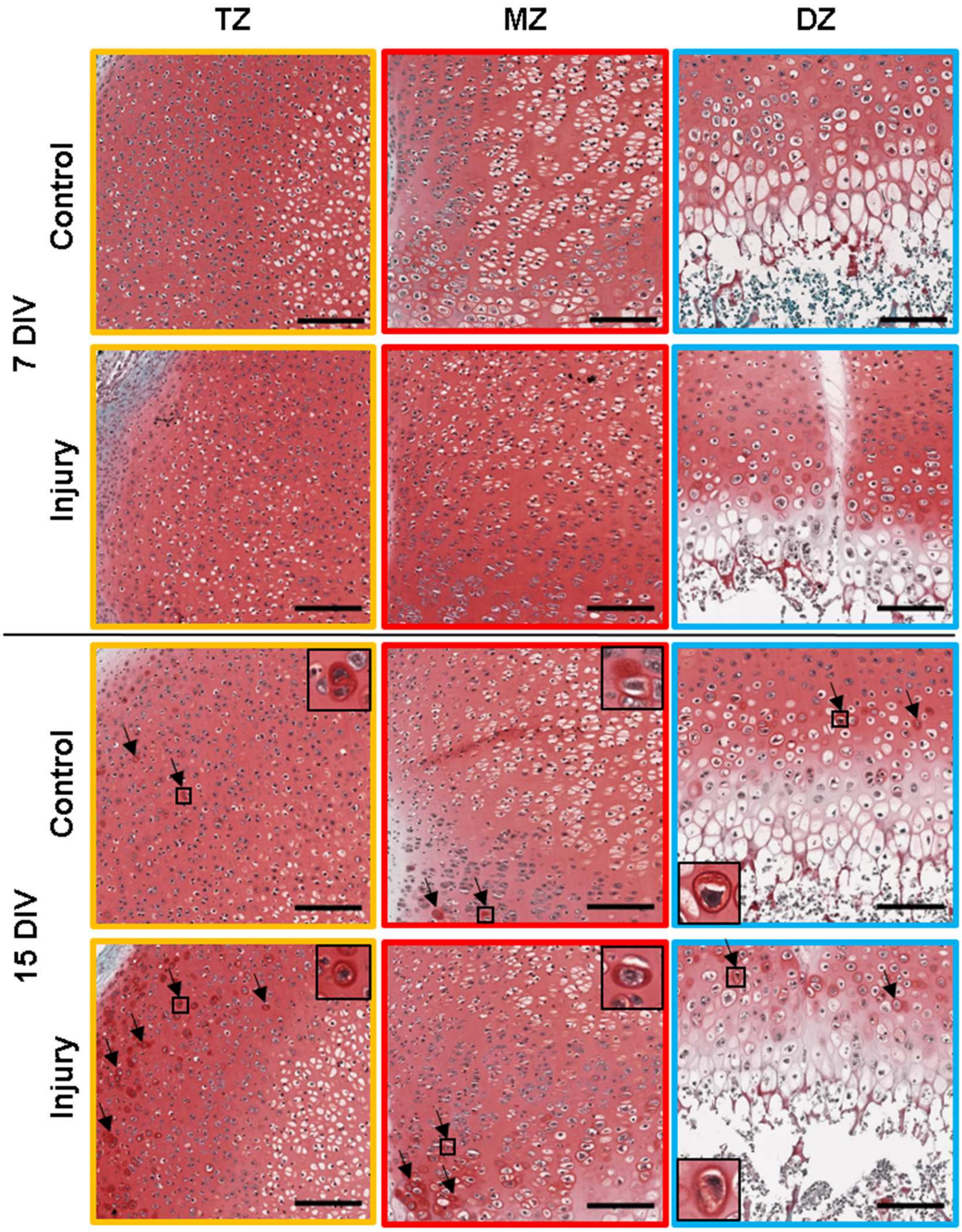

Figure 17. Increased proteoglycan (PG) production and secretion due to growth plate injury (GPI). Representative images of ex vivo bone cultures (OTC) with GPI and respective controls cultured for 7 and 15 days of in vitro cultivation (DIV) stained with Safranin-O/Fast Green staining. The colored squares indicate transition zone (TZ, yellow square), middle zone (MZ, red square) and deep zone (DZ, blue square). Black arrows indicate PG rich cell membrane of chondrocytes with higher magnification in black box. The scale bar: TZ/MZ/DZ: 150 µm and higher magnification: 40 µm. Reproduced from [1] under the terms of CC BY.

3.4 Bone formation and calcification during the in vitro cultivation (DIV)

Bone formation and calcification of tissue was assessed through the staining of calcium deposits by Alzarin Red S staining (Fig. 18). Calcium deposits were detected in the zone of Ranvier/ring of la croix and increased along the perichondrium towards the articular cartilage over the cultivation time in both conditions. Interestingly, calcium deposits were detected earlier with control OTC compared to injured OTC – 1 vs. 3 DIV (black arrows). At 15 DIV injured OTC exhibited a profoundly stronger staining of calcium deposits in the perichondrium compared to the control OTC.

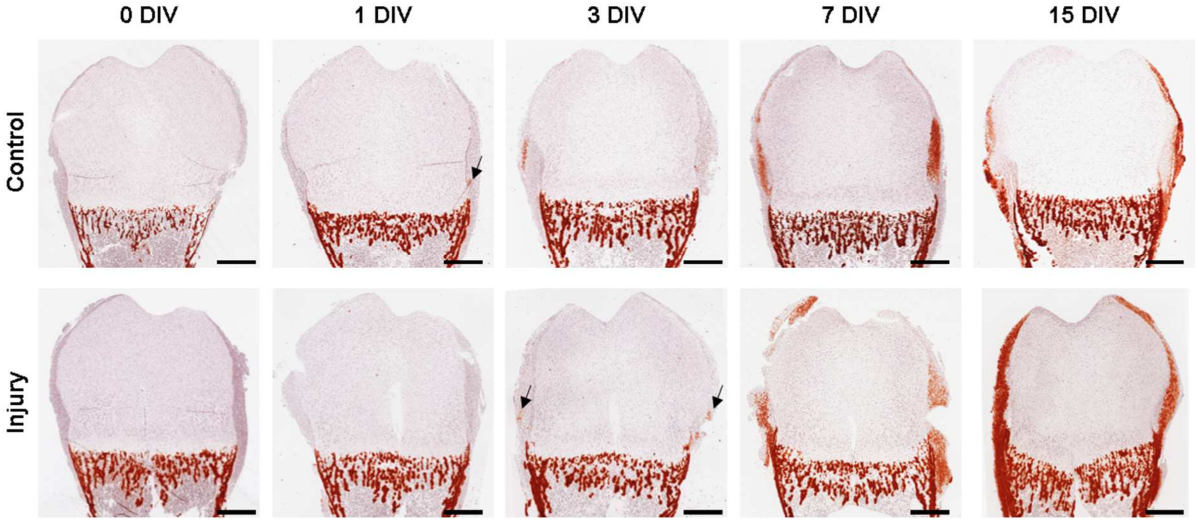

Figure 18. Accelerated perichondral calcification within the ex vivo bone cultures (OTC) due to growth plate injury (GPI). Representative images of Alzarin Red S staining of the proximal femur cultures with and without GPI at 0, 1, 3, 7, and 15 days of in vitro cultivation (DIV). Intense red staining indicates calcification (calcium deposits). Scale bar: 500 µm.

2.4 Influence of growth plate injury (GPI) on proliferation and apoptosis

To investigate the effect of GPI on cell proliferation and apoptosis in the injured and adjacent regions, IHC of Ki67 (proliferation marker) and c-Cas3 (apoptosis marker) was performed. The results showed a profound reduction in proliferation marked by Ki67 positive staining within the bone marrow cells and proximal epiphysis after 1 DIV in both conditions (Fig. 19a,c). In contrast, the number of c-Cas3 positive cells steadily increased in the epiphysis and reached its peak at 3 DIV in both conditions (Fig. 19b). Afterwards, it decreased, almost returning to the original level (Fig. 19d). We did not observe significant differences between the injured and control OTCs at the respective time points for Ki67 as well as c-Cas3 (Fig. 19c,d). Representative control images can be found in Fig. 46a.

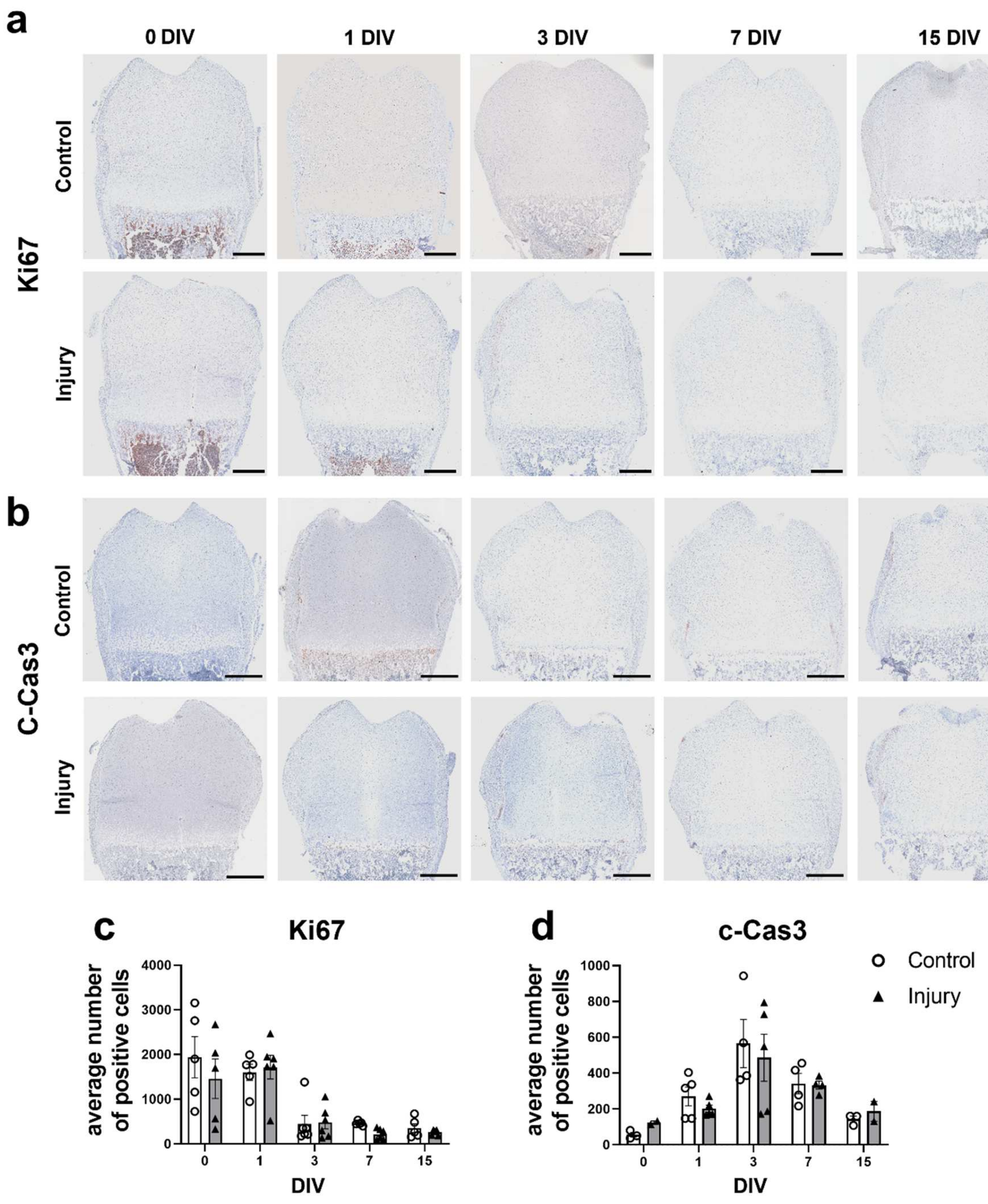

Figure 19. Growth plate injury (GPI) does not affect proliferation or apoptosis within the ex vivo bone culture (OTC). a,b) Representative images of proximal femur OTC with and without GPI stained by immunohistochemistry (IHC) of the proliferation marker Ki67 and the apoptotic marker cleaved Caspase 3 (c-Cas3) at 0, 1, 3, 7, and 15 days of in vitro cultivation (DIV). Scale bar: 500 µm. **c,d)** Quantification of positively stained pixels in IHC. Statistical

significance of observed differences was assessed by Mann-Whitney-U Test for injury vs. control comparisons. Data are presented as mean ± SEM with a minimum sample size of n ≥ 3 animals per time point (exception injury 0 DIV and 15 DIV), 3 technical replicates. Significance levels are denoted as *p ≤ 0.05, **p ≤ 0.01 and ***p ≤ 0.001; circles (controls, white) and triangles (injury, grey).

Moreover, we also analyzed the stem cell potential of cells within the GP in adjacent areas following the injury. Interestingly, we observed Vimentin-positive cells within the TZ at 7 and 15 DIV, but their numbers were profoundly reduced due to sustained GPI (Fig. 20). Representative control images can be found in Fig. 46a.

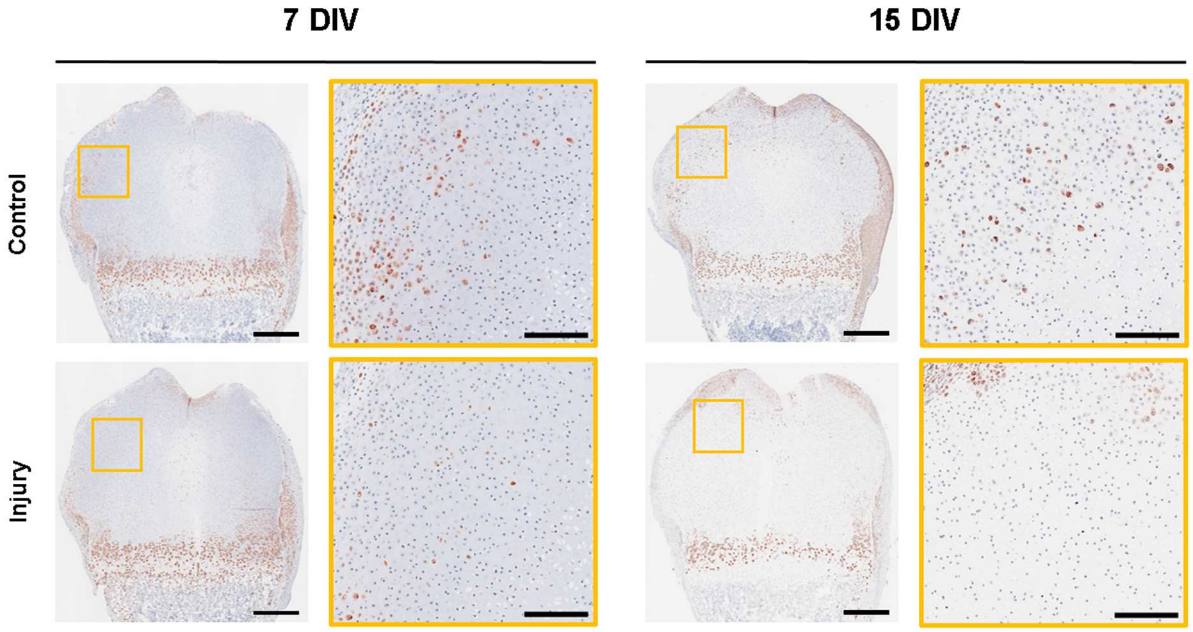

Figure 20. Stem cell potential in the ex vivo organotypic culture (OTC). Immunohistochemisty (IHC) with stem cell marker Vimentin was performed on OTC's at 7 and 15 days of in vitro cultivation (DIV) with and without sustained growth plate injury (GPI). Representative images of proximal epiphysis OTC with higher magnification of the transition zone (TZ, yellow square). Scale bar: proximal epiphysis: 500 µm, TZ: 150 µm.

3.5 Growth plate injury (GPI) influence on extracellular matrix maturation within the proximal epiphysis

To further dissect alterations in ECM and endochondral ossification, we analyzed the expression of Col2a1, Acan, and Col10a1 by IHC (Fig. 21). Representative control images can be found in Fig. 46a.

With regard to Col2a1, an injury-induced disruptions in expression pattern particularly at 0, 1, and 7 DIV could be observed (Fig. 21a). Within the control OTC the area of Col2a1 positive staining increased constantly throughout the whole proximal epiphysis until 7 DIV. By 15 DIV a reduction of Col2a1 positive area in regions closer to the columnar zone was observed. In contrast, at 0 and 1 DIV injured OTC's exhibited an intense Col2a1 staining at the site of injury. At 7 DIV Col2a1 positive staining was extensively attenuated compared to the control. Here, the Col2a1 expression was not established throughout the whole epiphysis and was missing within the columnar zone as well as multiple regions in the transition zone. At 15 DIV both conditions exhibited similar expression patterns. Analysis of positive stained pixel revealed a significantly increase within the injured OTC's from 1 DIV to 7 DIV ($p = 0.012$) and a highly significant increase from 1 DIV to 15 DIV ($p = 0.001$) (Fig. 21d).

Regarding Acan, injured and control OTC alike, exhibited an increased positive staining within the ECM of the epiphysis throughout the cultivation time (Fig. 21b). Starting at 3 DIV chondrocytes within the DZ and at the later time points throughout the epiphysis exhibited a profound Acan positive capsular membrane staining. The area of intense capsular staining was significantly increased within the injured OTC from 1 to 7 DIV ($p = 0.017$) (Fig. 21e). Although the number of intensely stained chondrocytes were similar between the control and injured OTC at the specific time points, the distribution of these cells within the epiphysis varied immensely. Whilst in the control OTC these specific chondrocytes were first located within the TZ and PZ on 7 DIV, they finally formed a circle within the epiphysis on 15 DIV. Contrary, these intense stained chondrocytes are distributed all over the epiphysis within the injured OTC on 7 DIV and form a semicircle on 15 DIV.

A clear time-dependent increase of Col10a1 positive staining within the GP and metaphysis during the cultivation period was detected in the control OTC (Fig. 21c). In contrast, the area as well as the intensity of ColXa1 positive staining was notably lower in injured OTC when compared to the control, starting from 3 DIV, with the weakest intensity at 15 DIV (bracket). While the positive staining increased over the cultivation time within the control OTC, in the injured OTC the staining decreased (bracket). Furthermore, no significant difference was detected by pixel analysis between injured and control OTC (Fig. 21f).

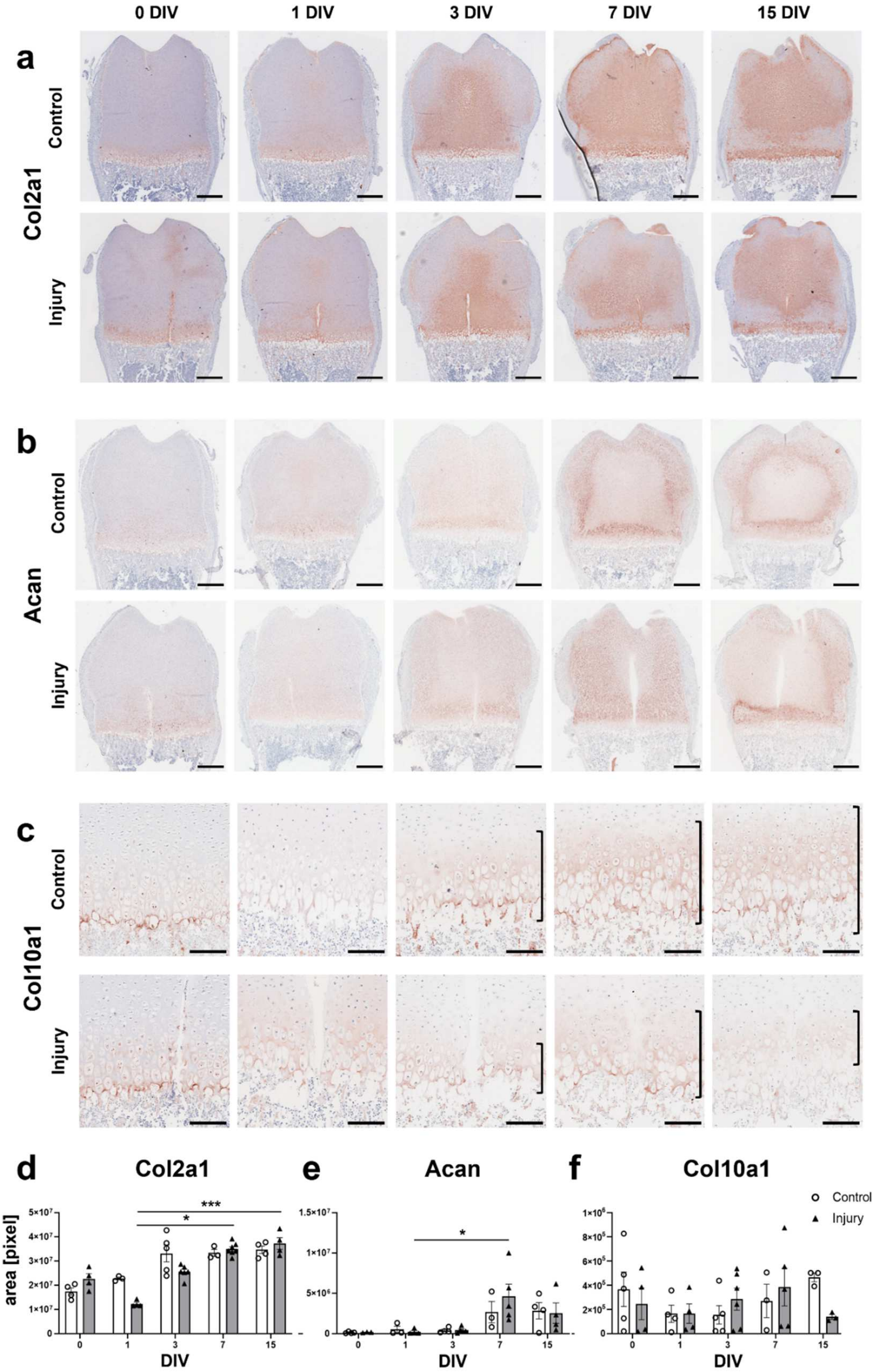

Figure 21. Injury-associated augmentation of the extracellular matrix (ECM) composition during endochondral ossification. a-c) Representative images of chondrocyte maturation stages analyzed by the immunohistochemistry (IHC) staining of ex vivo bone cultures (OTC) of type II collagen (Col2a1, representing committed chondrocytes), aggrecan (Acan, representing metabolically active chondrocytes), and type X collagen (Col10a1, representing hypertrophic chondrocytes) at 0, 1, 3, 7, and 15 days of in vitro cultivation (DIV).; black bracket – hypertrophic zone; Red – positive staining. Scale bar: 500 µm, Col10a1: 150 µm. **d-f)** Quantification of positively stained pixels in IHC. Statistical significance of observed differences was assessed using the Kruskal-Wallis Test for temporal changes and the Mann-Whitney-U Test for injury vs. control comparisons. Data are presented as mean ± SEM with a minimum sample size of $n \geq 3$ animals per time point, 3 technical replicates. Significance levels are denoted as $^{*}p \leq 0.05$, $^{**}p \leq 0.01$ and $^{***}p \leq 0.001$; circles (controls, white) and triangles (injury, grey). Reproduced from [1] under the terms of CC BY.

We conducted additional assessments to evaluate the gene expression levels of ECM proteins, namely Col1a1, Col2a1, and Col10a1, as well as the principal proteolytic enzyme Mmp13 (Fig. 22a-d). Our findings revealed significant differences between the injured and control OTCs at 0 DIV for Col1a1 ($p = 0.045$). However, the gene expression was stable during the cultivation time and no significant differences were observed at other time points (Fig. 22a). The expression of the Col2a1 gene remained relatively stable throughout the cultivation period, except at 3 DIV when expression decreased in both conditions (Fig. 22b). Notably, the primary proteolytic enzyme for Col2a1, Mmp13, exhibited increased expression at 3 DIV (Fig. 22d). Moreover, at 15 DIV, Mmp13 expression in the injured OTC showed a highly significant upregulation compared to the control OTC ($p = 0.006$). The gene expression of Col10a1 consistently decreased throughout the cultivation time, except at 3 DIV, although no significant differences were observed between the conditions (Fig. 22c).

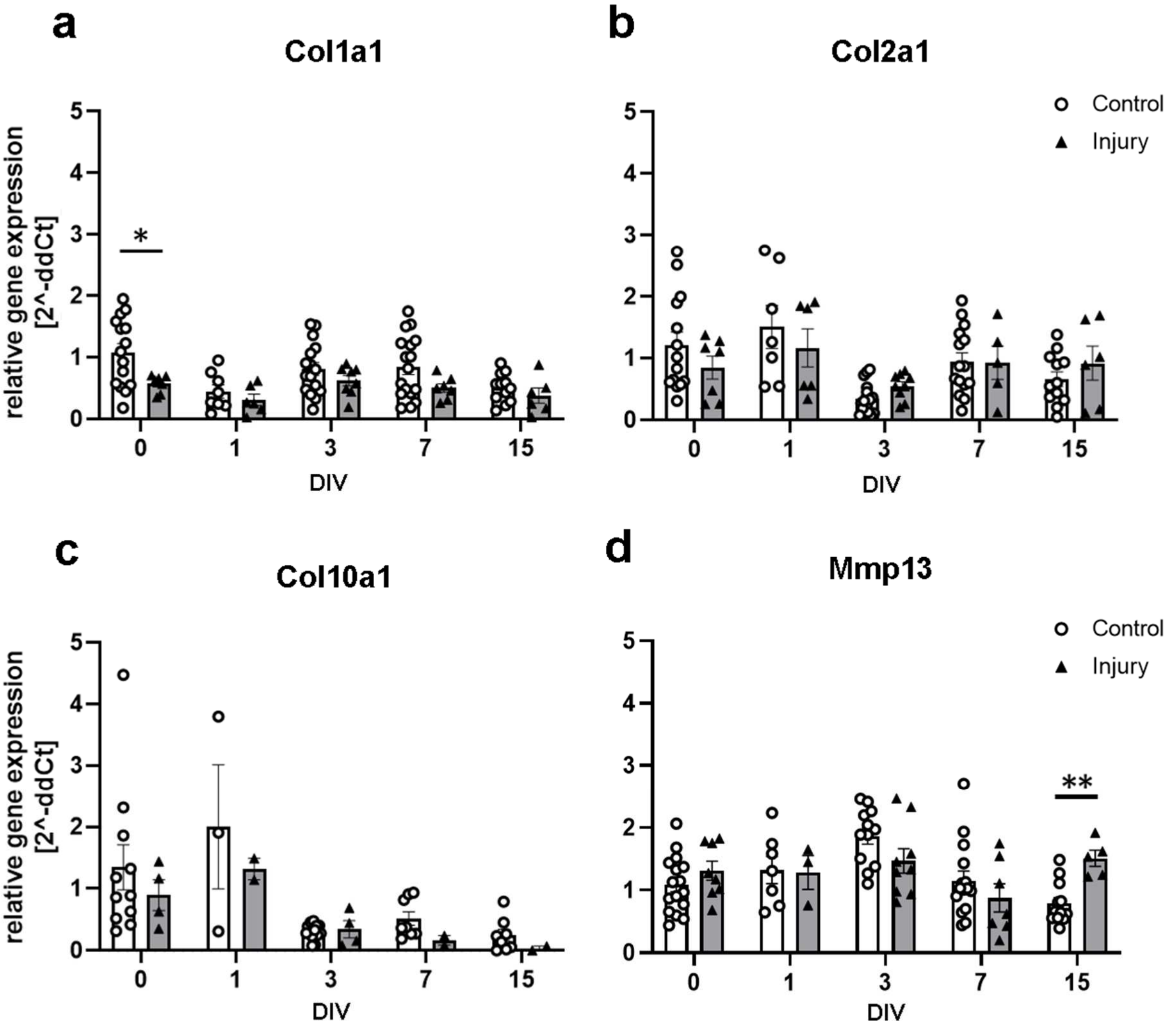

Figure 22. Growth plate injury (GPI) has no effect on extracellular matrix (ECM) genes expression. a-d) Gene expression levels of type I collagen (Col1a1), type II collagen (Col2a1), type X Collagen (Col10a1) and proteolytic enzyme collagenase 3 (metalloproteinase 13, Mmp13) was evaluated by real time PCR (RT-PCR) at 0, 1, 3, 7, and 15 days of in vitro cultivation (DIV). Statistical significance was assessed using the Mann-Whitney-U Test for injury vs. control comparisons. Data are presented as mean ± SEM with a minimum sample size of n ≥ 4 animals per time point (exception 1 DIV Col10a1), 3 technical replicates. Significance levels are denoted as *p ≤ 0.05, **p ≤ 0.01 and ***p ≤ 0.001; circles (controls, white) and triangles (injury, grey). Relative gene expression – gene expression normalized to 0 DIV control, which is set to 1.

3.6 Growth plate injury (GPI) enhances chondrogenesis over osteogenesis

Within the growth plate, physiological chondrogenesis plays a central role in driving longitudinal bone growth. To accomplish this, multiple regulatory processes have to simultaneously work tightly coordinated. One crucial feedback loop involved in the regulation of chondrocyte proliferation and differentiation is the interaction between Ihh and PTHrP. In our OTC the expression of the PTHrP gene remained relatively stable throughout the cultivation time, with the exception of a notable decrease at 7 DIV (Fig. 23a). In contrast, Ihh gene expression exhibited significant fluctuations. Initially, there was a sharp increase at 1 DIV, followed by a return to the baseline at 3 DIV (Fig. 23b). Interestingly, injured OTCs showed a substantial upregulation of Ihh gene expression at 7 and 15 DIV compared to the respective control (7 DIV: $p = 0.025$; 15 DIV: $p = 0.0004$), indicating a distinct response to injury. In addition, injured OTCs exhibited a significantly lower expression of PthrP compared to control OTCs at 7 DIV ($p = 0.02$).

Bmp-2 plays a role in promoting cell survival and proliferation in chondrocytes and stem cells, while also stimulating extracellular matrix (ECM) production to aid in the repair of injured tissue. Our findings demonstrated a significant initial increase in Bmp-2 expression at 1 DIV, followed by a return to the original levels for the remaining cultivation period (Fig. 23d).

Sox9, Runx2, and Osx are transcription factors that play critical roles in cell differentiation processes during skeletal development. Sox9 is involved in promoting the differentiation of stem cells towards the chondrocyte lineage, while Runx2 plays a crucial role in driving chondrocytes towards hypertrophic differentiation and facilitating the expression of genes essential for matrix mineralization. Osx, in turn, is responsible for the trans differentiation of hypertrophic chondrocytes into osteoblasts, contributing to the formation of bone tissue. In our in vitro cultivation, we observed a profound and consistent increase in Sox9 gene expression throughout the cultivation period, with a slightly less pronounced increase at 3 DIV (Fig. 23f). At 15 DIV, injured OTCs exhibited a significantly higher expression of Sox9 compared to the control ($p = 0.004$). Conversely, Runx2 gene expression remained relatively stable throughout the cultivation period, with no significant differences detected between the injured and control OTCs (Fig. 23e). Downstream of Runx2, Osx demonstrated an initial steep increase in gene expression up to 3 DIV, followed by a slight decrease until 15 DIV (Fig. 23g). However, no statistical differences were observed between the two conditions.

The proteins Opn and Oc are important for the cartilage-to-bone transition and the matrix mineralization process. Injured OTCs exhibited a significant decrease in Opn gene expression compared to the respective controls at 3 DIV (p = 0.039) and 7 DIV (p = 0.035) (Fig. 23h). This indicates a notable reduction in Opn levels in the injured OTCs during these time points. Oc gene expression showed a substantial initial decrease that persisted throughout the remaining cultivation period (Fig. 23i). This indicates a sustained downregulation of Oc gene expression in both the injured and control OTCs.

Notably, we further observed a profound initial increase in Vegfa expression in both conditions which decreased over rest of the cultivation period (Fig. 23c). Interestingly, at 3 DIV the injured OTC showed a significant decreased Vegfa expression compared to the control (p = 0.007).

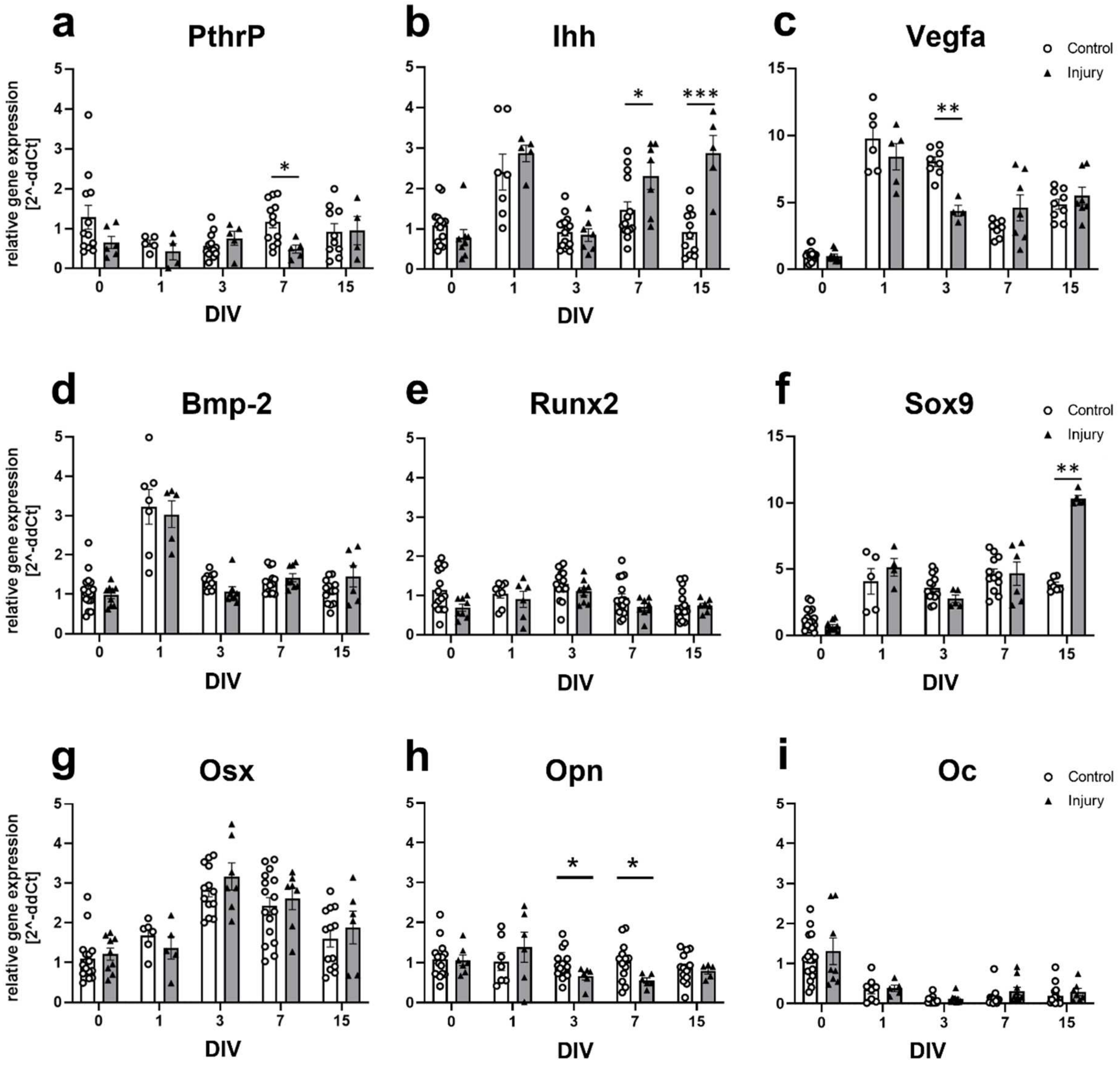

Figure 23. Chondrogenesis gene expression was altered due to growth plate injury (GPI) within an ex vivo femur slice culture (OTC). a-i) Gene expression levels of Parathormon-related protein (PthrP), Indian hedgehog (Ihh), Vascular endothelial growth factor A (Vegfa),

Bone morphogenetic protein-2 (Bmp-2), SRY-box transcription factor 9 (Sox9), Runt-related transcription factor 2 (Runx2), Osterix (Osx, SP7), Osteopontin (Opn, Spp1) and Osteocalcin (Oc, Bglap) were evaluated by real time PCR (RT-PCR) at 0, 1, 3, 7 and 15 days of in vitro cultivation (DIV). Statistical significance was assessed using the Mann-Whitney-U Test for injury vs. control comparisons. Data are presented as mean ± SEM with a minimum sample size of $n \geq 4$ animals per time point, 3 technical replicates. Significance levels are denoted as $^{*}p \leq 0.05$, $^{**}p \leq 0.01$ and $^{***}p \leq 0.001$; circles (controls, white) and triangles (injury, grey). Relative gene expression – gene expression normalized to 0 DIV control, which is set to 1.

Further, the expression and distribution patterns of transcriptions factors and proteins Bmp-2, Runx2, Osx, Sox9 and Ogp were evaluated by IHC (Fig. 24a-d) and we again had a closer look at the distinct zones of 7 and 15 DIV OTC's for Bmp-2, Runx2, Osx and 3, 7 and 15 DIV for Sox9 as indicated by the coloured squares. Representative control images can be found in Fig. 46a.

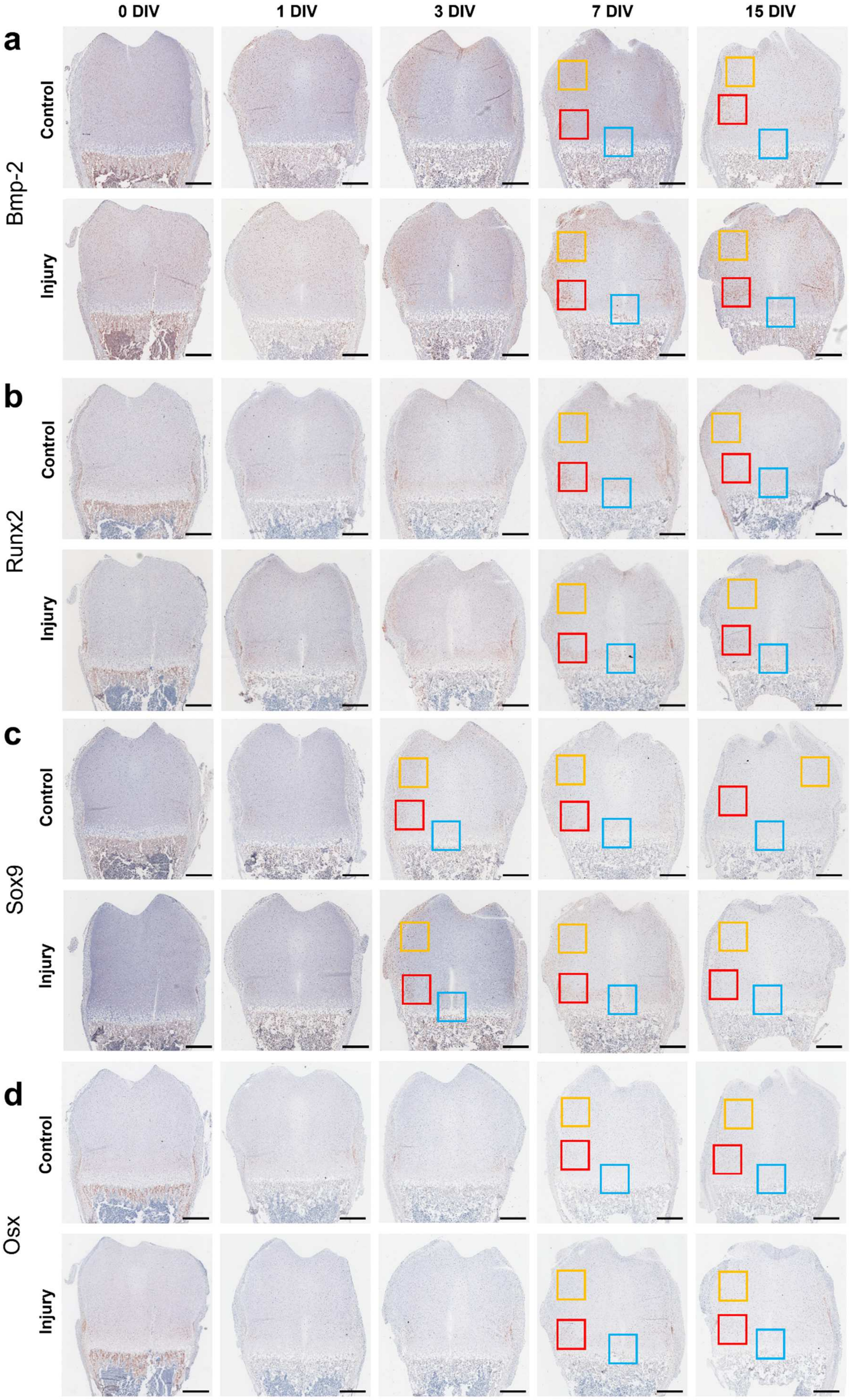
0 DIV
1 DIV
3 DIV
7 DIV
15 DIV
a
Bmp-2
Control
Injury
b
Runx2
Control
Injury
c
Sox9
Control
Injury
d
Osx
Control
Injury

Figure 24. Endochondral ossification following growth plate injury (GPI). a-d) Representative images of proximal femurs of immunohistochemical staining (IHC) for the targets Bmp-2, Runx2, Sox9, and Osx are presented at 0, 1, 3, 7, and 15 days of in vitro cultivation (DIV) for both injured and control ex vivo organotypic femur slice cultures (OTCs). Coloured squares indicate the regions selected for closer examination: transition zone (TZ, yellow square), middle zone (MZ, red square), and deep zone (DZ, blue square). Red – positive staining. Scale bar: 500 µm

Regarding Bmp-2 expression, we observed increased Bmp-2 positive staining in the TZ and MZ of the injury group at both 7 and 15 DIV. In contrast, no significant differences in positive staining were observed between the injured and control groups in the DZ at these time points (Fig. 25a). Quantification of positive cell count exhibited no significant difference between injured and control OTC (Fig. 25b).

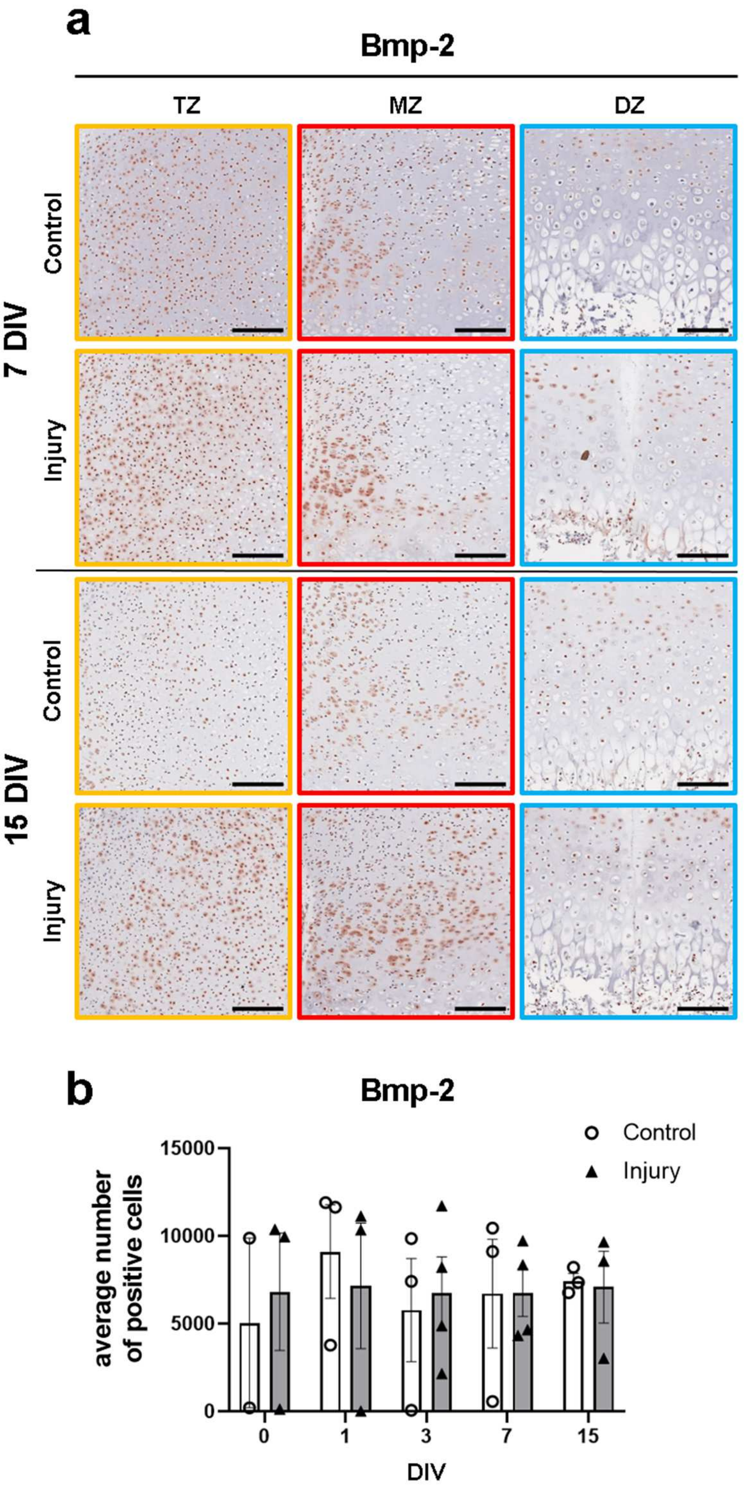

Figure 25. Master regulator Bone morphogenic protein 2 (Bmp-2) stimulates either chondrogenesis or osteogenesis in postnatal growth plate (GP). a) Representative images of immunohistochemistry (IHC) of target Bmp-2 of distinct zone: transition zone (TZ, yellow square), middle zone (MZ, red square) and deep zone (DZ, blue square) of the proximal

femur OTCs at 7 and 15 days of in vitro cultivation (DIV). Red – positive staining. Scale bar: 150 µm. **b)** Quantification of cell count in IHC. Statistical significance was assessed with the Mann-Whitney-U Test for injury vs. control comparisons. Data are presented as mean ± SEM with a minimum sample size of n ≥ 3 animals per time point used (exception 0 DIV control), 3 technical replicates. Significance levels are denoted as $^*p \leq 0.05$, $^{**}p \leq 0.01$ and $^{***}p \leq 0.001$; circles (controls, white) and triangles (injury, grey).

On the contrary, observed a decreased Runx2 positive staining in the GPI OTCs compared to the respective control group. This decrease in staining was observed in the TZ at both 7 and 15 DIV (Fig. 26a). Within the MZ, we detected pronounced and strong nuclear staining of proliferating chondrocytes at 7 DIV, but the area of positive staining was lower in the injured OTC compared to the control OTC. In the DZ, both the injured and control OTCs exhibited similar strong nuclear positive staining of pre-hypertrophic chondrocytes at 7 and 15 DIV. To quantify the Runx2 positive cells in the proximal epiphysis, we performed cell counting. Interestingly, we found no significant differences in the number of Runx2 positive cells between the injured and control OTCs at the specific time points assessed (Fig. 26b).

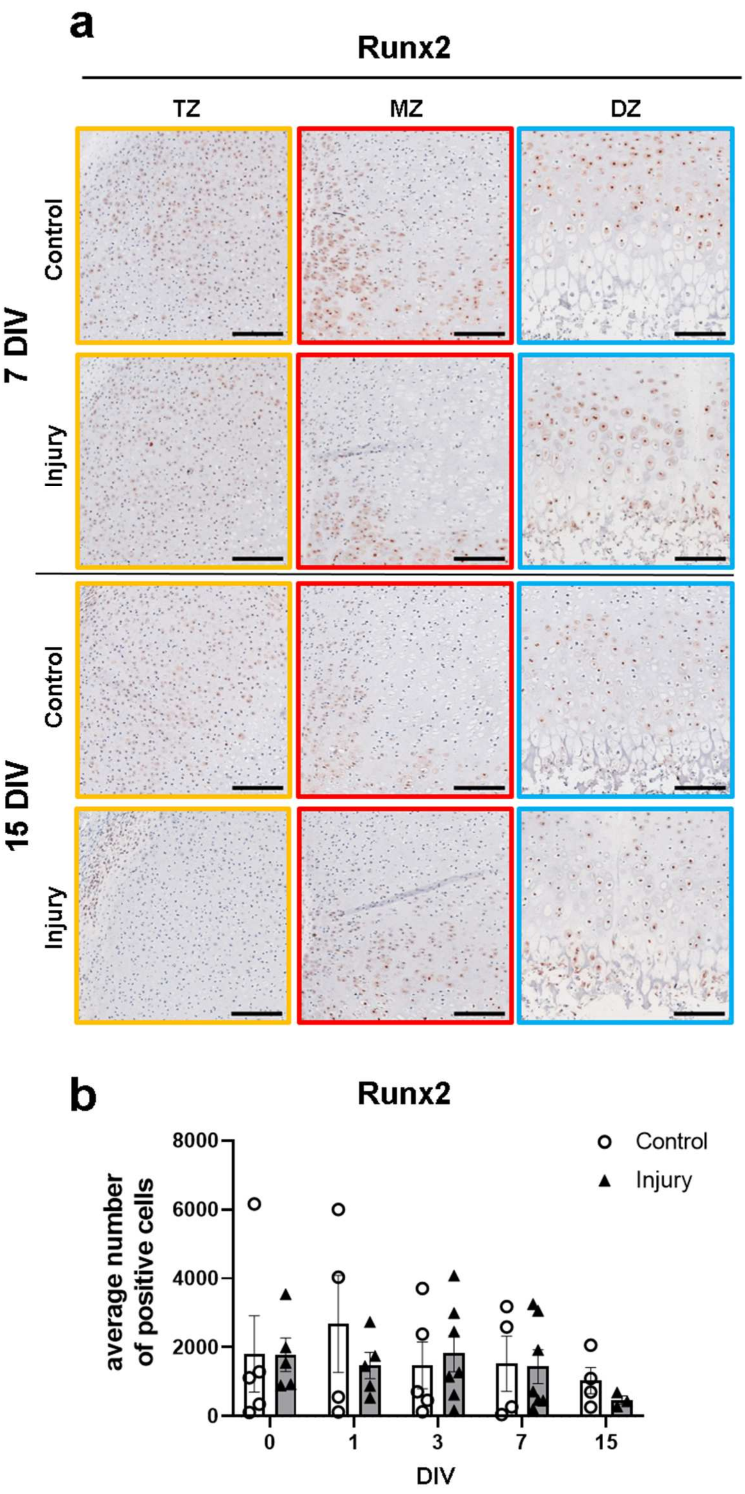

Figure 26. Decreased terminal hypertrophic differentiation due to decreased Runt-related transcription factor 2 (Runx2) after growth plate injury (GPI). a) Representative images of immunohistochemistry (IHC) of Runx2 of distinct zone: transition zone (TZ, yellow square), middle zone (MZ, red square) and deep zone (DZ, blue square) of the proximal femur

OTCs at 7 and 15 days of in vitro cultivation (DIV). Red – positive staining. Scale bar: 150 µm. **b)** Quantification of cell count in IHC. Statistical significance was assessed with the Mann-Whitney-U Test for injury vs. control comparisons. Data are presented as mean ± SEM with a minimum sample size of n ≥ 3 animals per time point used, 3 technical replicates. Significance levels are denoted as $^{*}p \leq 0.05$, $^{**}p \leq 0.01$ and $^{***}p \leq 0.001$; circles (controls, white) and triangles (injury, grey).

In our OTCs neither the injured nor the control OTCs showed any positive staining for Osx at 7 or 15 DIV within the TZ (Fig. 27a). However, in the MZ, we observed Osx positive staining in proliferating chondrocytes, with a higher intensity in the injured OTC compared to the control. Notably, at 7 DIV in the DZ, we observed strong nuclear staining of pre-hypertrophic and hypertrophic chondrocytes, as well as bone marrow cells at the metaphyseal junction in the injured OTC, while the control OTC showed no positive staining. At 15 DIV, both conditions displayed some Osx positive cells. To quantify the Osx positive cells in the proximal epiphysis, we conducted cell counting. We observed a steep decrease in the number of Osx positive cells in the control OTC from 7 DIV onwards, whereas in the injured OTC, the decrease in cell number was only evident at 15 DIV (Fig. 27b). However, no statistically significant differences between the conditions were detected in terms of Osx positive cell counts.

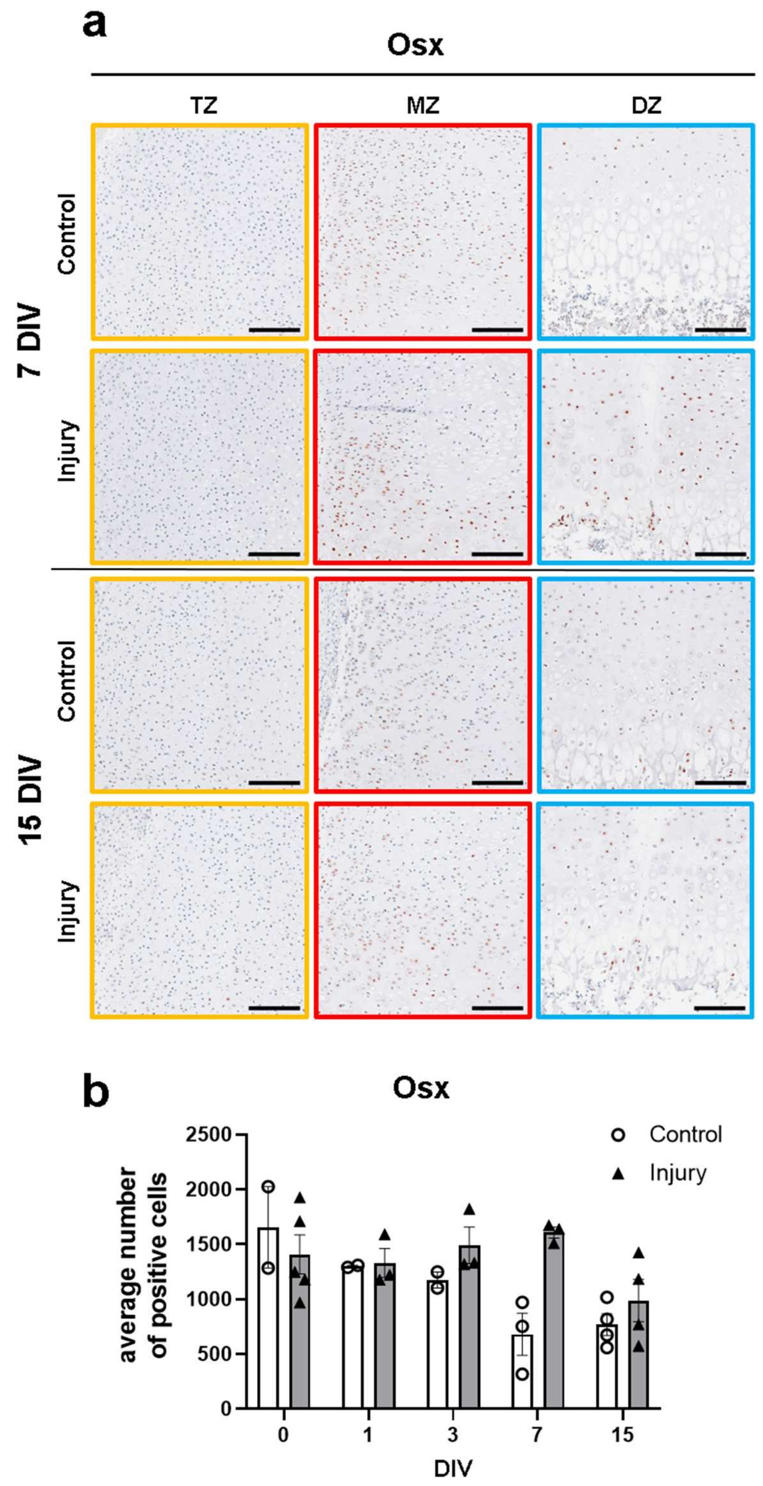

Figure 27. Increased hypertrophic differentiation through Osterix (Osx) after growth plate injury (GPI). a) Representative images of immunohistochemistry (IHC) of Osx of distinct zone: transition zone (TZ, yellow square), middle zone (MZ, red square) and deep zone (DZ, blue square) of the proximal femur OTCs at 7 and 15 days of in vitro cultivation (DIV). Red –

positive staining. Scale bar: 150 µm. **b)** Quantification of cell count in IHC. Statistical significance was assessed with the Mann-Whitney-U Test for injury vs. control comparisons. Data are presented as mean ± SEM with a minimum sample size of n ≥ 3 animals per time point used (exception control 0, 1 and 3 DIV), 3 technical replicates. Significance levels are denoted as *p ≤ 0.05, **p ≤ 0.01 and ***p ≤ 0.001; circles (controls, white) and triangles (injury, grey).

In our OTCs Sox9 was detected in chondrocytes across all distinct zones, exhibiting robust expression at 3 and 7 DIV, which subsequently attenuated by 15 DIV (Fig. 28a). Particularly noteworthy was the heightened Sox9 expression within the MZ at 3 and 7 DIV subsequent to GPI, as compared to the corresponding control. However, positive cell count did not reveal a significant difference between injured and control OTC (Fig. 28b).

a

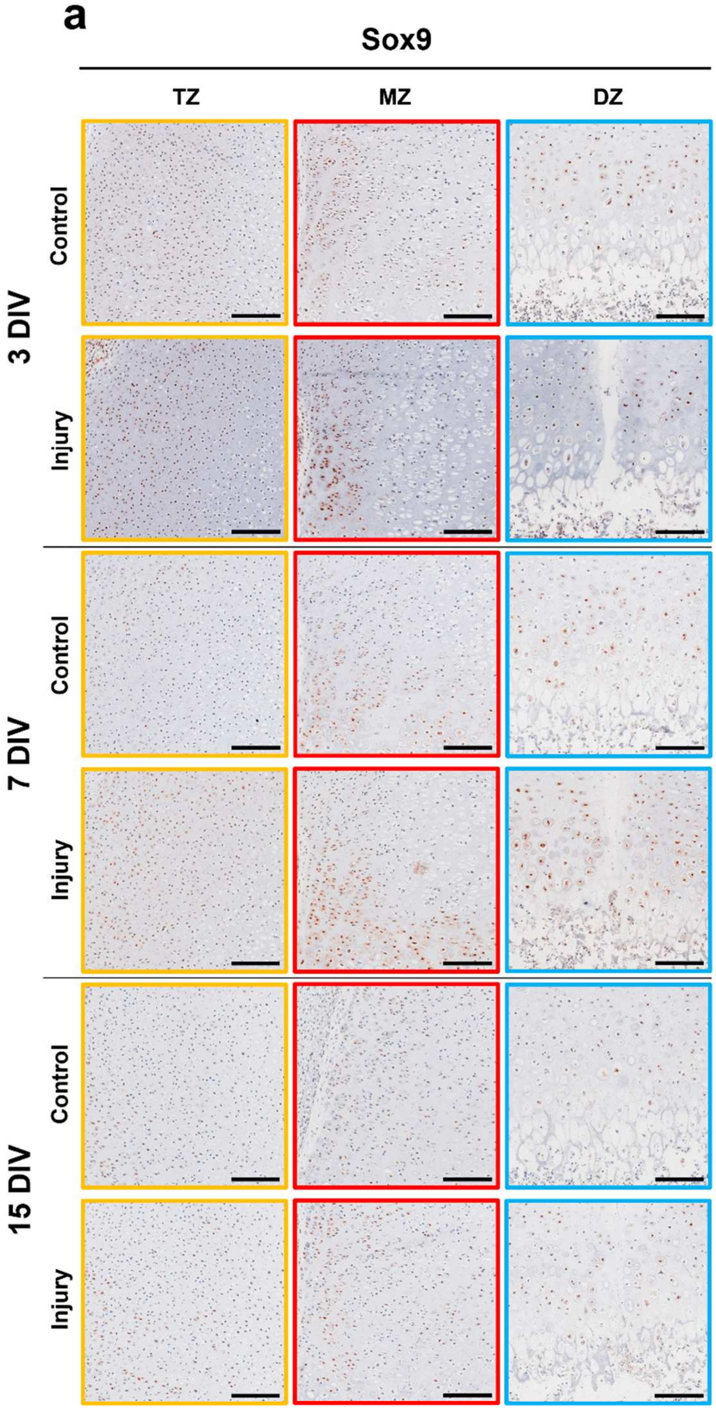
Sox9
TZ
MZ
DZ
3 DIV
Control
Injury
7 DIV
Control
Injury
15 DIV
Control
Injury

b

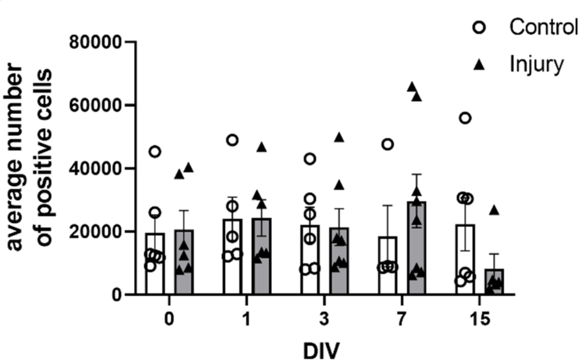
Sox9
Control
Injury
average number of positive cells
80000
60000
40000
20000
0
0
1
3
7
15
DIV

Figure 28. Stimulation of chondrogenesis due to growth plate injury (GPI) in an ex vivo bone culture (OTC). a) Representative images of immunohistochemistry (IHC) of Sox9 of distinct zone: transition zone (TZ, yellow square), middle zone (MZ, red square) and deep zone (DZ, blue square) of the proximal femur OTCs at 3, 7, and 15 days of in vitro cultivation (DIV). Red – positive staining. Scale bar: 150 µm. **b)** Quantification of Sox9 positive cell count of the IHC. Statistical significance with the Mann-Whitney-U Test for injury vs. control comparisons. Data are presented as mean ± SEM with a minimum sample size of n ≥ 3 animals per time point used, 3 technical replicates. Significance levels are denoted as *p ≤ 0.05, **p ≤ 0.01 and ***p ≤ 0.001; circles (controls, white) and triangles (injury, grey).

Moreover, we evaluated osteogenesis by utilizing the mature osteoblast marker Opn. Within this context, a heightened Opn expression was discerned along the perichondrium during the entire cultivation period; however, it reached its peak at 7 DIV and gradually diminished by 15 DIV (Fig. 29). Within the trabecular spicules, a sustained and escalating Opn expression was observed until 7 DIV, maintaining this level by 15 DIV. Notably, at 7 DIV, a significantly greater positive Opn expression was evident within the injured OTCs in comparison to the corresponding control. Representative control images can be found in Fig. 46a.

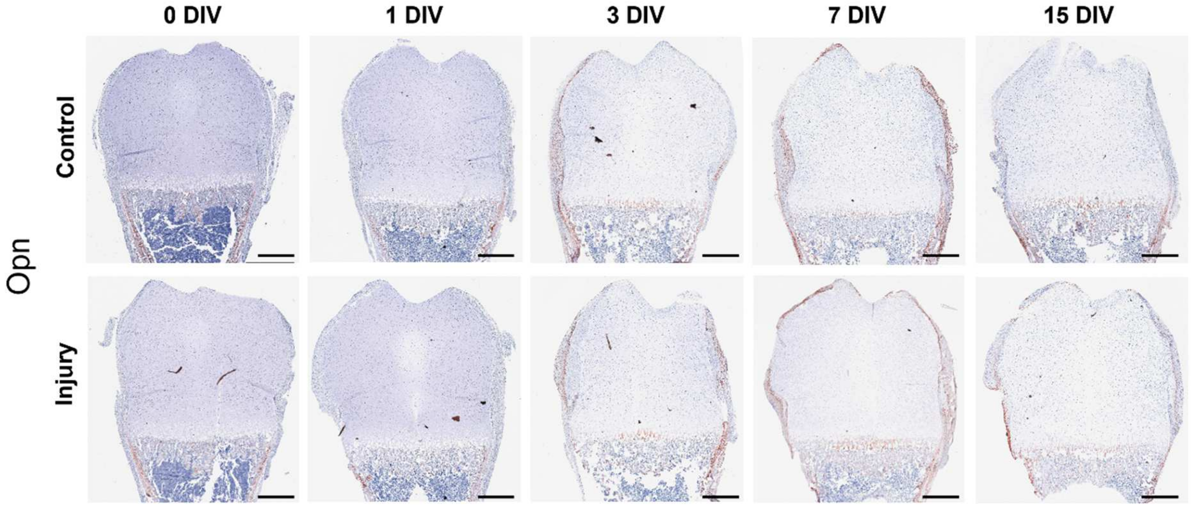

Figure 29. Osteogenesis was induced within the trabecular spicules due to growth plate injury (GPI) within an ex vivo bone culture (OTC). Representative images of proximal femurs of immunohistochemical staining (IHC) of Opn are presented at 0, 1, 3, 7, and 15 days of in vitro cultivation (DIV) for both injured and control OTCs. Red – positive staining. Scale bar: 500 µm

3.7 GPI influence on osteoclastogenesis

The evaluation of TRAP staining of osteoclasts, provided valuable information about osteoclast maturation and activity during GPI repair and postnatal endochondral ossification (Fig. 30). TRAP staining revealed an initial profound decrease in osteoclast number from 0 to 1 DIV (Fig. 30a, black arrows). A light decrease in staining intensity and therefore osteoclast activity over the cultivation time for both conditions was observed, however, no statistical differences were detected (Fig. 30b). Gene expression analyses of TRAP coincided with the gathered TRAP staining and cell count data (Fig. 30c). After an initial steep decline in expression, there is a slow and steady decrease over the remaining cultivation period in both conditions with no significant differences between the two at the specific time points.

The osteoclast formation and activation are mainly regulated via the RankL-Rank-Opg-pathway. Therefore, we analyzed these targets on gene expression levels (Fig. 30d-f). Opg expression experienced a constant increase over the cultivation time for both conditions (Fig. 30d). Up until 15 DIV the control exhibited a higher Opg gene expression level than the injured OTC, which changed at this time point. We further detected that at 0 DIV Opg was significantly lower expressed than the control OTC ($p = 0,037$). Contrary, RankL gene expression experienced an initial increase at 1 DIV but a steep and continuous decreased over the following cultivation period was detected for both conditions with no significant differences between injured and control OTCs (Fig. 30e). The receptor Rank exhibited a profound decrease in gene expression over the cultivation period and no significant differences were detected between both conditions (Fig. 30f).

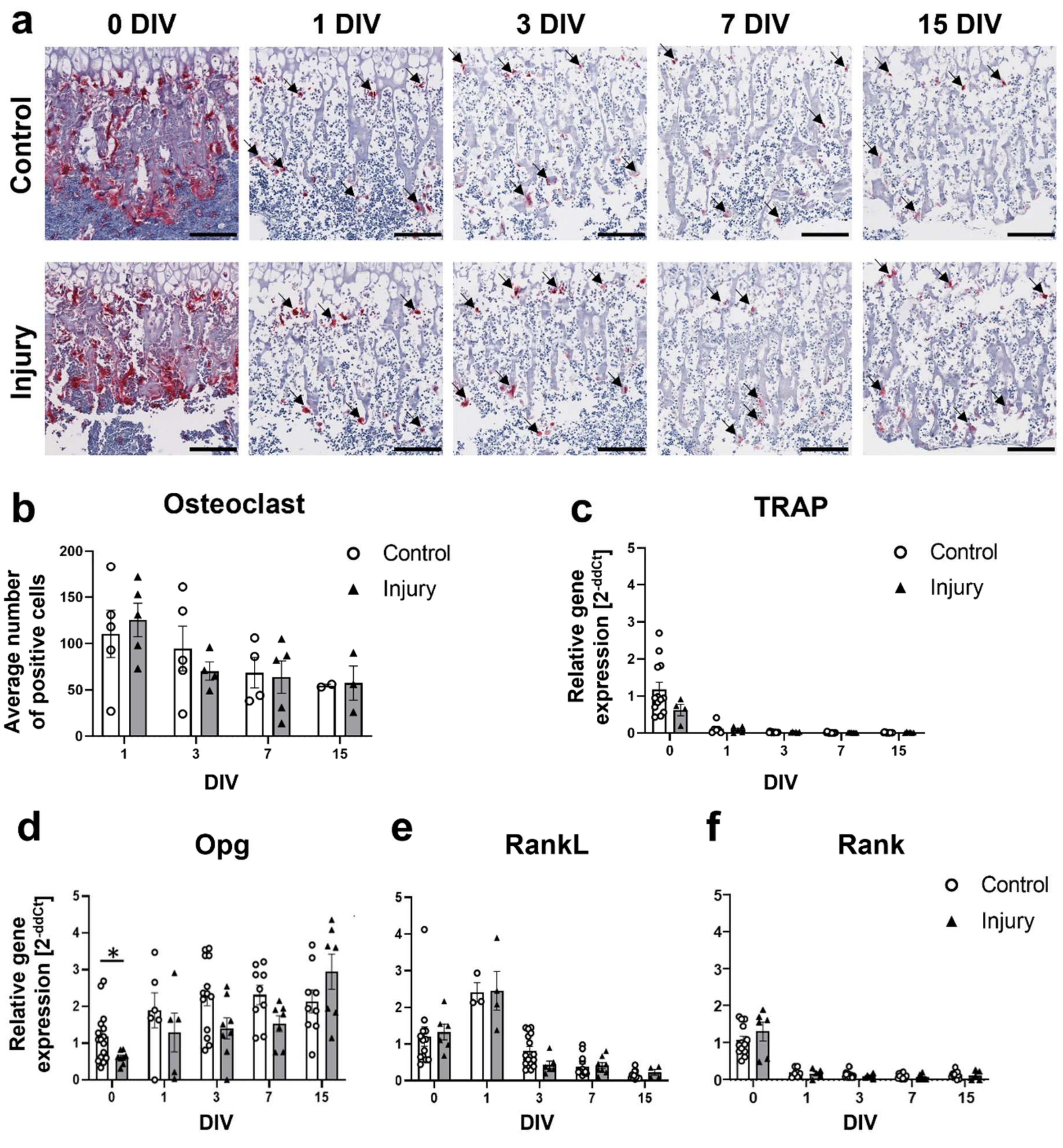

Figure 30. Growth plate injury (GPI) does not affect osteoclast (OC) number and activity. Osteoclasts within the trabecular spicules were detected by tartrate-resistant acid phosphatase (TRAP) staining. **a)** Representative images of trabecular spicules of the proximal femur bone slice cultures (OTS) with and without GPI at 0, 1, 3, 7 and 15 days of cultivation (DIV). Black arrows – osteoclasts; Scale bar: 150 µm. **b)** Quantification of osteoclast cell count within the trabecular spicules. Data are presented as mean ± SEM with a minimum sample size of n ≥ 3

animals per time point used (exception 15 DIV control), 3 technical replicates; circles (controls, white) and triangles (injury, grey). **c-f)** Gene expression analysis of TRAP, Opg, RankL and Rank by real time PCR (RT-PCR). Statistical significance of observed differences was assessed using the Whitney-U Test for injury vs. control comparisons. Data are presented as mean ± SEM with a minimum sample size of n ≥ 4 animals per time point used (exception RankL 1 DIV), 3 technical replicates. Significance levels are denoted as $^{*}p \leq 0.05$, $^{**}p \leq 0.01$ and $^{***}p \leq 0.001$; circles (controls, white) and triangles (injury, grey). Relative gene expression – gene expression normalized to 0 DIV control, which is set to 1.

Finally, the expression and distribution patterns of Opg was evaluated by immunohistochemistry (Fig. 31) and we again had a closer look at the distinct zones at 7 and 15 DIV as indicated by the coloured squares. Representative control images can be found in Fig. 46a.

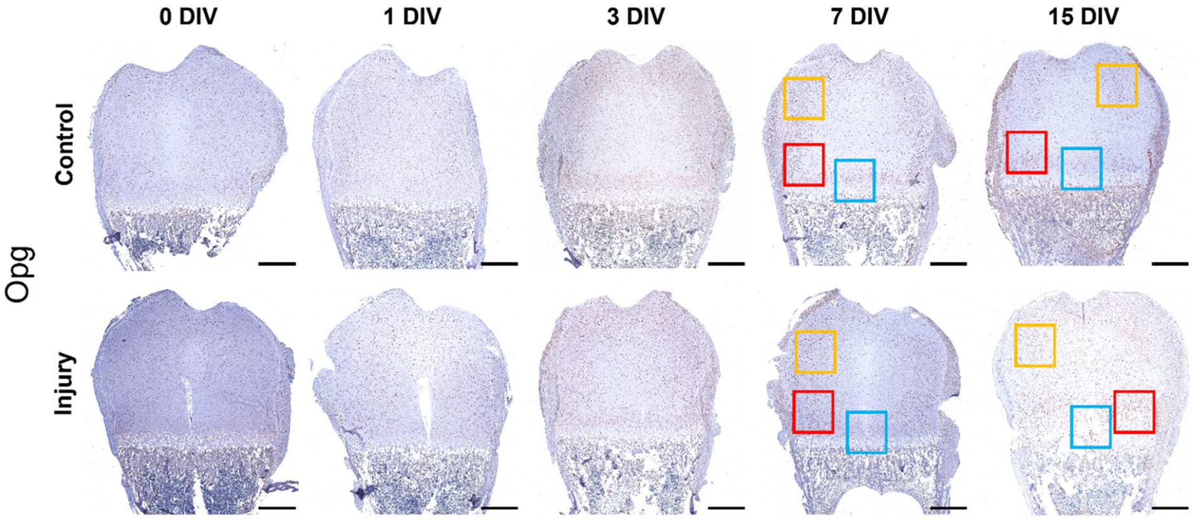

Figure 31. Opg expression by chondrocytes was evaluated. Representative images of proximal femurs of immunohistochemical staining (IHC) of Opg are presented at 0, 1, 3, 7, and 15 days of in vitro cultivation (DIV) for both injured and control OTCs. Coloured squares indicate the regions selected for closer examination: transition zone (TZ, yellow square), middle zone (MZ, red square), and deep zone (DZ, blue square). Red – positive staining. Scale bar: 500 µm

A detailed examination of the discrete zones unveiled a broader dispersion of Opg expression at 7 DIV specifically within the MZ as a consequence of the injury, in contrast to the control OTC (Fig. 32). This pattern was similarly apparent at 15 DIV, extending to both the TZ and MZ, where an elevated Opg expression was noted within the injured OTC when compared to the corresponding control.

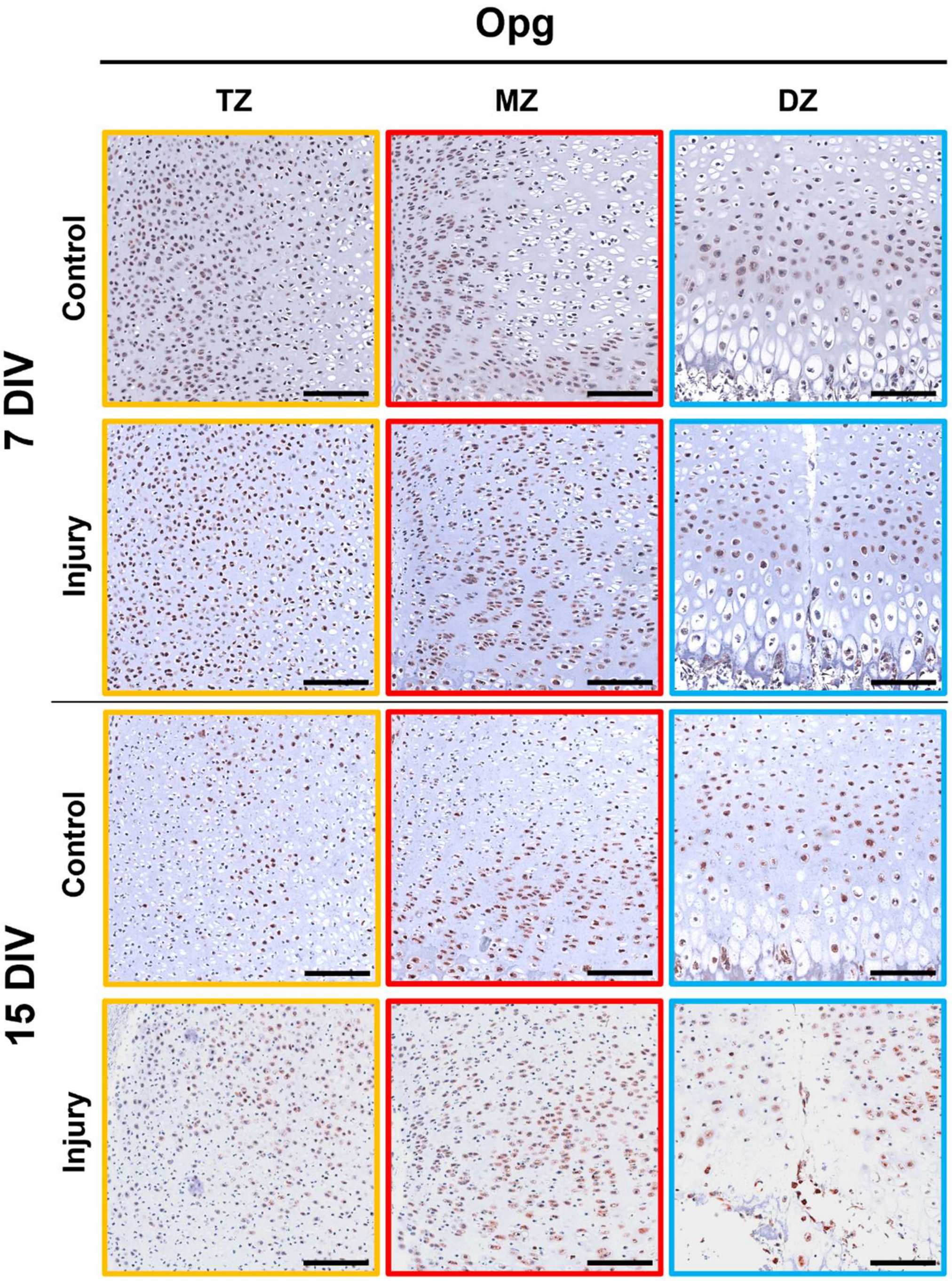

Figure 32. Growth plate injury (GPI) enhances Osteopotegerin (Opg) protein expression within the ex vivo bone culture (OTC). Representative images of immunohistochemistry (IHC) of Opg of distinct zone: transition zone (TZ, yellow square), middle zone (MZ, red square)

and deep zone (DZ, blue square) of injured and control OTCs at 7 and 15 days of in vitro cultivation (DIV). Red – positive staining. Scale bar: 150 µm.

3.8 Staining variability between experiments

Histological and IHC staining's of OTC from different animals (experiments) are subject to a certain degree of variability. To demonstrate the variability between the animals concerning histological staining, HE staining of 7 DIV control and injured OTC (Fig. 33) as well as IHC staining´s of Bmp-2 (Fig. 34) and Col2a1 (Fig. 35) of 3 -15 DIV of control and injured OTC are presented. Within the HE staining, we observed the same trend concerning endochondral ossification within most of our OTC. However, in a couple of animals, e.g. 7 DIV control Exp. 2, we observed a different morphological pattern. For IHC staining`s (Bmp-2 – Fig. 34 and Col2a1 – Fig. 35), we again observed the same staining pattern trend in the independent experiments, however, staining intensity did vary due to the methodical execution (AEC incubation time not long enough).

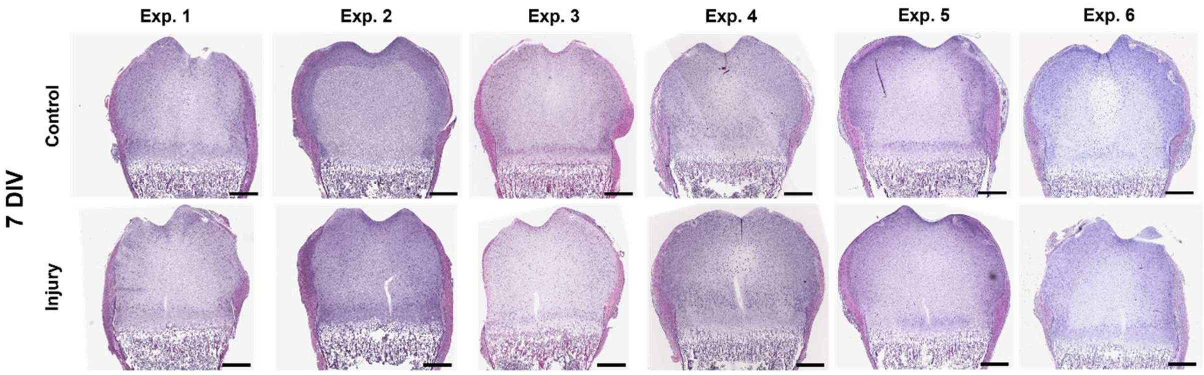

Figure 33. Proximal femurs overview of histological staining variability. Control and injured OTC at 7 DIV from 6 independent experiments were stained with Hematoxylin and Eosin (H&E) staining. Proximal femurs are presented. Scale bar = 500 µm.

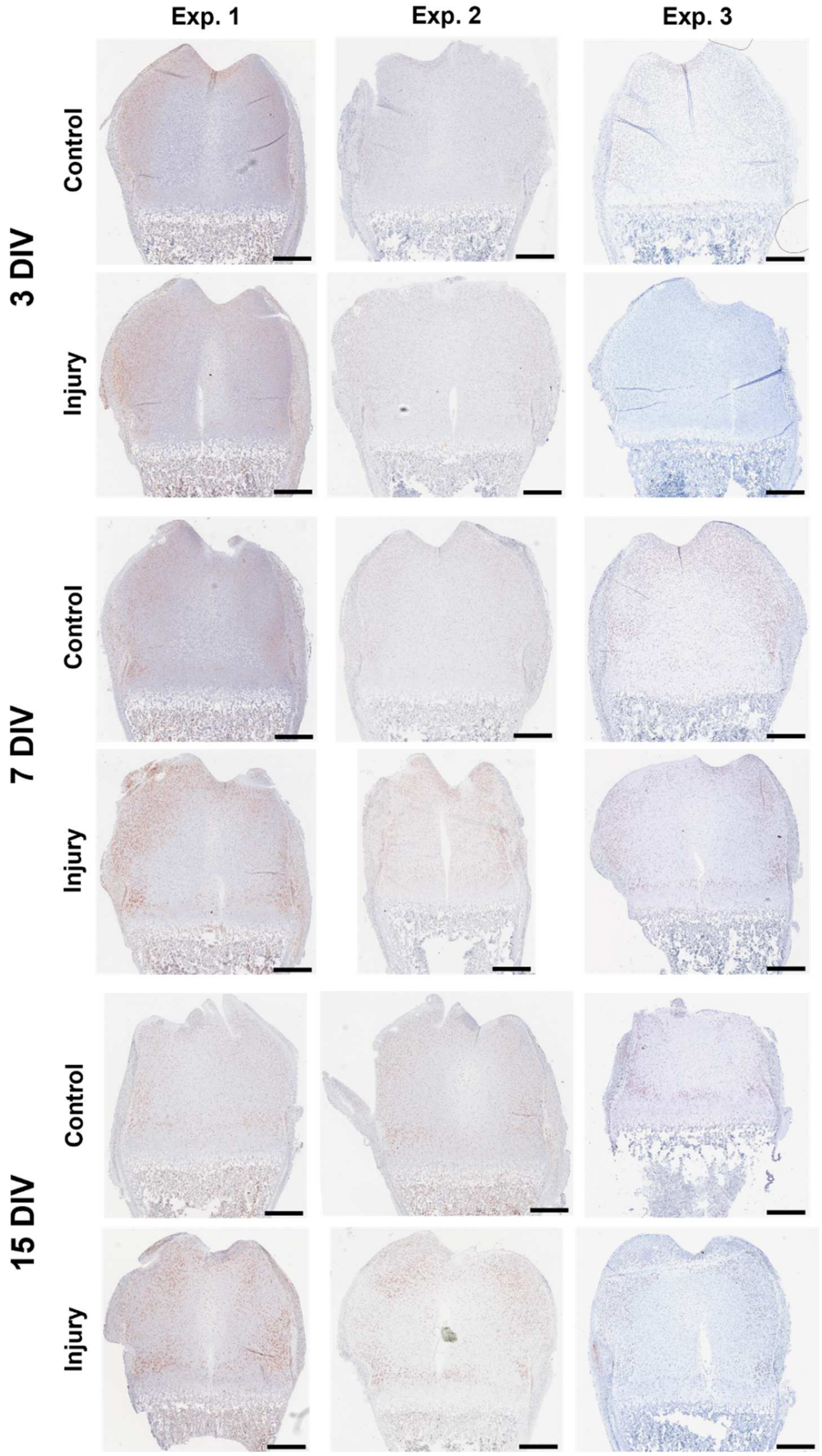

Figure 34. Proximal epiphysis overview of immunohistochemically staining (IHC) variability. Control and injured OTC at 3, 7 and 15 DIV from 3 independent experiments were

stained with Bmp-2 and counterstained with hematoxylin. Red – positive staining. Scale bar = 500 µm.

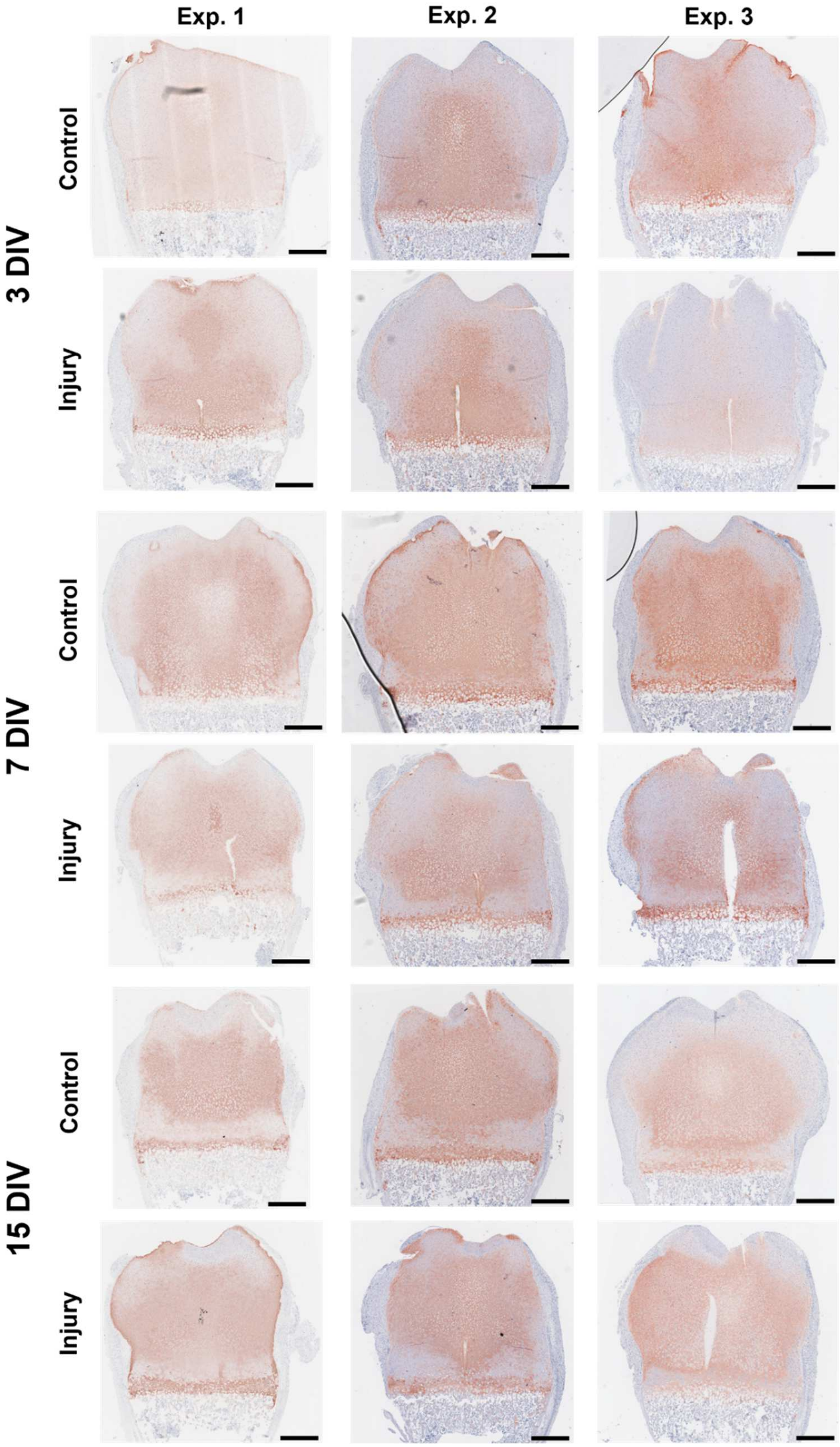

Figure 35. Proximal epiphysis overview of immunohistochemically staining (IHC) variability. Control and injured OTC at 3, 7 and 15 DIV from 3 independent experiments were

stained with Col2a1 and counterstained with hematoxylin. Red – positive staining. Scale bar = 500 µm.

4 Discussion Part One

4.1 General Discussion

Bone elongation is achieved through the intricate process of chondrogenic maturation within the GP. Unfortunately, when the still active GP is involved in injury or disease the complications during regeneration can lead to impaired bone growth. The successful regeneration of GPI into its original cartilaginous and accurately structured form with physiological chondrogenesis is of utmost importance for maintaining uninterrupted postnatal bone development. However, the underlying molecular and cellular mechanisms involved in GPI repair have jet to be elucidated To investigate the impact of GPI on postnatal endochondral chondrogenic and osteogenic development and to explore the underlying molecular and cellular mechanisms involved in GPI repair, we utilized an ex vivo organotypic femur culture. In this experimental setup, an injury was deliberately induced through the GP, penetrating into the bone marrow cavity, resembling a Salter-Harris III or IV classification with subsequent exhaustive analyses of the injured and the non-injured area of the proximal epiphysis.

4.2 Regeneration following GPI within the OTC

Numerous studies utilizing different animal models were able to identify four distinct phases of GPI repair namely the inflammatory phase (days 1 - 3), fibrogenic phase (days 3 - 7), osteogenic phase (days 7 - 14) and remodelling phase (day 14 +) [86, 139]. Therefore, we choose the time points 0, 1, 3, 7 and 15 DIV to investigate the regeneration processes following GPI within our ex vivo bone culture.

Firstly, in unfixed live OTC we observed the formation of a cellular network at 7 DIV which covered the injured OTC at 15 DIV by Live/Dead staining seemingly originating from the groove of Ranvier. Closer evaluation of the injury area by histological staining revealed the elimination of injured tissue by 3 DIV. Moreover, cells and cell aggregates were seen within the injury cleft starting at 3 DIV and increased in size and number until 15 DIV. Specifically we first observed cell aggregates at 7 DIV within the hypertrophic chondrocyte layer and at 15 DIV within the upper part of the injury. Moreover, tissue surrounding the lesion as well as fibers spanning the injury cleft were positively stained for Col2a1 by IHC from 0 DIV throughout the 15 days cultivation period. We further observed proliferation but no apoptosis and BMP-2 positive IHC staining of cells within the injury area throughout the cultivation time period. Electron microscopy imaging of the injury cleft at 7 DIV further confirmed the presence of stem cells, fibroblast and chondrocytes as well as collagen fibers within the injury area. Taken all these data together we might have observed a possible movement of stem cells from the groove of Ranvier towards the injury cleft together with a possible migration of bone marrow cells upwards the injury cleft. In accordance with previous research, the current findings provide additional evidence supporting the concept that the groove of Ranvier functions not only as a stem cell niche but also harbours diverse populations of progenitor cells capable of migration towards the injury site [140, 141]. The involvement of stem cells during GPI repair is a highly researched topic and new insights are achieved regularly. For example Muruganandan et al discovered a distinct FoxA2+ stem cell on top of the RZ, beside the secondary ossification area, which upon injury expanded and produced physeal cartilage for GPI regeneration [142]. Moreover, Matsushita et al demonstrated that following injury, quiescent bone marrow-derived mesenchymal stem cells undergo a remarkable transformation in their identity, adopting a precursor cell state similar to that of skeletal stem cells, aiding with skeletal regeneration [143].

Although bone bridge formation is regularly observed after GPI of Salter Harris III – IV, we did not observe this occurrence in our ex vivo OTCs in our histological staining's. Upon comparison with other in vivo GPI models, three notable discrepancies emerge relative to our methodology: 1) the age of the animal at the time of GPI initiation, 2) the type of GPI and 3) the duration of observation subsequent to sustained GPI application [139, 144–147].

In our study we utilized 5 day old Sprague Dawley rats, introduced a 2 mm transphyseal injury from the later 2nd ossification centre through the GP and metaphysis into the bone marrow cavity with subsequent in vitro cultivation for 15 days. Other in vivo studies typically perform their experiments on 6 week old Sprague Dawley rats [139]. While in our study the 2nd ossification centre is not developed at the time of OTC preparation, in 6-week old rats it has not only been developed but reached its full maturity [148, 149].

Concerning the type of GPI, Fan et al. compared the traditional transversal GPI to the longitudinal GPI in rabbits. Interestingly they found bone bride formation in both group, but the longitudinal GPI reached more accurate and reliable bone bridge formation [150]. Furthermore, also Erickson et al performed longitudinal GPI within rats from the direction of the diaphysis through the GP into the epiphysis without damaging the articular cartilage [139]. Although they achieved a high rate of bone bridge formation, they also mention the lack of this occurrence in some bones due to uninjured GP or not sufficiently disrupting the GP.

Time of observed bone bridge formation is differently reported in the literature, starting as early as 7 days post injury to a full mature bone bridge at 14 days to 3 weeks post injury [79, 151, 152]. In our model we observed ongoing regeneration processes like newly synthesised fibrils, which were spanning over the injury area starting from 3 DIV onwards. However, we did not observe a mature bone bridge formation within our histological analysis. Nonetheless, we observed specific processes, such as decreased Col2a1 and Col10a1 protein secretion, which have been established in the literature as contributors to bone bridge development [79, 153]. Consequently, we hypothesize that the ongoing cultivation of our OTCs may be fostering bone bridge formation, however, our 15 days cultivation period is not sufficient for histological verification.

4.3 Disruption of GP organization after GPI

In addition to studying the regeneration processes of the GPI within the OTC, our investigation also focused on non-injured adjacent areas within the epiphysis and GP to understand potential changes in architecture and organization due to the injury. We performed histological analysis using H&E, Movat Pentachrome, and Safranin O-Fast Green staining, which revealed evident disturbances both in the local injury area and the distant non-injured areas of the proximal femur epiphysis. We observed a profound decrease of the hypertrophic zone together with a random distribution of chondrocyte maturation stages within the DZ, indicating an impairment in the normal maturation process of chondrocytes. Moreover, an area shift of proliferating chondrocytes and the formation of multicellular clusters instead of the ordered single columns due to GPI was noted, further illustrating the impact of the injury on the cellular dynamics and organization within the GP. Coleman et al. observed profound damage within the non-injured area in the epiphysis by the time bone bridge had formed. They detected also detected cellular disorganisation together with a significant reduction in GP thickness and volume [144]. Interestingly recent studies suggest that bone bridge formation might not be solely responsible for later growth disturbances and for the development certain areas within the GP have to be affected by the injury [154, 155]. The established correlation between the extent of GPI and the severity of negative complications is a well-documented phenomenon. However, emerging evidence suggests a distinctive pattern, indicating that damage primarily affecting the RZ leads to growth disturbances [79, 142, 156, 157]. This observation points towards the differential sensitivities of these distinct zones to injury and underscores the importance of understanding zone-specific responses to better comprehend the mechanisms underlying GPI and subsequent complications. The importance of the RZ during postnatal endochondral ossification is highlighted by Newton et al. [158] and Mizuhashi et al. [13].

Newton focused on chondrocyte clonality and observed the acquisition of self-renewal of chondroprogenitors within the RZ. They suggest a postnatal formation of a stem cell niche within the GP which serves as a constant supply of chondrocytes [158]. Mizuhashi et al., on the other hand, showed that postnatal growth is driven by a population of PTHrP-positive chondro-progenitors, which are located in the RZ and are able to facilitate the generation of chondrocytes without being consumed themselves [13].

4.4 Alteration in tissue maturation and extra cellular matrix composition due to GPI

Tissue composition undergoes significant alterations during the process of endochondral ossification. To evaluate the impact of GPI on tissue maturation, we conducted Movat-Pentachrome staining and Safranin O-Fast Green staining. Our findings demonstrate a pronounced disruption of endochondral ossification by 7 DIV spanning the entirety of the proximal epiphysis. Our data might indicate a premature mineralization within the TZ due to sustained GP injury. Furthermore, in this area we observed an increased population of chondrocytes exhibiting profound positive proteoglycan staining in both the capsular and territorial matrix due to the sustained GPI. Chondrocytes possess the ability to quickly adjust their metabolic activity in response to mechanical stress and/or sustained injury, thereby enhancing the resilience of cartilage against tough biomechanical forces and promoting regeneration following injury. Nevertheless, in cases of extensive injury, the reparative mechanisms are prone to falter, potentially culminating in degenerative processes such as osteoarthritis [159]. A study by Siffert et al. documented an elevation in chondrocyte metabolic activity within the articular and growth cartilage as a self-repair response subsequent to sustained injury. Furthermore, it was noted that this heightened metabolic activity was short lived and has the potential to contribute to degenerative modifications within the matrix [160].

4.5 Disruption of spatial ECM proteins due to GPI

Given the profound influence of GPI on ECM maturation during in vitro cultivation as well as the observed increased number of highly metabolic active chondrocytes, we conducted IHC and RT-PCR analyses to elucidate the specific expression patterns of ECM and chondrocyte maturation marker, namely Col2a1, Acan, Col10a1, and respective collagenase Mmp13. We identified an augmentation in chondrocyte metabolic activity, specifically in relation to matrix secretion. Furthermore, there was a visible impairment in the transition of chondrocytes into the hypertrophic state, which began at 3 DIV and reached its peak at 7 DIV due to the sustained GPI. Notably, chondrocytes residing in the TZ and the DZ appeared to modify their maturation status by altering their ECM expression patterns of Col2a1, Col10a1, and Acan following injury, as compared to non-injured OTC's.

The ECM comprises a complex network where collagens, along with proteoglycans and other proteins, bind together to enhance resistance against mechanical stresses, maintain physiological equilibrium, and exert a regulatory role akin to soluble signaling molecules [51]. Col2a1, the predominant collagen fibril found in the ECM of cartilage, is primarily secreted by proliferating and pre-hypertrophic chondrocytes [51, 161]. Col2a1 together with Acan, the main proteoglycan in the ECM of the GP bind to hyaluronic acid, growth factors and other molecules, allowing the cartilage tissue with the unique abilities [162]. In the course of chondrocyte maturation and the subsequent terminal hypertrophic stage, chondrocytes undergo a ~10-fold increase in cell volume before reaching apoptosis. This expansion plays a vital role in facilitating longitudinal bone growth. During this process, hypertrophic chondrocytes release Col10a1 into the ECM, thereby promoting calcification [163]. A reduction of Col2a1 positive staining distribution at 7 DIV in our OTCs due to the sustained GPI was observed. During growth plate maturation, the mineralization process begins, which is marked by a decrease in Col2a1 gene expression coupled with an increase in Col10a1 expression [164]. Our data, therefore, may indicate a premature initiation of growth plate mineralization due to the sustained GPI.

Furthermore, numerous studies have already highlighted the importance of local autocrine and paracrine regulation of growth factors, signaling molecules and transcription factors on the chondrocyte maturation and ossification [165]. Furthermore, the formation and degradation of the ECM is crucial in the development of GP chondrocytes and bone elongation. ECM degradation is primarily orchestrated by collagenolytic Mmps, with Mmp-13 serving as the primary collagen-degrading enzyme [166]. Furthermore, Mmp-13 is also crucial during vascularization and the columnar arrangement within the GP [167]. Interestingly, while we observed a failure to establish the "normal" distribution pattern of Col2a1 and Acan at 7 and 15 DIV in IHC, we did not observe differences in gene expression levels of these markers. However, we observed a highly significant upregulation of Mmp-13 gene expression due to the sustained GPI at 15 DIV compared to the respective control. These findings are consistent with the results of Pichler et al., who reported an increase in Mmp-13 gene expression in chondrocytes in vitro when exposed to harmful forces. In contrast, when applying physiological force, they initially observed a decrease in Mmp-13 expression; however, 24 h later, they also noted an increase in Mmp-13 expression in this group [168].

4.6 GPI enhances chondrogenesis over osteogenesis in the OTC's

Our findings clearly indicate a pronounced bias toward chondrogenesis as opposed to osteogenesis during the regeneration of a GPI in the ex vivo bone culture. This tendency is substantiated by the increased gene expression of Ihh alongside a decrease in PthrP levels following the GPI. In addition to the stimulation of chondrogenesis, we observed a significant downregulation of the mature osteoblast marker Opn following GPI at 3 and 7 DIV. Furthermore, the osteocyte marker Oc also exhibited profound downregulation at the gene expression level after 1 DIV for both injured and control OTCs throughout the cultivation period. Furthermore, in immunohistochemistry staining, we observed stronger Bmp-2 positive staining in the TZ and MZ due to the GPI at 7 and 15 DIV, with positive cell clusters at the junction of the hypertrophic to calcification zone at 7 DIV. Similarly, Sox9 exhibited more pronounced positive staining in the MZ at 3 and 7 DIV as a result of the GPI. Additionally, Osx positive staining also increased in the MZ and DZ in injured OTC at 7 and 15 DIV. In contrast, Runx2 positive staining decreased due to the sustained GPI.

It is well-documented that Ihh plays a crucial role in stimulating chondrocyte proliferation and facilitating their differentiation into pre-hypertrophic chondrocytes. [13, 169, 170]. Tao et al. conducted an investigation into Hedgehog (Hh) signaling in 4 weeks old male rats following a GPI [171]. While our observations revealed elevated Ihh gene expression levels at later time points, Tao et al. reported robust and high Ihh expression during the early stages. Additionally, they found that the upregulation of Hh signaling had a suppressive effect on undesired bone bridge formation. Ihh signaling plays a pivotal role in tissue regeneration and has been demonstrated to promote mesenchymal stem cell (MSC) differentiation toward the chondrogenic lineage, thus aiding in the recovery from injury [172, 173].

Moreover, Ihh and PthrP expression is directly regulated through Runx2 expression [174]. However, depending on the maturation state of the chondrocyte, the regulation through Runx2 varies. Runx2 primarily exerts its regulatory effect on Ihh and PthrP in resting chondrocytes, whereas in hypertrophic chondrocytes, gene expression does not appear to be affected [20, 24]. Rashid et al. additionally reported that increased expression of Ihh and PthrP in their Runx2$^{HC/HC}$ mice was accompanied by an increased number of pre-hypertrophic/hypertrophic chondrocytes within an enlarged growth plate [24]. In our ex vivo bone cultures, we observed significant regulation in both Ihh and PthrP gene expression, while Runx2 gene expression remained relatively stable throughout the cultivation time for both injured and control OTC's. Moreover, at 15 DIV, we observed a significant elevation in the transcription factor Sox9 gene expression following GPI. In the postnatal GP, Sox9 ensures the normal maturation of chondrocytes while preventing their dedifferentiation/redifferentiation into the osteoblastic lineage [22]. In contrast, Runx2 plays an opposing role and is required for the transdifferentiation of chondrocytes into osteoblasts [20]. The expression of Sox9 and its impact on chondrogenesis following GPI has exhibited variability across various studies. While we, along with others, observed an augmentation in Sox9 gene expression [29], divergent results have been reported by others, who observed a reduction in Sox9 expression and chondrogenesis, coupled with an increase in hypertrophy following GPI [80, 175]. It's noteworthy that both of these studies employed 5 or 6 weeks old Sprague Dawley rats compared to our 5-days old rats and utilized the drill hole methodology.

Interestingly, while Osx is recognized as a osteoblast precursor marker that lies downstream of Runx2, in chondrocytes of the GP it drives terminal cartilage differentiation and endochondral ossification [176]. Moreover, Osx also regulates Vegf activity [177] and the production of Mmp-13 through hypertrophic chondrocytes [178]. The increase in Osx positive staining following GPI, along with other data such as H&E staining, might indicate a premature differentiation of proliferating and resting chondrocytes towards the hypertrophic state. This, in turn, could disrupt the normal function of the growth plate and bone elongation after sustained GPI.

Bone repair relies on adequate angiogenesis and its primary pro-angiogenic stimulator, Vegf. We observed a steep increase in Vegfa gene expression from 0 to 1 DIV in both control and injured OTCs. However, at 3 DIV, the injured OTCs had reduced their Vegfa expression by half, while the control OTCs exhibited this rapid decrease only at 7 DIV. Notably, while bone growth and repair depend on sufficient angiogenesis and vascular supply, it has been demonstrated that elevated Vegf levels correlate with the formation of a bony bar. Therefore, high Vegf levels can serve as an indicator of the bone bridge development process [179–181]. Interestingly, Erickson et al. provided evidence that the application of a particular hydrogel containing an anti-Vegf antibody effectively suppressed the formation of a bone bridge following tibial physeal injury, without disrupting the regular bone elongation process [182]. Moreover, Chung et al. reported that GPI treatment with anti-Vegf significantly decreased blood-vessel-like structures within the injury site together with decreased bony tissue at the injury site at day 14 in a rat tibial drill hole model [181].

4.7 Osteoclastogenesis

The development of a bone bridge involves the both, cartilage and bone formation as well as osteoclastic remodelling of the newly formed trabecular bone at the injury site [83, 151]. Osteoclastogenesis is initiated when RankL binds to its receptor Rank, while the binding of Opg to the receptor results in the suppression of osteoclast formation [183]. In our study, we noted an upregulation in gene expression of osteoclastogenesis inhibition marker Opg within our OTCs during the cultivation period. It seems that the GPI has a limiting effect the first 7 DIV. Furthermore, both osteoclastogenesis activators RankL and its receptor, Rank, exhibited consistent downregulation at all time points in both injured and control OTCs. Additionally, there was a noticeable reduction in both the quantity and activity of osteoclasts in both the GPI and control OTCs throughout the cultivation period. These findings align with the observations of Pichler et al., who similarly reported a significant upregulation of Opg expression at the site of injury, indicative of chondrogenesis inhibition due to GPI in their drill hole model [184]. We further observed two distinct areas of osteoclast activity: in the proximal and distal metaphysis. New research suggest that osteoclast are a heterogenous population capable of digesting various matrices, including bone, cartilage and dentine [185, 186]. Furthermore, the existence of a specific cartilage-resorbing osteoclast type, named the chondroclast, is still under debate [187]. In their study, Romeo et al. discovered two distinct osteoclast subtypes in the metaphysis, namely vessel-associated osteoclasts (VAOs, proximal) and bone-associated osteoclasts (BAOs, distal). BAOs are normal osteoclast, while VAOs, on the contrary, are responsible for cartilage degeneration in the postnatal GP to make space for invading blood vessels. Moreover, the VAOs type weas prevalent in growing bone, while the BAOs type was the primary osteoclast found in aging bone. They also demonstrated a significant decrease in the number of osteoclast over time, which correlates with the ageing of the mice. [187].

4.8 Limitations of the methodology

We were able to establish a robust methodology to advance the research on physiological and pathological processes following GPI. However, there exist certain limitations of this methodology which need to be taken under consideration for further utilizations. As our OTCs are cultured ex vivo the lack of vascularization, blood flow and therefor the absence of systemic factors as well as limited inflammatory/immune cells need to be considered while interpreting the data. GPI follows four distinct phases which include the inflammatory phase (days 1 - 3), fibrogenic phase (days 3 - 7), osteogenic phase (days 7 - 14) and remodelling phase (day 14 +) [86, 139]. The inflammatory phase is characterized by the invasion of inflammatory cells, primarily neutrophils, along with macrophages/monocytes and lymphocytes, which is observed at the injury site. This process is initiated approximately 8 hours after the sustained injury, peaks at 1 day post-injury, and fades by 3 days post-injury [78]. These cells play a crucial role in eliminating debris and secreting cytokines and growth factors, which, in turn, regulate downstream (pathological) regeneration processes [76]. Therefore, they recruit stem cells and progenitor cells to the injury site, demonstrating the long-lasting effects that immune cells have on the regeneration of GPI [188]. The importance of the inflammatory response was highlighted by Chung et al. They treated a GPI with a neutrophil-neutralizing antiserum and observed and increase of osteogenic markers coupled with a decrease of chondrogenic markers [78]. Interestingly, even though our model lacks the systemic inflammatory phase, we observed the opposite of what Chung et al. reported. Our model exhibited an increase in chondrogenic markers along with a decrease in osteogenic markers. Furthermore it has been reported that TNF-α, secreted by the infiltrated immune cells, has a critical role in recruiting stem cell towards the injury site [77, 189]. Similar to our contrasting findings compared to Chung et al., we observed potential migration of what appeared to be stem cells or precursor cells from the groove of Ranvier towards the injury site in the Live/Dead staining. Furthermore, the presence of stem cells within the injury site was confirmed through STEM imaging.

Another limitation of our study is the challenging quantification of the injury dimension and its regeneration over the cultivation period. Although we used a 2 mm razor blade to mimic the GPI, with the later secondary ossification point serving as the starting point, we observed variability in the initial GPI dimension due to handling. Furthermore, daily measurements of the GPI dimensions within the same OTC were not feasible. Therefore, this study lacks numerical quantification of the in vitro regeneration process.

Methodologically challenging and difficult in the interpretation and quantification was also the variability in histological and IHC staining's between the independent experiments. Although some animals demonstrated a different staining pattern, most of the data gained from the independent experiments did demonstrate a trend. Although a robust image quantification process was developed, due to the endochondral ossification process of the OTC during the in vitro cultivation as well as difference in initial weight and size of the rat pups and therefor the femur, no good normalization angel was determined. Therefore, the whole epiphysis was used in the image quantification process. Unfortunately, clearly observed differences within the distinct zones between control and injured OTC were lost due to this approach and the (semi)quantitative data is not comparable to the visual observations. To overcome this problem in the future, more sophisticated methodology, e.g. spatial biology, would be a good alternative.

4.9 Conclusion and Outlook

To summarize, we have successfully modified an ex vivo femur bone model to study the regeneration process following GPI. The gene expression data, along with the observed formation of a network in the live/dead staining as well as the IHC data, may indicate the recruitment of MSCs into the injury lesion. This recruitment could be followed by the stimulation of MSCs toward the chondrogenic lineage through Ihh and Sox9. Simultaneously, it may involve the preservation of the proliferation of chondrocyte columns, promotion of their transition into hypertrophic cells, and inhibition of their transdifferentiation. Furthermore, we observed evidence of premature mineralization of the GP, as indicated by decreased Col2a1 positive staining coupled with increased Osx positive staining following the GPI. These processes were also evident in the Movat-Pentachrome, where we observed earlier tissue mineralisation in the injured OTCs.

The confirmation of the similarities between ex vivo organ cultures and their in vivo counterparts has unlocked significant opportunities in scientific research. Particularly given the challenge of translating in vitro cell culture data to in vivo conditions, ex vivo cultures play a vital role in bridging this crucial gap between the two settings. Moreover, we are committed to upholding the "3Rs" principle, which promotes the reduction, refinement, and replacement of animal experiments in scientific research. Ex vivo organ cultures present the possibility of harnessing one animal for multiple research hypotheses. Our ongoing efforts are focused on refining this technology to obtain multiple bone slice cultures from a single bone, extending their viability in the in vitro setting, and expanding to different types of bones, thus making the most efficient use of one animal and actively reducing the number of animals required for scientific research.

As our lifespans continue to lengthen, research in the realm of skeletal health and postnatal bone development becomes increasingly urgent. Methodologies like the ex vivo femur culture serve as powerful tools for investigating physiological and pathophysiological processes related to development, regeneration, and disease. They further contribute to fields such as tissue engineering and material/drug testing.

Furthermore, the established GPI ex vivo culture will be instrumental in our approved UFO grant from the Steiermärkischen Landesregierung, where we will explore the potential of stem cell sheets in the regeneration of a sustained growth plate injury (GPI). The project with the titel: “Ein Stammzellpflaster als Therapiemöglichkeit für Verletzungen der juvenilen Wachstumsfuge“ is funded with a volume of € 99.998,79.

Part Two

5 Results Part Two

5.1 Morphological and tissue composition changes following particle irradiation

To investigate the underlying effect of particle IR (proton and C-ions) on postnatal endochondral ossification within a 1-day old ex vivo bone cultures were morphologically analyzed at 1 and 14 DIV following radiation, using H&E, Movat-Pentachrome, Safranin O-Fast Green (Fig. 36a-c). Differences between proton IR, C-ions IR and control (Non-IR) OTCs within the distinct zones: TZ (yellow square), MZ (red square), and DZ (blue square) are discussed in more detail in the following.

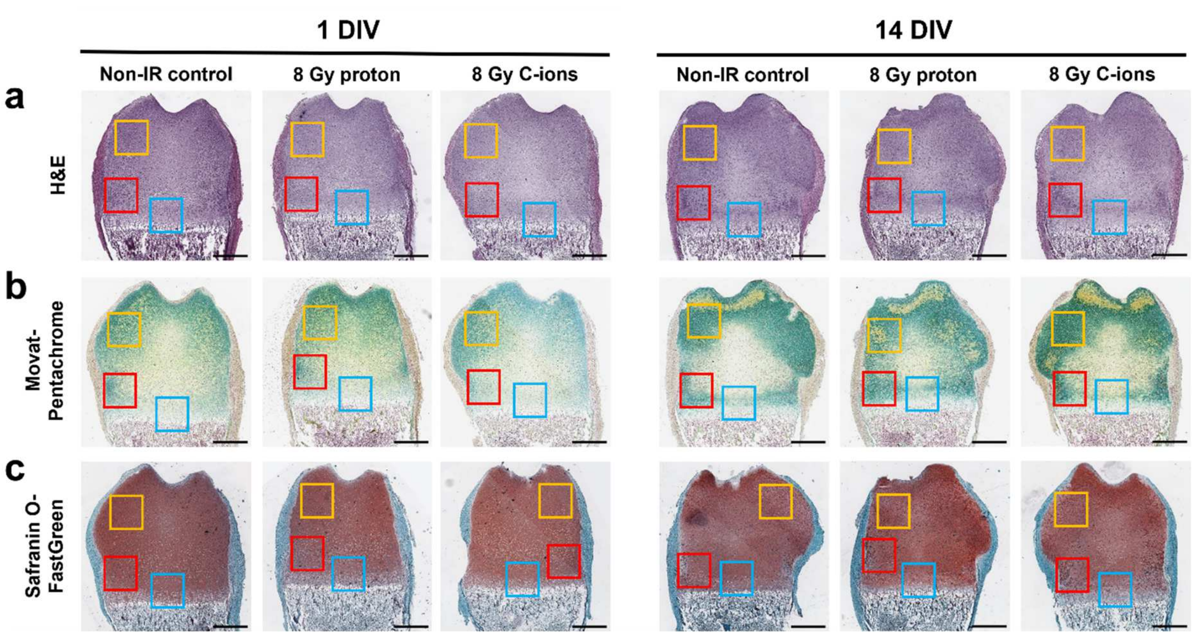

Figure 36. Representative images of ex vivo bone cultures (OTC) following proton or carbon ions (C-ions) irradiation and respective control (Non-IR) that underwent histological staining using various techniques. Representative images of the one day old proximal femur OTC after particle irradiation (IR) with either 8 Gy proton or 8 Gy carbon ions (c-ions) with the non irradiadiated control (Non-IR) at 1 and 14 days of in vitro cultivation (DIV) stained with **a)** Hematoxylin and Eosin stain (H&E), **b)** Movat-Pentachrome, and **c)** Sarfanin O-Fast Green stain. The colored squares indicate transition zone (TZ, yellow square), middle zone (MZ, red square), and deep zone (DZ, blue square) for following detailed investigation. Scale bar: 500 µm. Reproduced from [2] under the terms of CC BY.

5.2 Morphological changes within the distinct zones following particle irradiation

To evaluate the morphological alterations following particle IR in the OTC we performed H&E staining (Fig. 37).

One day after exposure to 8 Gy proton IR, we observed the presence of pre-hypertrophic chondrocytes randomly scattered within the TZ, which were absent in the Non-IR control OTC. Within the C-ions IR OTC, these pre-hypertrophic chondrocytes were also absent. Within the MZ zone of both proton and C-ions IR-exposed OTCs, a profound reduction in actively dividing chondrocytes was evident when compared to the Non-IR control OTC. Moreover, these cells were replaced by pre-hypertrophic chondrocytes. Furthermore, the chondrocytes located in the DZ remained unaffected at 1 DIV.

At 14 DIV the impact of particle irradiation became most pronounced within the MZ. Specifically, OTCs exposed to 8 Gy proton IR displayed a transformation of chondrocytes into the (pre)-hypertrophic states, and these cells organized into columnar structures, typically characteristic of the DZ and essential for the process of bone elongation. Conversely, following C-ions IR, chondrocytes exhibited an overall increase in size, formed isogenic groups, but concurrently transitioned into pre-hypertrophic state within these clusters.

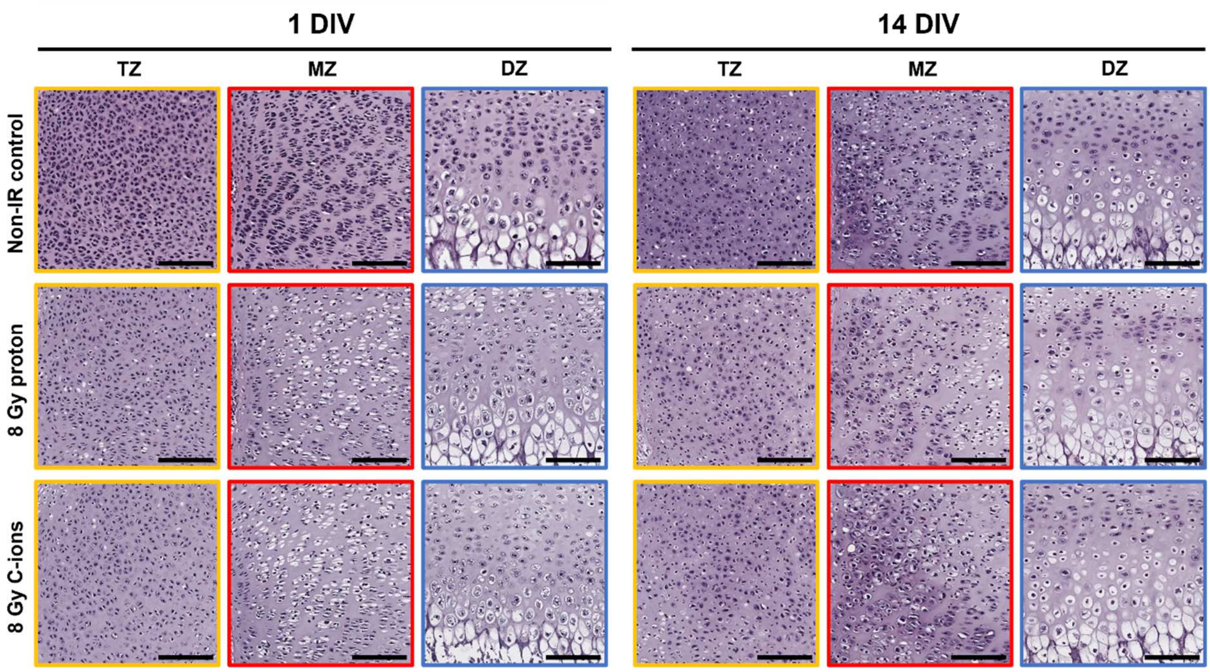

Figure 37. Particle irradiation has a profound effect on postnatal growth plate (GP) maturation. Representative images represent one day old ex vivo bone cultures (OTC) after particle irradiation (IR) with either 8 Gy proton or 8 Gy Carbon ions (C-ions), along with the non-irradiated control (Non-IR control) and subsequent 1 or 14 days in vitro cultivation (DIV) stained with Haematoxylin and Eosin (H&E) staining. Coloured squares indicate transition zone (TZ, yellow square), middle zone (MZ, red square), and deep zone (DZ, blue square). Scale bar: 150 µm. Reproduced from [2] under the terms of CC BY.

5.3 Tissue maturation disruption due to particle irradiation

Movat-Pentachrome staining was performed to investigate the progression of endochondral ossification following exposure to particle IR and subsequent in vitro cultivation (Fig. 38).

Notably, no substantial differences were observed after 1 DIV between proton IR, C-ions IR and Non-IR control OTCs. The only notable change observed was a diminished staining intensity of both cartilage and mineralized tissue within the MZ following C-ions IR compared to the proton IR and Non-IR control OTC.

14 days after particle irradiation exposure, distinct patterns emerged within the OTCs. Proton IR exposed OTCs exhibited the presence of mineralized tissue (bright yellow staining) primarily in the TZ as compared to the Non-IR control. In contrast, cartilage became the predominant tissue within the C-ions IR OTCs (green staining). Notably, in both IR OTCs, there was an increased in mineralization of cells (bright yellow) adjacent to the zone of Ranvier in the MZ.

Furthermore, proton IR induced a more intense cartilage staining (green staining) within the DZ, whereas C-ions IR led to a reduction in cartilage staining.

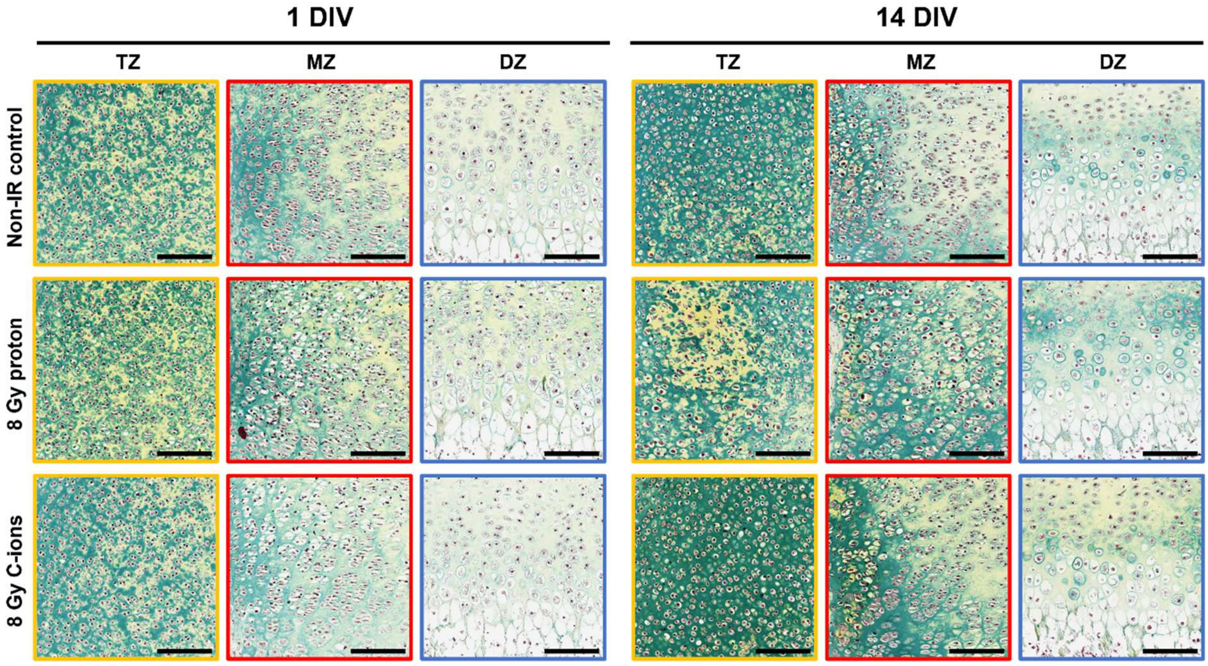

Figure 38. Particle irradiation leads to accelerated postnatal growth plate (GP) mineralization. Representative images represent one day old ex vivo bone cultures (OTC) after particle irradiation (IR) with either 8 Gy proton or 8 Gy Carbon ions (C-ions), along with the non-irradiated control (Non-IR control) and subsequent 1 or 14 days in vitro cultivation (DIV) stained with Movat-Pentachrome staining. Coloured squares indicate transition zone (TZ, yellow square), middle zone (MZ, red square), and deep zone (DZ, blue square). This staining results in structures being stained as follows: cell nuclei (black), cytoplasm (reddish), elastic fibers (red), collagen connective tissue (light yellow), mineralized tissue/bone (dark yellow, black arrows) and mineralized cartilage (dark green-blue, black stars). Scale bar: 150 µm. Reproduced from [2] under the terms of CC BY.

5.4 Proteoglycan secretion is enhanced due to particle irradiation

To investigate the impact of particle IR on the secretion of ECM protein PG, we conducted Safranin O-Fast green staining, which indicates the presence of PG in the tissue (Fig. 39).

One day after the in vitro cultivation following exposure to particle irradiation, we did not observe any discernible differences in the distribution of proteoglycans (PG) within the OTC.

However, after 14 DIV post IR, we noted profound differences in PG production and secretion compared to the Non-IR control OTC. Specifically, there was a notable and substantial increase in PG content within the territorial matrix of chondrocytes located in both the MZ and DZ following both proton and C-ions IR when compared to the Non-IR control OTCs. Notably, these increased PG areas are similar to the prematurely mineralized areas observed within the Movat-Pentachrome staining.

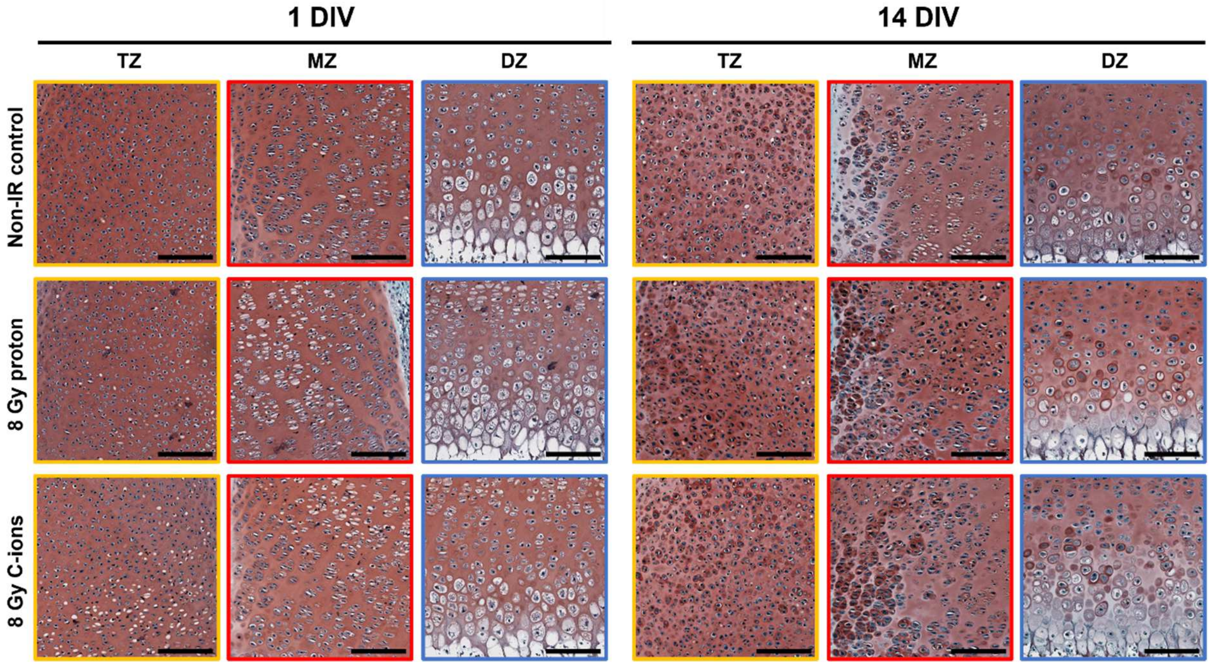

Figure 39. Particle irradiation enhanced proteoglycan (PG) production and secretion in the postnatal growth plate (GP). Representative images represent one day old ex vivo bone cultures (OTC) after particle irradiation (IR) with either 8 Gy proton or 8 Gy Carbon ions (C-ions), along with the non-irradiated control (Non-IR control) and subsequent 1 or 14 days in vitro cultivation (DIV) stained with Safranin O-Fast Green staining. Coloured squares indicate transition zone (TZ, yellow square), middle zone (MZ, red square), and deep zone (DZ, blue square). Scale bar: 150 µm. Reproduced from [2] under the terms of CC BY.

5.5 ECM maturation is changed due to particle irradiation

Because of the observed variations in tissue composition in Movat-Pentachrome and Safranin O-Fast Green staining following particle IR, we chose to focus on the collagen component of the ECM next. Therefore, we analyzed the gene expression as well as the distribution of Col2a1 as an indicator for proliferating and pre-hypertrophic chondrocytes and Col10a1 as an indicator of chondrocyte hypertrophy. Representative control images can be found in Fig. 46a.

Regarding the spatial distribution of Col2a1 expression, we initially observed only moderate staining in the columnar zone of the growth plate (DZ) and towards the later secondary ossification center at 1 DIV (Fig. 40a). However, as the cultivation period progressed, there was a substantial increase in Col2α1 staining. By 14 DIV, Col2a1 had expanded from the center of the epiphysis toward both the MZ and the DZ. Notably, Non-IR control OTCs exhibited the highest positive staining area, followed by those subjected to C-ions IR and proton IR. This observation was further supported by our gene expression analysis. In all experimental conditions, a highly significant upregulation of Col2a1 expression was evident between 1 DIV and 14 DIV (Non-IR: 5.82 ± 4.3***; proton: 5.33 ± 3.0***; C-ions: 2.92 ± 1.3***). Notably, at 14 DIV, C-ions IR had a significant impact on Col2a1 expression when compared to the Non-IR controls (**) (Fig. 40c).

Chondrocyte hypertrophy is marked due to the presence of Col10a1 in the ECM. At 1 DIV, moderate Col10 positive staining of the inter-territorial matrix of hypertrophic chondrocytes within the DZ was observed in both Non-IR control and proton IR OTCs (Fig. 40b). Notably, the height of the hypertrophic area appeared reduced after proton IR (black bracket). In OTCs subjected to C-ions IR, Col10 was primarily confined within the chondrocytes and had not yet been secreted into the ECM at 1 DIV. However, at 14 DIV, a significant increase in Col10 staining intensity was observed in all conditions. In the Non-IR control, a uniform and sufficient hypertrophic zone was observed, whereas this area was reduced following particle irradiation. Notably, at sites of calcification, the proton and C-ions IR OTCs exhibited intensely positive Col10 staining, which was absent in the Non-IR OTCs. Additionally, our gene expression data indicated a decrease in Col10 expression due to particle irradiation at 1 DIV, with a highly significant reduction in gene expression from 1 DIV to 14 DIV in all conditions, respectively (Non-IR: 0.14 ± 0.1***; proton: 0.04 ± 0.1***; C-ions: 0.01 ± 0.01***). At 14 DIV, a significant difference was observed between non-IR control and proton IR (*) and C-ions IR (**) (Fig. 40d).

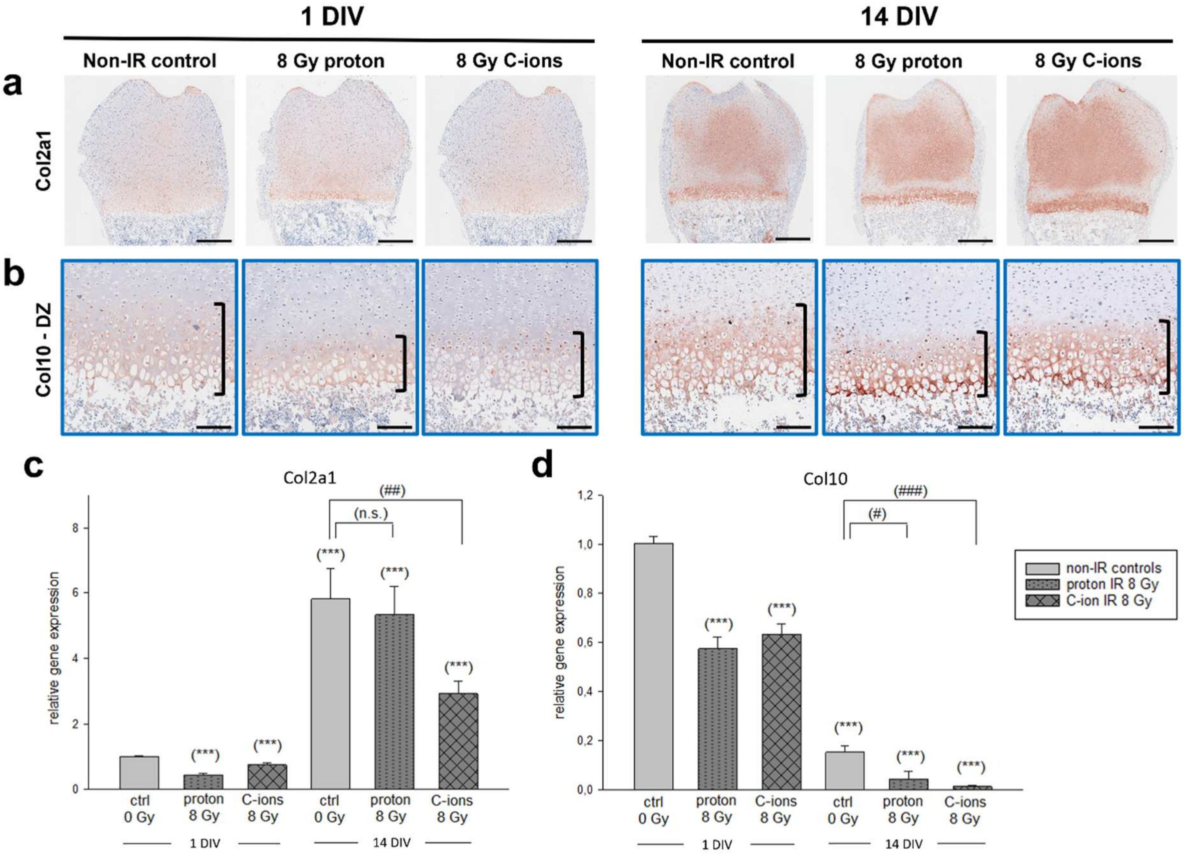

Figure 40. Particle irradiation altered extracellular matrix (ECM) composition during the postnatal growth plate (GP) development. a-b) ECM composition was analysed in the one day old ex vivo bone culture (OTC) by immunohistochemistry (IHC) staining of type II collagen (Col2a1, proximal epiphysis) and type X collagen (ColX, deep zone (DZ) – blue square) at 1 and 14 days of in vitro cultivation (DIV) following particle irradiation (IR) with either 8 Gy proton or 8 Gy carbon (C-ions) with the respective non-irradiated (Non-IR) control. Black bracket – hypertrophic zone. Red – positive staining. Scale bar: 500 µm (Col2a1), 150 µm (ColX). **c-d)** Gene expression analysis of Col2a1 and ColX by real time PCR (RT-PCR). Statistical significance of observed differences was assessed using the Whitney-U Test for injury vs. control comparisons or Kruskal-Wallis-H test with Bonferroni correction was applied for multiple comparisons. Data are presented as mean ± SEM, with a minimum of n ≥ 4 animals per time point and 3 technical replicates. Significant differences at 1 DIV: $P \leq 0.05$(*), $P \leq 0.01$(**), and $P \leq 0.001$(***), and at 14 DIV: $P \leq 0.05$(#), $P \leq 0.01$(##), and $P \leq 0.001$(###). (n.s.) = not significant differences. Relative gene expression – gene expression normalized to 0 DIV control, which is set to 1. Reproduced from [2] under the terms of CC BY.

5.6 Progression of endochondral ossification following particle irradiation

Next, regeneration processes especially chondrocyte differentiation after exposure to particle IR were examined. Therefore, we analyzed the gene expression as well as the protein distribution of Bmp-2, Runx2 and OPG in the postnatal GP. In the proximal epiphysis, variations in the distribution pattern of these markers were evident and will be discussed in greater detail in the subsequent result sections (Fig. 41a-c). Representative control images can be found in Fig. 46a.

Gene expression studies revealed significant upregulation following proton IR (4.76 ± 4.9*) but a significant downregulation after C-ion IR (0.74 ± 0.3**) at 1 DIV (Fig. 41d). Subsequently, in all experimental conditions, a notable upregulation in Bmp-2 expression was observed after 14 DIV (Non-IR: 9.98 ± 4.2***; proton: 6.33 ± 3.8***; C-ions: 2.75 ± 2.3*). However, proton IR (*) and C-ions IR (**) had a significantly limiting effect on the upregulation at 14 DIV.

Concerning Runx2 gene expression, particle IR led to a highly significant downregulation of the expression at 1 DIV when compared to the Non-IR control (proton: 0.65 ± 0.3***; C-ions: 0.64 ± 0.3***) (Fig. 41e). After 14 DIV, gene expression was upregulated across all conditions (Non-IR: 4.69 ± 5.9**; proton: 1.76 ± 1.6; C-ions: 1.04 ± 0.5). Similar to Bmp-2, the upregulation of Runx2 gene expression was significantly reduced due to proton IR (*) and C-ions IR (**) at 14 DIV, compared to the respective Non-IR control.

Opg gene expression was not affected by particle IR at one day (1 DIV) (Fig. 41f). At 14 DIV, a significant upregulation was observed for OPG gene expression in all conditions (Non-IR: 8.21 ± 6.0***; proton: 9.84 ± 3.4***; C-ions: 5.41 ± 1.65***). Notably, C-ions IR (*) resulted in a significant reduction in OPG gene expression, when compared to the respective Non-IR control.

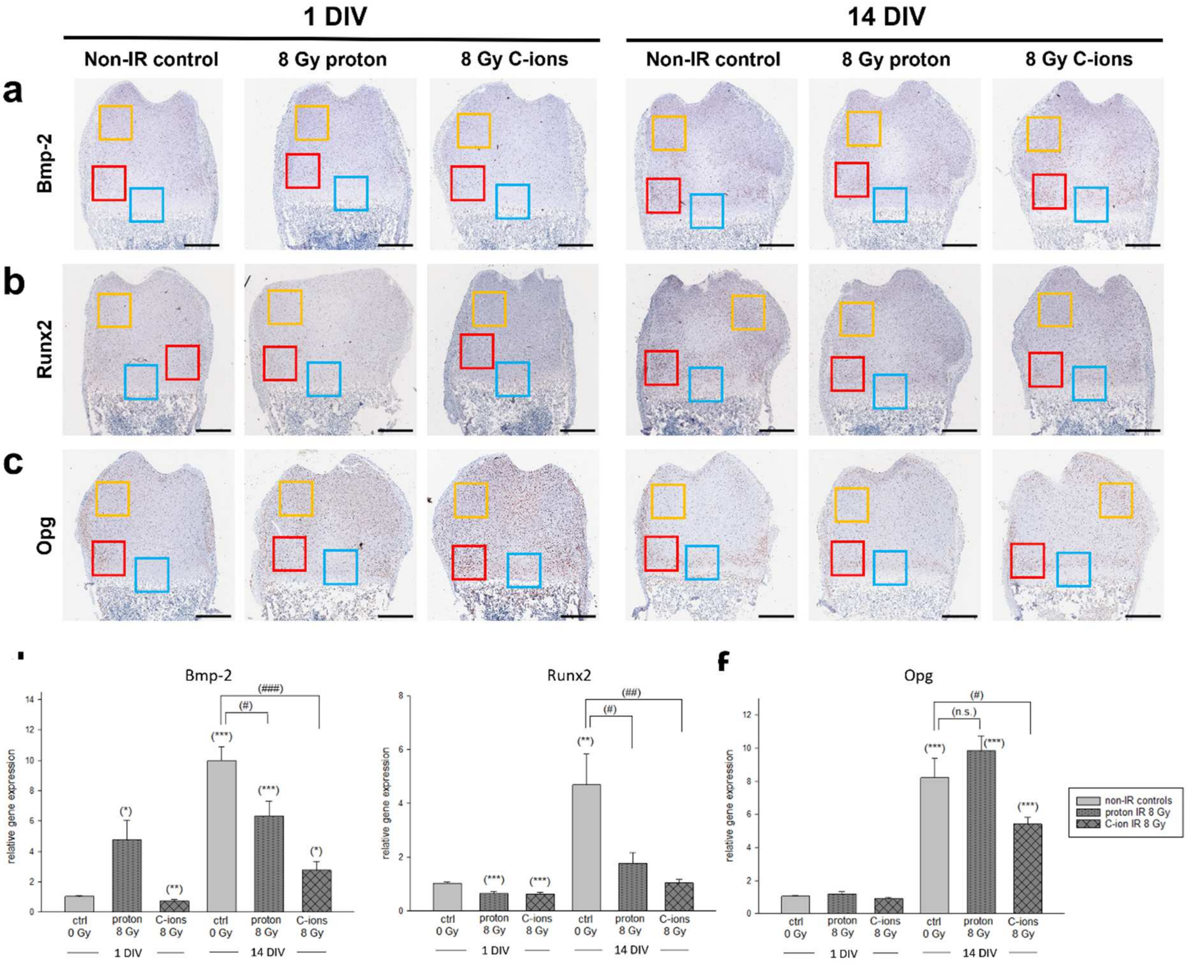

Figure 41. Particle irradiation influenced chondrogenesis in postnatal growth plate (GP). a-c) Representative images represent the proximal epiphysis of one day old ex vivo bone cultures (OTC) after particle irradiation (IR) with either 8 Gy proton or 8 Gy Carbon ions (C-ions), along with the non-irradiated control (Non-IR control) and subsequent 1 or 14 days in vitro (DIV) cultivation stained by immunohistochemistry (IHC) of bone morphogenetic protein 2 (Bmp-2), Runt-related transcription factor 2 (Runx2) and osteopotegerin (Opg). Coloured squares indicate transition zone (TZ, yellow square), middle zone (MZ, red square), and deep zone (DZ, blue square). Red – positive staining. Scale bar: 500 µm. **d-f)** Gene expression analysis of Bmp-2, Runx2 and Opg by real time PCR (RT-PCR). Statistical significance of observed differences was assessed using the Whitney-U Test for injury vs. control comparisons or Kruskal-Wallis-H test with Bonferroni correction was applied for multiple comparisons. Data are presented as mean ± SEM with a minimum of n ≥ 4 animals per time point and 3 technical replicates. Significant differences at 1 DIV: P ≤ 0.05(*), P ≤ 0.01(**), and P ≤ 0.001(***), and at 14 DIV: P ≤ 0.05(#), P ≤ 0.01(##), and P ≤ 0.001(###). (n.s.) = not

significant differences. Relative gene expression – gene expression normalized to 0 DIV control, which is set to 1. Reproduced from [2] under the terms of CC BY.

Regarding the Bmp-2 distribution, a well-known factor that induces chondrogenesis and promotes endochondral ossification, only faint positive staining was evident within the TZ, MZ, and DZ for all experimental conditions (Fig. 42). Notably, this was particularly visible after C-ions IR, which resulted in a reduced presence of positive staining within these regions. At 14 DIV, chondrocytes exhibited a more intense Bmp-2 staining across all conditions. However, within the TZ, a reduction in positive staining was observed specifically due to C-ions IR. Moreover, a decrease in positive chondrocyte staining was noted within both the MZ for both proton and C-ions IR, respectively.

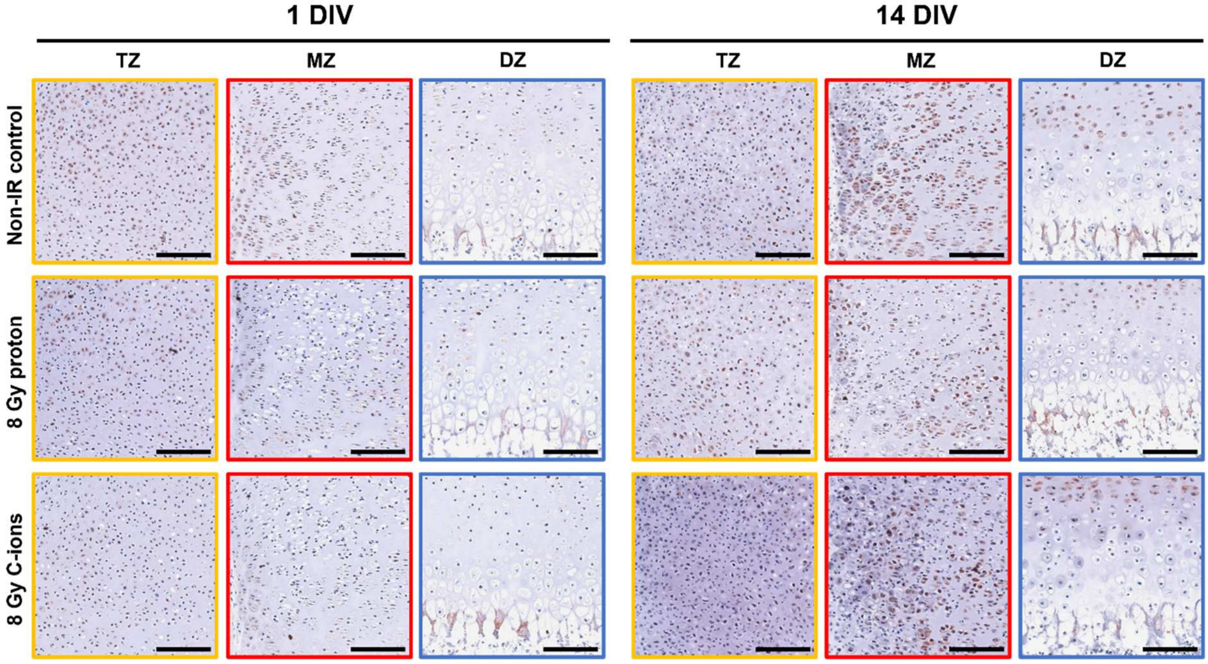

Figure 42. Master regulator Bone morphogenic protein 2 (Bmp-2) stimulates either chondrogenesis or osteogenesis in postnatal growth plate (GP). Representative images of the proximal epiphysis of one day old ex vivo bone cultures (OTC) after particle irradiation (IR) with either 8 Gy proton or 8 Gy Carbon ions (C-ions), along with the non-irradiated control (Non-IR control) and subsequent 1 or 14 days in vitro (DIV) cultivation stained by immunohistochemistry (IHC) of Bmp-2. The coloured squares represent the distinct zone: transition zone (TZ, yellow square), middle zone (MZ, red square) and deep zone (DZ, blue square). Red – positive staining. Scale bar: 150 µm. Reproduced from [2] under the terms of CC BY.

Next, we studied Runx2, a crucial transcription factor responsible for promoting terminal hypertrophy of chondrocytes in the postnatal GP. At 1 DIV, a reduction in positive staining of chondrocytes within the TZ and MZ was evident due to the exposure to particle IR (Fig. 43). In the DZ, proton IR had no noticeable effects on the positive staining of chondrocytes, while an increase in Runx2-positive chondrocyte staining was observed after C-ions IR. After 14 DIV, a decrease in staining following proton and C-ions IR was observed within the TZ and MZ. In the DZ, neither proton nor C-ions IR had an effect on Runx2 expression.

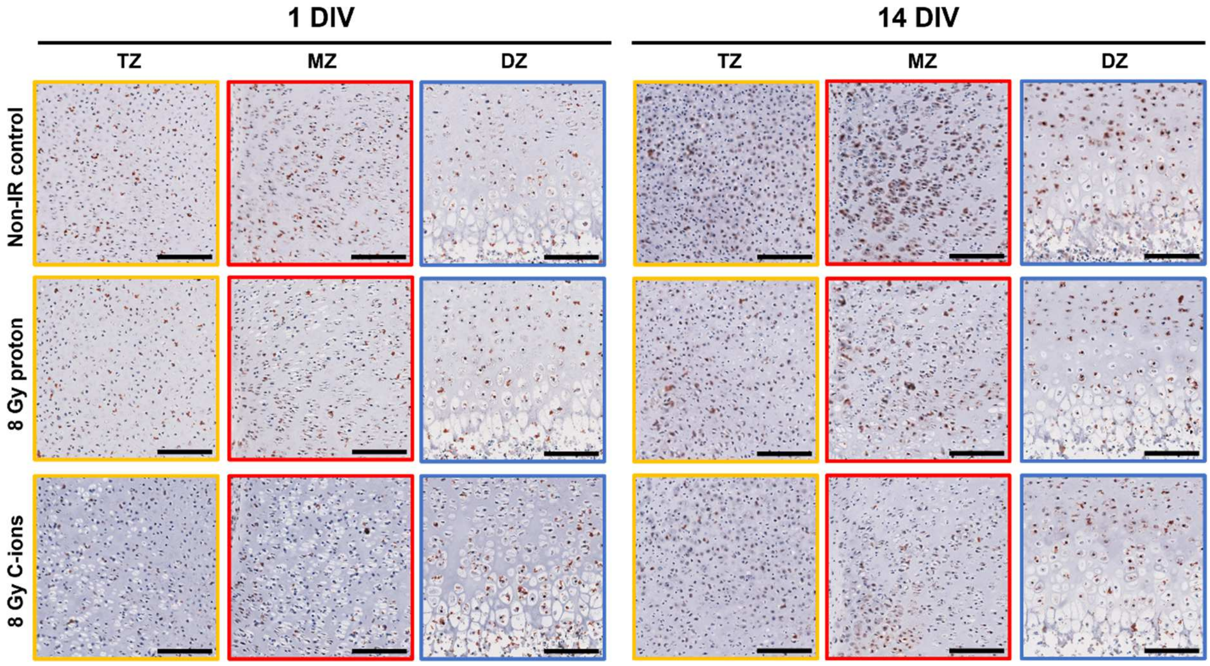

Figure 43. Terminal hypertrophic runt-related transcription factor 2 (Runx2) decreased due to particle irradiation in postnatal growth plate (GP). Representative images of the proximal epiphysis of one day old ex vivo bone cultures (OTC) after particle irradiation (IR) with either 8 Gy proton or 8 Gy Carbon ions (C-ions), along with the non-irradiated control (Non-IR control) and subsequent 1 or 14 days in vitro (DIV) cultivation stained by immunohistochemistry (IHC) of Runx2. The coloured squares represent the distinct zone: transition zone (TZ, yellow square), middle zone (MZ, red square) and deep zone (DZ, blue square). Red – positive staining. Scale bar = 150 µm. Reproduced from [2] under the terms of CC BY.

At 1 DIV, positive Opg stained chondrocytes were observed in the TZ and MZ of the Non-IR control OTCs (Fig. 44). However, following particle IR these positively stained chondrocytes were distributed throughout the entire proximal epiphysis, including the TZ, MZ, and DZ coupled with higher staining intensity. After 14 DIV a reduction in Opg staining was observed within the TZ, MZ and DZ of proton IR OTCs compared to the Non-IR control. On the contrary, Opg positive staining increased at this time point after C-ions IR.

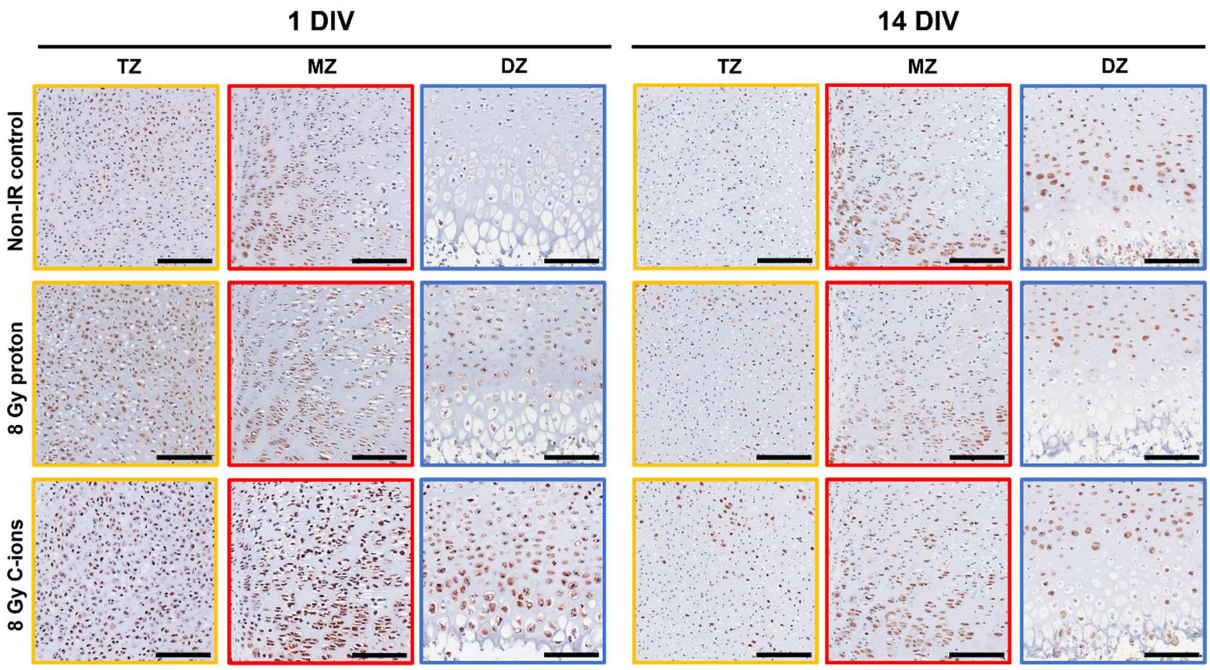

Figure 44. Osteopotegerin (Opg) decreased or increased following particle irradiation in the postnatal growth plate (GP). Representative images of the proximal epiphysis of one day old ex vivo bone cultures (OTC) after particle irradiation (IR) with either 8 Gy proton or 8 Gy Carbon ions (C-ions), along with the non-irradiated control (Non-IR control) and subsequent 1 or 14 days in vitro (DIV) cultivation stained by immunohistochemistry (IHC) of Opg. The coloured squares represent the distinct zone: transition zone (TZ, yellow square), middle zone (MZ, red square) and deep zone (DZ, blue square). Red – positive staining. Scale bar: 150 µm. Reproduced from [2] under the terms of CC BY.

5.7 Influences of particle irradiation on osteogenesis

Finally, we investigated the effect of particle IR on osteogenesis during postnatal GP development. Therefore, we performed gene expression analysis together with IHC of key osteogenesis marker Opn and Alpl.

At 1 DIV, faint positive Opn staining along the perichondrium in the Non-IR control as well as after C-ions IR was observed, while this was more pronounced after proton IR (Fig. 45a). By

14 DIV the perichondrium displayed intense positive staining across all groups. Notably, we also noted positive Opn staining in the calcification zone of the Non-IR control OTC which was missing in the particle irradiated OTCs. Gene expression levels further revealed a highly significant reduction in Opn due to proton IR at 1 DIV (0.61 ± 0.3***) (Fig. 45b). Over the 14 DIV period, there was a substantial upregulation in Opn expression for all groups (Non-IR: 11.66 ± 8.8***; proton: 14.81 ± 6.2***; C-ions: 10.5 ± 7.2***). However, no significant differences due to particle irradiation were detected. Representative control images can be found in Fig. 46a.

Concerning Alpl gene expression, both proton and C-ions IR led to a highly significant downregulation, when compared to the respective Non-IR control (proton: 0.57 ± 0.3***; C-ions: 0.69 ± 0.2***) (Fig. 45c). As osteogenesis progressed, Alpl expression significantly increased over the 14-day cultivation period for the Non-IR control (2.62 ± 1.2***), while particle irradiation had a limiting effect (proton: 1.28 ± 0.7; C-ions: 1.40 ± 1.1). When compared to the respective Non-IR control this Alpl gene expression reduction was highly significant (proton***, C-ions**).

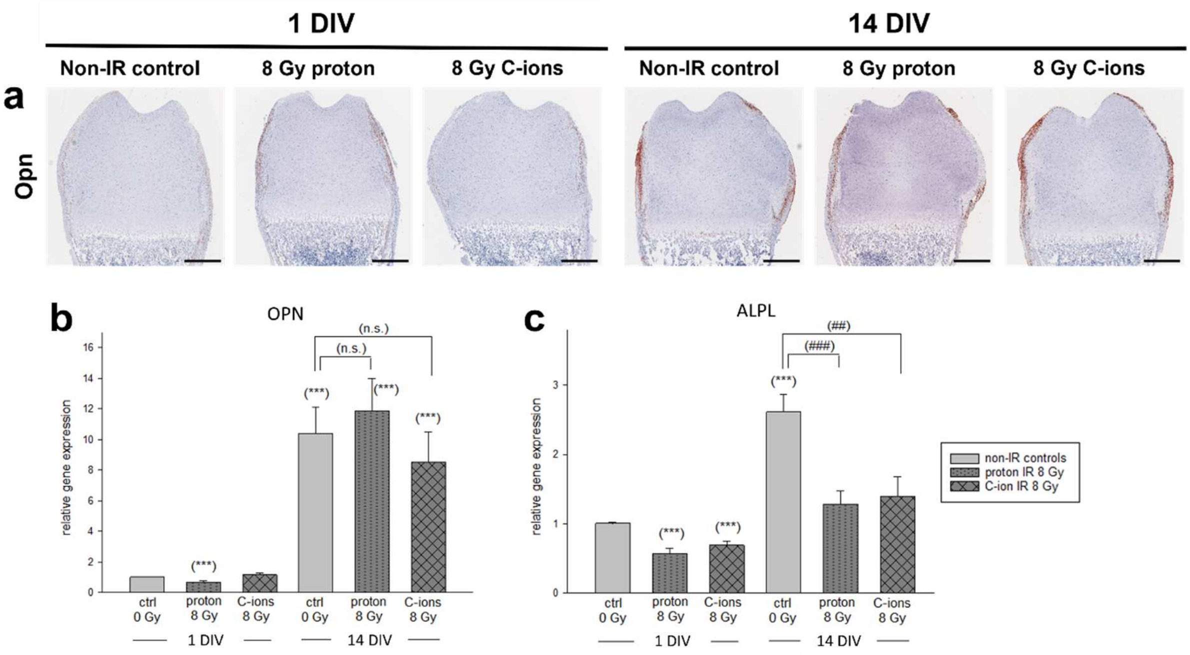

Figure 45. Ion radiation influences osteogenesis in postnatal growth plate (GP). a-c) Representative images represent the proximal epiphysis of one day old ex vivo bone cultures (OTC) after particle irradiation (IR) with either 8 Gy proton or 8 Gy Carbon ions (C-ions), along with the non-irradiated control (Non-IR control) and subsequent 1 or 14 days in vitro cultivation (OTC) stained by immunohistochemistry (IHC) osteopontin (Opn). Scale bar: 500 µm. **d-f)**

Gene expression analysis of Osteopontin (Opn) and alkaline phosphatase (Alpl) by real time PCR (RT-PCR). Statistical significance of observed differences was assessed using the Whitney-U Test for injury vs. control comparisons or Kruskal-Wallis-H test with Bonferroni correction was applied for multiple comparisons. Data are presented as mean ± SEM with a minimum of $n \geq 4$ animals per time point and 3 technical replicates. Significant differences at 1 DIV: $P \leq 0.05$(*), $P \leq 0.01$(**), and $P \leq 0.001$(***), and at 14 DIV: $P \leq 0.05$(#), $P \leq 0.01$(##), and $P \leq 0.001$(###). (n.s.) = not significant differences. Relative gene expression – gene expression normalized to 0 DIV control, which is set to 1. Reproduced from [2] under the terms of CC BY.

Finally, representative images of stainings control for Live/Dead staining (Fig. 42b) and IHC of the target markers: Acan, Col2a1, Col10a1, Bmp-2, Runx2, Osx, Sox9, Opn, Vimentin, Ki67 and c-Cas 3 are presented (Fig. 46a).

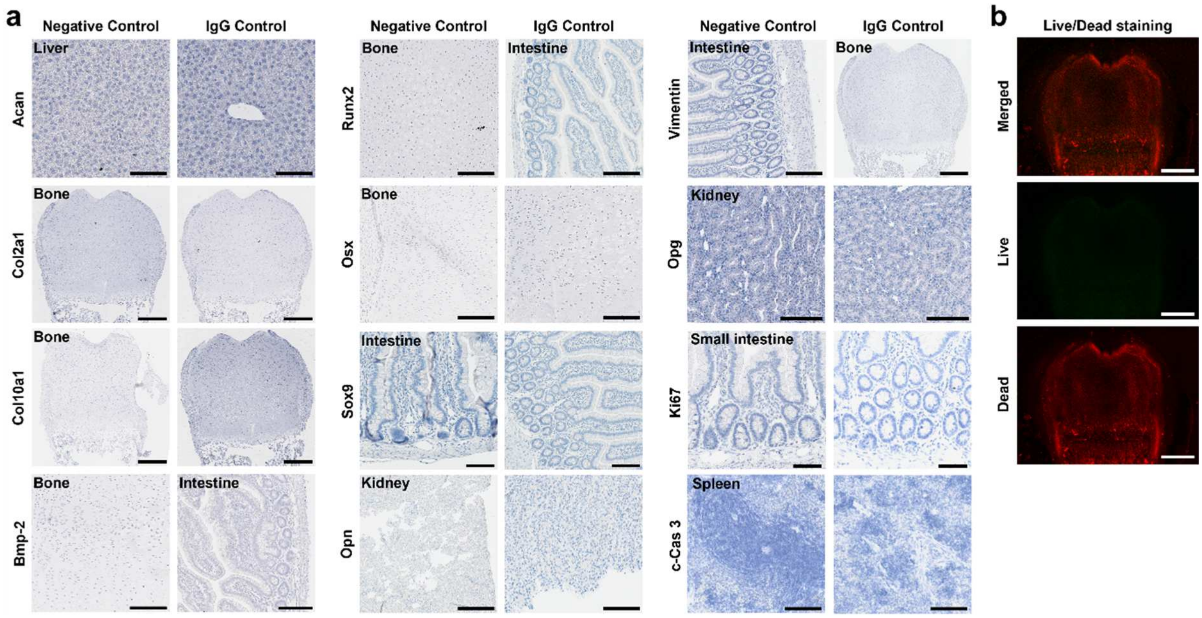

Figure 46 Representative Images of controls for immunohistochemistry staining (IHC) and live/dead staining. a) IHC controls represent a negative control, which does not have a primary antibody, and an IgG control, which was incubated either with anti-mouse or anti-rabbit IgG depending on the origin of the primary antibody. The targets include: Acan, Col2a1, Col10a1, Bmp-2, Runx2, Osx, Sox9, Opn, Vimentin, Ki67 and c-Cas 3. Scale bar: 500 µm (Bone - epihpysis), 150 µm (Tissue – close ups). **b)** Live/dead staining controls represent a OTC treated with a 1:1 mixture of DMSO and 70 % EtOH for 1 h.

6 Discussion Part Two

6.1 General Discussion

When it comes to treating malignant tumors, RT is considered one of the gold standard therapeutic approaches. Nevertheless, RT may result in undesired side effects, such as skin redness, hair loss, radiation burns, or acute radiation syndrome [190]. Here, PT offers a combination of precisely targeted high-energy radiation of the tumor while simultaneously protecting the surrounding healthy tissue [138]. Within the confines of the "Bragg peak," accelerated particles loose the bulk of their energy precisely [191]. Notably, while protons deposit their entire energy within the Bragg peak, C-ions experience fragmentation, resulting in the delivery of only a fraction of the dose to distal tissue [192]. Moreover, C-ions possess an elevated RBE, which is attributed to their higher LET and the increased ionization density and track structure of secondary particles generated during interactions post IR [193]. Though particle therapy is more intricate and notably costlier, its benefit in lower undesired side effect and efficiently targeting radioresistant and pediatric tumors have made it the preferred IR method [190].

In clinical practice, particles are administered in the following doses: 70 Gy in 35 fractions at 2 Gy RBE/fraction for proton IR and 70.4 Gy in 16 fractions at 4.4 Gy RBE/fraction for C-ions IR [194, 195]. When it comes to irradiating cells or bones for research purposes, typical doses include 2 Gy, 4 Gy, or 8 Gy for both proton and C-ions IR [193]. Moreover, in clinical settings, when single-fraction radiotherapy is employed usually a dosage of 1 x 8 Gy is applied [196, 197]. To sufficiently demonstrate the consequence induced by proton and C-ions IR on postnatal GP development, a single dose of 8 Gy was administered to one day old ex vivo femur OTCs with subsequent in vitro cultivation.

An essential consideration when caring for pediatric patients belongs to the ongoing process of endochondral ossification and the potential complications arising after IR, which can occur in both RT and PT [198]. While the long-term negative impacts of RT on the GP have been extensively studied [98, 99, 199], little research has been conducted regarding the effects of PT on the GP. This is mainly due to the cost intensive treatment methodology and the restricted accessibility to those infrastructures for basic research.

6.2 Particle irradiation altered the process of endochondral ossification in the postnatal growth plate

It is well-established that RT exerts a multitude of negative effects on bone growth and skeletal development. Post IR complications are similar to the complications observed after GPI. These include growth arrest, growth retardation, fractures, or osteoradionecrosis, which can occur at doses as low as ≥15 Gy. However, the most clinically significant and quantifiable effects are typically observed at doses above 30 Gy [199].

Following a single dose of either 8 Gy proton or C-ions of one day old ex vivo bone cultures a profound decline in the number of actively proliferating chondrocytes within the MZ at 1 DIV was noted. However, at 14 DIV, a noticeable restorative process was observed in the proliferating cells within the MZ of proton-IR OTCs. This process was characterized by the presence of chondrocytic clusters and the substantial production and secretion of ECM/PG production in their territorial and inter-territorial matrix. Moreover, this extensive ECM exhibited increased mineralization which was further noted in the TZ following IR. This observation suggests a potential restorative effort aimed at reinstating functional elongation following the initial loss of proliferative chondrocytes due to proton-IR. Beside the presence of chondrocytic clusters we further noted disruption within the ECM following PT. The hypertrophic chondrocyte marker Col10a1 exhibited a substantial reduction in response to proton-IR, both in the IHC results and the gene expression analysis. In contrast, Col2a1 showed an increase in both the IHC findings and gene expression studies from 1 to 14 DIV, while gene expression was significantly limited following C-ions IR.

Interestingly, Damron et al. [99] conducted an investigation into the impact of a single-dose IR (17.5 Gy X-ray) on the postnatal GP. Initially, a primary inhibitory effect was observed, but subsequent regenerative efforts led to the formation of islands of proliferating chondrocytes. While there was a reduction in the number of cells within the GP, the heightened production and secretion of the ECM resulted in an overall increase in GP height, particularly in the TZ. Furthermore, a subsequent study involving fractionated IR, where a daily dose of 3.5 Gy was administered for five consecutive days, resulting in a total of 17.5 Gy, demonstrated that the reduction in growth rate was not as profound in comparison to the single-fraction experiment. In the single-fraction study, the reduction in growth rate was mainly prominent in the TZ. However, in this fractionated treatment study, with multiple lower Gy doses, the impact extended to the MZ, specifically through the proliferative chondrocytes [100].

The significance of age and radiation dose on the severity of bone growth complications was studied by Hartley et al. [200] and Mizumoto et al. [201]. For bone elongation to occur, chondrocytes must continuously undergo mitotic division to replenish the diminishing pool of hypertrophic chondrocytes. Unfortunately, this heightened mitotic activity leaves the GP particularly susceptible to damage [98, 198]. Marguliese et al. [202] exposed proliferating chondrocytes to serial radiation doses in vitro and observed a dose-dependent adverse effect, marked by reduced proliferation, increased cytotoxicity, apoptosis, and disruption of cell synthetic activity. Horton et al. [98] made similar observations following a single radiation dose of 17.5 Gy X-rays. They concluded that this expanded proliferation along with accelerated ECM synthesis serves as the primary mechanism for reestablishing bone elongation after IR.

6.3 Particle irradiation influenced chondrogenesis and osteogenesis in the postnatal growth plate

Although the Bmp family plays a crucial role in cartilage development and bone growth, Bmp-2 holds particular significance in the ongoing postnatal bone development process [12]. Following PT, we observed an initial reduction in positive Bmp-2 and Runx2 staining at 1 DIV by IHC. However, at 14 DIV, a significant increase in Bmp-2 staining was noted, although with a limiting effect caused by PT. In the case of Runx2 at 14 DIV, an increase was only observed in Non-IR OTCs. These IHC data were consistent with the gene expression analysis for Bmp-2 and Runx2.

Bmp-2 signaling can subsequently activate the transcription factors Sox9 or Runx2. Sox9 is involved in promoting the differentiation of stem cells towards the chondrocyte lineage, while Runx2 plays a crucial role in driving chondrocytes towards hypertrophic differentiation and facilitating the expression of genes essential for matrix mineralization [27, 203]. Studies performed by Garrison et al. [204] and Nilsson et al. [205] identified an expression gradient for Bmp-2 within the GP. Their findings suggested that Bmp-2 stimulates chondrocyte proliferation within the MZ while initiating hypertrophic differentiation in the pre-hypertrophic zone. Based on our data, it appears that growth abnormalities following proton IR may result from decreased Bmp-2 and, consequently, reduced downstream Runx2 signaling. This suggests the loss of MSCs that would normally differentiate into proliferating chondrocytes, as well as the loss of pre-hypertrophic chondrocytes responsible for bone elongation. Consequently, this disruption or loss of bone elongation leads to growth abnormalities.

Bone homeostasis relies on the coordinated actions of osteoblasts, responsible for the deposition of osteoid and osteoclasts, which resorb different matrices [206]. An imbalance in the numbers and activity of osteoclasts and osteoblasts following RT is believed to be a contributing factor to weakened bone structures and an increased risk of necrosis or fractures [207]. Consequently, we investigated the impact of particle IR on the activation and function of osteoclasts and osteoblasts. The differentiation and activity of osteoclasts is regulated through the Opg/RankL signaling pathway. The binding of RankL to its receptor, Rank, triggers the activation of osteoclasts. In contrast, when Opg binds to the receptor, it covers the binding site for RankL, thereby inhibiting osteoclast activation [208]. Following particle IR, we observed that although Opg staining was not as widespread within the proximal epiphysis of the OTCs, the staining intensity increased after 14 DIV in C-ions IR OTC's. This finding was further confirmed at gene expression level, particularly following C-ions IR, resulting in a highly significant reduction in Opg expression. Interestingly, while it was thought that particularly osteoblast secrete Opg to prevent further bone resorption, recent studies found that Opg produced by hypertrophic chondrocytes is central for the differentiation of osteoclast [209–211]. Mature osteoblast are marked by the expression of alkaline phosphatase [212]. In our OTCs, particle IR had no immediately noticeable effect on the development and maturation of osteoblasts. However, we observed a significant downregulation of Alpl gene expression after 14 DIV. This is consistent with the findings of other studies, which have demonstrated that while osteoblast numbers typically remain stable following irradiation, the functionality of osteoblasts, including osteoid production and the mineralization process, can be adversely affected [207, 213–215].

6.4 Limitations

Part one of this dissertation has already addressed the methodological limitations stemming from the absence of vascularization, blood flow, and, consequently, the lack of systemic factors. Additionally, the restricted presence of inflammatory/immune cells must also be taken into account in part two of the dissertation. Furthermore, a study-specific limitation is the use of a single-dose IR approach instead of the in the clinic commonly employed fractionated multiple-dosage irradiation scheme during treatment. Regrettably, due to limited access to the MedAustron facilities, the study was unable to investigate the impact of single-dose versus fractionated IR on postnatal bone development.

In addition to the challenge of precisely timing the birth of the rats to the fixed dates of the MedAustron facility, we were constrained in our ability to explore only two specific time points for assessing the impact of particle IR on postnatal bone development. These time points were chosen to represent immediate effects (1 DIV) and intermediate-term effects (14 DIV) of the irradiation on bone development.

6.5 Conclusion and Outlook

In conclusion, our organotypic ex-vivo femoral slices culture offers a robust method for investigating the pathology and subsequent regenerative processes within the postnatal GP following particle IR ex vivo. We observed an initial substantial decrease in proliferating chondrocytes at 1 DIV followed by regenerative attempts through the formation of chondrocytic clones at 14 DIV. Additionally, we observed an accelerated ECM mineralization process, which correlated with an increase in the production and secretion of PG into the territorial and inter-territorial matrix. During the in vitro cultivation period, the expression of ECM marker Col2a1 exhibited a notable increase but was significantly inhibited by particle IR. Furthermore, the decrease in Col10a1 expression over time was more pronounced when compared to the Non-IR control OTCs. Significantly, chondrogenic markers such as Bmp-2, Runx2, Opg and the osteogenic marker Alp, showed a noteworthy reduction in their expression increase after 14 DIV due to particle IR, while C-ions IR had a more pounced impact than proton IR.

The similarity to the in vivo studies makes this new methodology a powerful tool and will enhance our understanding of the cellular radiobiological processes associated with PT, ultimately contributing to the optimization of therapy strategies for paediatric tumor patients. While extensive research is ongoing to mitigate or prevent the adverse effects of radiation therapy in pediatric patients, there remains a notable deficiency in new advancements. Approaches aimed at reducing growth arrest and angular deformities have encompassed strategies such as fractionation, hyperfractionation, and the utilization of chemical radioprotectors [100]. Due to the comparable results gained with our ex vivo OTC to the in vivo setting, our methodology provides a unique opportunity to evaluate a range of radioprotectors with a high-throughput approach and real-time analysis.

Furthermore, as ex vivo organ cultures gain increasing popularity, this ex vivo bone culture can contribute to the reduction of the still required animal experiments. Consequently, as we continue to enhance the ex vivo femur culture, our objective is to achieve multiple slices per bone, prolong their in vitro cultivation lifespan, and expand these cultures to other types of bones for multiple applications. This endeavour aligns with the principles of the 3R concept, which seeks to reduce, refine, and replace animal experiments in scientific research.

7 References

1. Etschmaier V, Üçal M, Lohberger B, Absenger-Novak M, Kolb D, Weinberg A, Schäfer U. Disruption of Endochondral Ossification and Extracellular Matrix Maturation in an Ex Vivo Rat Femur Organotypic Slice Model Due to Growth Plate Injury. Cells 2023. doi:10.3390/cells12131687.
2. Etschmaier V, Glänzer D, Eck N, Schäfer U, Leithner A, Georg D, Lohberger B. Proton and Carbon Ion Irradiation Changes the Process of Endochondral Ossification in an Ex Vivo Femur Organotypic Culture Model. Cells 2023. doi:10.3390/cells12182301.
3. Breeland G, Sinkler MA, Menezes RG, editors. StatPearls: Embryology, Bone Ossification. Treasure Island (FL); 2023.
4. Percival CJ, Richtsmeier JT. Angiogenesis and intramembranous osteogenesis. Dev Dyn. 2013;242:909–22. doi:10.1002/dvdy.23992.
5. Ortega N, Behonick DJ, Werb Z. Matrix remodeling during endochondral ossification. Trends Cell Biol. 2004;14:86–93. doi:10.1016/j.tcb.2003.12.003.
6. Thompson EM, Matsiko A, Farrell E, Kelly DJ, O'Brien FJ. Recapitulating endochondral ossification: a promising route to in vivo bone regeneration. J Tissue Eng Regen Med. 2015;9:889–902. doi:10.1002/term.1918.
7. Yun HH, Kim H-J, Jeong M-S, Choi Y-S, Seo J-Y. Changes of the growth plate in children: 3-dimensional magnetic resonance imaging analysis. Korean J Pediatr. 2018;61:226–30. doi:10.3345/kjp.2018.61.7.226.
8. Hunziker EB. Mechanism of longitudinal bone growth and its regulation by growth plate chondrocytes. Microsc Res Tech. 1994;28:505–19. doi:10.1002/jemt.1070280606.
9. Hunziker EB, Schenk RK. Physiological mechanisms adopted by chondrocytes in regulating longitudinal bone growth in rats. J Physiol. 1989;414:55–71. doi:10.1113/jphysiol.1989.sp017676.
10. Nguyen JC, Markhardt BK, Merrow AC, Dwek JR. Imaging of Pediatric Growth Plate Disturbances. Radiographics. 2017;37:1791–812. doi:10.1148/rg.2017170029.
11. Abad V, Meyers JL, Weise M, Gafni RI, Barnes KM, Nilsson O, et al. The role of the resting zone in growth plate chondrogenesis. Endocrinology. 2002;143:1851–7. doi:10.1210/endo.143.5.8776.
12. Hallett SA, Ono W, Ono N. Growth Plate Chondrocytes: Skeletal Development, Growth and Beyond. Int J Mol Sci 2019. doi:10.3390/ijms20236009.
13. Mizuhashi K, Ono W, Matsushita Y, Sakagami N, Takahashi A, Saunders TL, et al. Resting zone of the growth plate houses a unique class of skeletal stem cells. Nature. 2018;563:254–8. doi:10.1038/s41586-018-0662-5.

14. Kronenberg HM, Chung U. The parathyroid hormone-related protein and Indian hedgehog feedback loop in the growth plate. Novartis Found Symp. 2001;232:144-52; discussion 152-7. doi:10.1002/0470846658.ch10.
15. Hallett SA, Matsushita Y, Ono W, Sakagami N, Mizuhashi K, Tokavanich N, et al. Chondrocytes in the resting zone of the growth plate are maintained in a Wnt-inhibitory environment. Elife 2021. doi:10.7554/eLife.64513.
16. St-Jacques B, Hammerschmidt M, McMahon AP. Indian hedgehog signaling regulates proliferation and differentiation of chondrocytes and is essential for bone formation. Genes Dev. 1999;13:2072–86. doi:10.1101/gad.13.16.2072.
17. Tiet TD, Alman BA. Developmental pathways in musculoskeletal neoplasia: involvement of the Indian Hedgehog-parathyroid hormone-related protein pathway. Pediatr Res. 2003;53:539–43. doi:10.1203/01.PDR.0000054688.93486.18.
18. Bonucci E. Calcification in biological systems. Boca Raton: CRC Press; 1992.
19. Aghajanian P, Mohan S. The art of building bone: emerging role of chondrocyte-to-osteoblast transdifferentiation in endochondral ossification. Bone Res. 2018;6:19. doi:10.1038/s41413-018-0021-z.
20. Qin X, Jiang Q, Nagano K, Moriishi T, Miyazaki T, Komori H, et al. Runx2 is essential for the transdifferentiation of chondrocytes into osteoblasts. PLoS Genet. 2020;16:e1009169. doi:10.1371/journal.pgen.1009169.
21. Lui JC, Yue S, Lee A, Kikani B, Temnycky A, Barnes KM, Baron J. Persistent Sox9 expression in hypertrophic chondrocytes suppresses transdifferentiation into osteoblasts. Bone. 2019;125:169–77. doi:10.1016/j.bone.2019.05.027.
22. Haseeb A, Kc R, Angelozzi M, Charleroy C de, Rux D, Tower RJ, et al. SOX9 keeps growth plates and articular cartilage healthy by inhibiting chondrocyte dedifferentiation/osteoblastic redifferentiation. Proc Natl Acad Sci U S A 2021. doi:10.1073/pnas.2019152118.
23. Dy P, Wang W, Bhattaram P, Wang Q, Wang L, Ballock RT, Lefebvre V. Sox9 directs hypertrophic maturation and blocks osteoblast differentiation of growth plate chondrocytes. Dev Cell. 2012;22:597–609. doi:10.1016/j.devcel.2011.12.024.
24. Rashid H, Chen H, Javed A. Runx2 is required for hypertrophic chondrocyte mediated degradation of cartilage matrix during endochondral ossification. Matrix Biol Plus. 2021;12:100088. doi:10.1016/j.mbplus.2021.100088.
25. Choi JY, Pratap J, Javed A, Zaidi SK, Xing L, Balint E, et al. Subnuclear targeting of Runx/Cbfa/AML factors is essential for tissue-specific differentiation during embryonic development. Proc Natl Acad Sci U S A. 2001;98:8650–5. doi:10.1073/pnas.151236498.

26. Hinoi E, Bialek P, Chen Y-T, Rached M-T, Groner Y, Behringer RR, et al. Runx2 inhibits chondrocyte proliferation and hypertrophy through its expression in the perichondrium. Genes Dev. 2006;20:2937–42. doi:10.1101/gad.1482906.
27. Komori T. Runx2, an inducer of osteoblast and chondrocyte differentiation. Histochem Cell Biol. 2018;149:313–23. doi:10.1007/s00418-018-1640-6.
28. Zhou X, Mark K von der, Henry S, Norton W, Adams H, Crombrugghe B de. Chondrocytes transdifferentiate into osteoblasts in endochondral bone during development, postnatal growth and fracture healing in mice. PLoS Genet. 2014;10:e1004820. doi:10.1371/journal.pgen.1004820.
29. Cortes M, Baria AT, Schwartz NB. Sulfation of chondroitin sulfate proteoglycans is necessary for proper Indian hedgehog signaling in the developing growth plate. Development. 2009;136:1697–706. doi:10.1242/dev.030742.
30. Faienza MF, Chiarito M, Brunetti G, D'Amato G. Growth plate gene involment and isolated short stature. Endocrine. 2021;71:28–34. doi:10.1007/s12020-020-02362-w.
31. Kusindarta DL, Wihadmadyatami H, editors. The Role of Extracellular Matrix in Tissue Regeneration: IntechOpen; 2018.
32. Aszódi A, Pfeifer A, Wendel M, Hiripi L, Fässler R. Mouse models for extracellular matrix diseases. J Mol Med (Berl). 1998;76:238–52. doi:10.1007/s001090050214.
33. Bateman JF, Boot-Handford RP, Lamandé SR. Genetic diseases of connective tissues: cellular and extracellular effects of ECM mutations. Nat Rev Genet. 2009;10:173–83. doi:10.1038/nrg2520.
34. Ballock RT, O'Keefe RJ. Physiology and pathophysiology of the growth plate. Birth Defects Res C Embryo Today. 2003;69:123–43. doi:10.1002/bdrc.10014.
35. Gustafsson E, Aszodi A, Ortega N, Hunziker EB, Denker H-W, Werb Z, Fassler R. Role of collagen type II and perlecan in skeletal development. Ann N Y Acad Sci. 2003;995:140–50. doi:10.1111/j.1749-6632.2003.tb03217.x.
36. Behonick DJ, Werb Z. A bit of give and take: the relationship between the extracellular matrix and the developing chondrocyte. Mech Dev. 2003;120:1327–36. doi:10.1016/j.mod.2003.05.002.
37. Keene DR, Oxford JT, Morris NP. Ultrastructural localization of collagen types II, IX, and XI in the growth plate of human rib and fetal bovine epiphyseal cartilage: type XI collagen is restricted to thin fibrils. J Histochem Cytochem. 1995;43:967–79. doi:10.1177/43.10.7560887.
38. Alvarez J, Balbín M, Fernández M, López JM. Collagen metabolism is markedly altered in the hypertrophic cartilage of growth plates from rats with growth impairment secondary

to chronic renal failure. J Bone Miner Res. 2001;16:511–24. doi:10.1359/jbmr.2001.16.3.511.

39. Freije JM, Díez-Itza I, Balbín M, Sánchez LM, Blasco R, Tolivia J, López-Otín C. Molecular cloning and expression of collagenase-3, a novel human matrix metalloproteinase produced by breast carcinomas. J Biol Chem. 1994;269:16766–73.
40. Warman ML, Cormier-Daire V, Hall C, Krakow D, Lachman R, LeMerrer M, et al. Nosology and classification of genetic skeletal disorders: 2010 revision. Am J Med Genet A. 2011;155A:943–68. doi:10.1002/ajmg.a.33909.
41. Vandenberg P, Khillan JS, Prockop DJ, Helminen H, Kontusaari S, Ala-Kokko L. Expression of a partially deleted gene of human type II procollagen (COL2A1) in transgenic mice produces a chondrodysplasia. Proc Natl Acad Sci U S A. 1991;88:7640–4. doi:10.1073/pnas.88.17.7640.
42. Jacenko O, LuValle P, Solum K, Olsen BR. A dominant negative mutation in the alpha 1 (X) collagen gene produces spondylometaphyseal defects in mice. Prog Clin Biol Res. 1993;383B:427–36.
43. Jacenko O, LuValle PA, Olsen BR. Spondylometaphyseal dysplasia in mice carrying a dominant negative mutation in a matrix protein specific for cartilage-to-bone transition. Nature. 1993;365:56–61. doi:10.1038/365056a0.
44. Kwan KM, Pang MK, Zhou S, Cowan SK, Kong RY, Pfordte T, et al. Abnormal compartmentalization of cartilage matrix components in mice lacking collagen X: implications for function. J Cell Biol. 1997;136:459–71. doi:10.1083/jcb.136.2.459.
45. Gress CJ, Jacenko O. Growth plate compressions and altered hematopoiesis in collagen X null mice. J Cell Biol. 2000;149:983–93. doi:10.1083/jcb.149.4.983.
46. Aszódi A, Bateman JF, Gustafsson E, Boot-Handford R, Fässler R. Mammalian skeletogenesis and extracellular matrix: what can we learn from knockout mice? Cell Struct Funct. 2000;25:73–84. doi:10.1247/csf.25.73.
47. Heinegård D. Fell-Muir Lecture: Proteoglycans and more--from molecules to biology. Int J Exp Pathol. 2009;90:575–86. doi:10.1111/j.1365-2613.2009.00695.x.
48. Schaefer L, Iozzo RV. Biological functions of the small leucine-rich proteoglycans: from genetics to signal transduction. J Biol Chem. 2008;283:21305–9. doi:10.1074/jbc.R800020200.
49. Ng L, Grodzinsky AJ, Patwari P, Sandy J, Plaas A, Ortiz C. Individual cartilage aggrecan macromolecules and their constituent glycosaminoglycans visualized via atomic force microscopy. J Struct Biol. 2003;143:242–57. doi:10.1016/j.jsb.2003.08.006.

50. Chandran PL, Horkay F. Aggrecan, an unusual polyelectrolyte: review of solution behavior and physiological implications. Acta Biomater. 2012;8:3–12. doi:10.1016/j.actbio.2011.08.011.
51. Myllyharju J. Extracellular matrix and developing growth plate. Curr Osteoporos Rep. 2014;12:439–45. doi:10.1007/s11914-014-0232-1.
52. Wai AW, Ng LJ, Watanabe H, Yamada Y, Tam PP, Cheah KS. Disrupted expression of matrix genes in the growth plate of the mouse cartilage matrix deficiency (cmd) mutant. Dev Genet. 1998;22:349–58. doi:10.1002/(SICI)1520-6408(1998)22:4<349::AID-DVG5>3.0.CO;2-6.
53. Watanabe H, Kimata K, Line S, Strong D, Gao LY, Kozak CA, Yamada Y. Mouse cartilage matrix deficiency (cmd) caused by a 7 bp deletion in the aggrecan gene. Nat Genet. 1994;7:154–7. doi:10.1038/ng0694-154.
54. Karamanos NK, Theocharis AD, Piperigkou Z, Manou D, Passi A, Skandalis SS, et al. A guide to the composition and functions of the extracellular matrix. FEBS J. 2021;288:6850–912. doi:10.1111/febs.15776.
55. Melrose J, Shu C, Whitelock JM, Lord MS. The cartilage extracellular matrix as a transient developmental scaffold for growth plate maturation. Matrix Biol. 2016;52-54:363–83. doi:10.1016/j.matbio.2016.01.008.
56. Hecht JT, Hayes E, Haynes R, Cole WG, Long RJ, Farach-Carson MC, Carson DD. Differentiation-induced loss of heparan sulfate in human exostosis derived chondrocytes. Differentiation. 2005;73:212–21. doi:10.1111/j.1432-0436.2005.00025.x.
57. Gerber HP, Hillan KJ, Ryan AM, Kowalski J, Keller GA, Rangell L, et al. VEGF is required for growth and survival in neonatal mice. Development. 1999;126:1149–59. doi:10.1242/dev.126.6.1149.
58. Egeblad M, Werb Z. New functions for the matrix metalloproteinases in cancer progression. Nat Rev Cancer. 2002;2:161–74. doi:10.1038/nrc745.
59. Meszaros E, Malemud CJ. Prospects for treating osteoarthritis: enzyme-protein interactions regulating matrix metalloproteinase activity. Ther Adv Chronic Dis. 2012;3:219–29. doi:10.1177/2040622312454157.
60. Mackie EJ, Ahmed YA, Tatarczuch L, Chen K-S, Mirams M. Endochondral ossification: how cartilage is converted into bone in the developing skeleton. Int J Biochem Cell Biol. 2008;40:46–62. doi:10.1016/j.biocel.2007.06.009.
61. Inada M, Wang Y, Byrne MH, Rahman MU, Miyaura C, López-Otín C, Krane SM. Critical roles for collagenase-3 (Mmp13) in development of growth plate cartilage and in

endochondral ossification. Proc Natl Acad Sci U S A. 2004;101:17192–7. doi:10.1073/pnas.0407788101.

62. Salhotra A, Shah HN, Levi B, Longaker MT. Mechanisms of bone development and repair. Nat Rev Mol Cell Biol. 2020;21:696–711. doi:10.1038/s41580-020-00279-w.
63. Si J, Wang C, Zhang D, Wang B, Zhou Y. Osteopontin in Bone Metabolism and Bone Diseases. Med Sci Monit. 2020;26:e919159. doi:10.12659/MSM.919159.
64. Schaffler MB, Kennedy OD. Osteocyte signaling in bone. Curr Osteoporos Rep. 2012;10:118–25. doi:10.1007/s11914-012-0105-4.
65. Kang JH, Ko HM, Moon JS, Yoo HI, Jung JY, Kim MS, et al. Osteoprotegerin expressed by osteoclasts: an autoregulator of osteoclastogenesis. J Dent Res. 2014;93:1116–23. doi:10.1177/0022034514552677.
66. Udagawa N, Koide M, Nakamura M, Nakamichi Y, Yamashita T, Uehara S, et al. Osteoclast differentiation by RANKL and OPG signaling pathways. J Bone Miner Metab. 2021;39:19–26. doi:10.1007/s00774-020-01162-6.
67. Donabauer M, Pommer A. IDB Austria 2021 Verletzungsursachen in Österreich: Standarderhebung des KFV. 2023. https://www.kfv.at/download/idb-jahresbericht-2021/.
68. Kahl H, Dortschy R, Ellsässer G. Verletzungen bei Kindern und Jugendlichen (1-17 Jahre) und Umsetzung von persönlichen Schutzmassnahmen. Ergebnisse des bundesweiten Kinder- und Jugendgesundheitssurveys (KiGGS). [Injuries among children and adolescents (1-17 years) and implementation of safety measures. Results of the nationwide German Health Interview and Examination Survey for Children and Adolescents (KiGGS)]. Bundesgesundheitsblatt Gesundheitsforschung Gesundheitsschutz. 2007;50:718–27. doi:10.1007/s00103-007-0233-7.
69. Qiu X, Deng H, Su Q, Zeng S, Han S, Li S, et al. Epidemiology and management of 10,486 pediatric fractures in Shenzhen: experience and lessons to be learnt. BMC Pediatr. 2022;22:161. doi:10.1186/s12887-022-03199-0.
70. Levine RH, Thomas A, Nezwek TA, Waseem M, editors. StatPearls: Salter-Harris Fracture. Treasure Island (FL); 2023.
71. SALTER RB, HARRIS WR. Injuries Involving the Epiphyseal Plate. JBJS. 1963;45.
72. Cant DALW, Faergemann C. The incidence of physeal fractures in the lower limb and the frequency of premature physeal closure: a cohort study of 236 patients. Acta Orthop. 2023;94:289–94. doi:10.2340/17453674.2023.13429.
73. Little JT, Klionsky NB, Chaturvedi A, Soral A, Chaturvedi A. Pediatric Distal Forearm and Wrist Injury: An Imaging Review. Radiographics. 2014;34:472–90. doi:10.1148/rg.342135073.

74. Sananta P, Isnansyah Y, Rosandi RD, Sugiarto MA. The Management Growth Plate Injury in Animal Studies with Stem Cells Technique: Systematic Review. Acta Inform Med. 2022;30:53–6. doi:10.5455/aim.2022.30.53-56.
75. Chung R, Xian CJ. Recent research on the growth plate: Mechanisms for growth plate injury repair and potential cell-based therapies for regeneration. J Mol Endocrinol. 2014;53:T45-61. doi:10.1530/JME-14-0062.
76. Zhou FH, Foster BK, Sander G, Xian CJ. Expression of proinflammatory cytokines and growth factors at the injured growth plate cartilage in young rats. Bone. 2004;35:1307–15. doi:10.1016/j.bone.2004.09.014.
77. Zhou FH, Foster BK, Zhou X-F, Cowin AJ, Xian CJ. TNF-alpha mediates p38 MAP kinase activation and negatively regulates bone formation at the injured growth plate in rats. J Bone Miner Res. 2006;21:1075–88. doi:10.1359/jbmr.060410.
78. Chung R, Cool JC, Scherer MA, Foster BK, Xian CJ. Roles of neutrophil-mediated inflammatory response in the bony repair of injured growth plate cartilage in young rats. J Leukoc Biol. 2006;80:1272–80. doi:10.1189/jlb.0606365.
79. Xian CJ, Zhou FH, McCarty RC, Foster BK. Intramembranous ossification mechanism for bone bridge formation at the growth plate cartilage injury site. J Orthop Res. 2004;22:417–26. doi:10.1016/j.orthres.2003.08.003.
80. Macsai CE, Hopwood B, Chung R, Foster BK, Xian CJ. Structural and molecular analyses of bone bridge formation within the growth plate injury site and cartilage degeneration at the adjacent uninjured area. Bone. 2011;49:904–12. doi:10.1016/j.bone.2011.07.024.
81. Neumayer B, Amerstorfer E, Diwoky C, Lindtner RA, Wadl E, Scheurer E, et al. Assessment of pharmacokinetics for microvessel proliferation by DCE-MRI for early detection of physeal bone bridge formation in an animal model. MAGMA. 2017;30:417–27. doi:10.1007/s10334-017-0615-2.
82. Ngo TQ, Scherer MA, Zhou FH, Foster BK, Xian CJ. Expression of bone morphogenic proteins and receptors at the injured growth plate cartilage in young rats. J Histochem Cytochem. 2006;54:945–54. doi:10.1369/jhc.6A6939.2006.
83. Chung R, Foster BK, Zannettino ACW, Xian CJ. Potential roles of growth factor PDGF-BB in the bony repair of injured growth plate. Bone. 2009;44:878–85. doi:10.1016/j.bone.2009.01.377.
84. Fischerauer E, Heidari N, Neumayer B, Deutsch A, Weinberg AM. The spatial and temporal expression of VEGF and its receptors 1 and 2 in post-traumatic bone bridge

formation of the growth plate. J Mol Histol. 2011;42:513–22. doi:10.1007/s10735-011-9359-x.

85. Yang Y-Q, Tan Y-Y, Wong R, Wenden A, Zhang L-K, Rabie ABM. The role of vascular endothelial growth factor in ossification. Int J Oral Sci. 2012;4:64–8. doi:10.1038/ijos.2012.33.
86. Wang X, Li Z, Wang C, Bai H, Wang Z, Liu Y, et al. Enlightenment of Growth Plate Regeneration Based on Cartilage Repair Theory: A Review. Front Bioeng Biotechnol. 2021;9:654087. doi:10.3389/fbioe.2021.654087.
87. Chung R, Foster BK, Xian CJ. Injury responses and repair mechanisms of the injured growth plate. Front Biosci (Schol Ed). 2011;3:117–25. doi:10.2741/s137.
88. Baumgart R. The reverse planning method for lengthening of the lower limb using a straight intramedullary nail with or without deformity correction. A new method. Oper Orthop Traumatol. 2009;21:221–33. doi:10.1007/s00064-009-1709-4.
89. Langenskiöld A. Surgical treatment of partial closure of the growth plate. J Pediatr Orthop. 1981;1:3–11. doi:10.1097/01241398-198101010-00002.
90. Tobita M, Ochi M, Uchio Y, Mori R, Iwasa J, Katsube K, Motomura T. Treatment of growth plate injury with autogenous chondrocytes: a study in rabbits. Acta Orthop Scand. 2002;73:352–8. doi:10.1080/000164702320155383.
91. Roebuck DJ. Skeletal complications in pediatric oncology patients. Radiographics. 1999;19:873–85. doi:10.1148/radiographics.19.4.g99jl01873.
92. Bassal M, Mertens AC, Taylor L, Neglia JP, Greffe BS, Hammond S, et al. Risk of selected subsequent carcinomas in survivors of childhood cancer: a report from the Childhood Cancer Survivor Study. J Clin Oncol. 2006;24:476–83. doi:10.1200/JCO.2005.02.7235.
93. Oeffinger KC, Mertens AC, Sklar CA, Kawashima T, Hudson MM, Meadows AT, et al. Chronic health conditions in adult survivors of childhood cancer. N Engl J Med. 2006;355:1572–82. doi:10.1056/NEJMsa060185.
94. Mitchell MJ, Logan PM. Radiation-induced changes in bone. Radiographics. 1998;18:1125-36; quiz 1242-3. doi:10.1148/radiographics.18.5.9747611.
95. Paulino AC. Late effects of radiotherapy for pediatric extremity sarcomas. Int J Radiat Oncol Biol Phys. 2004;60:265–74. doi:10.1016/j.ijrobp.2004.02.001.
96. Emerzian SR, Wu T, Vaidya R, Tang SY, Abergel RJ, Keaveny TM. Relative Effects of Radiation-Induced Changes in Bone Mass, Structure, and Tissue Material on Vertebral Strength in a Rat Model. J Bone Miner Res. 2023;38:1032–42. doi:10.1002/jbmr.4828.

97. Chung CS, Yock TI, Nelson K, Xu Y, Keating NL, Tarbell NJ. Incidence of second malignancies among patients treated with proton versus photon radiation. Int J Radiat Oncol Biol Phys. 2013;87:46–52. doi:10.1016/j.ijrobp.2013.04.030.

98. Horton JA, Margulies BS, Strauss JA, Bariteau JT, Damron TA, Spadaro JA, Farnum CE. Restoration of growth plate function following radiotherapy is driven by increased proliferative and synthetic activity of expansions of chondrocytic clones. J Orthop Res. 2006;24:1945–56. doi:10.1002/jor.20251.

99. Damron TA, Margulies BS, Strauss JA, O'Hara K, Spadaro JA, Farnum CE. Sequential histomorphometric analysis of the growth plate following irradiation with and without radioprotection. JBJS. 2003;85:1302–13. doi:10.2106/00004623-200307000-00017.

100. Damron TA, Horton JA, Pritchard MR, Stringer MT, Margulies BS, Strauss JA, et al. Histomorphometric evidence of growth plate recovery potential after fractionated radiotherapy: an in vivo model. Radiat Res. 2008;170:284–91. doi:10.1667/RR1254.1.

101. Barcellos-Hoff MH, Park C, Wright EG. Radiation and the microenvironment - tumorigenesis and therapy. Nat Rev Cancer. 2005;5:867–75. doi:10.1038/nrc1735.

102. Radford IR, Murphy TK, Radley JM, Ellis SL. Radiation response of mouse lymphoid and myeloid cell lines. Part II. Apoptotic death is shown by all lines examined. International Journal of Radiation Biology. 1994;65:217–27. doi:10.1080/09553009414550251.

103. Little JB. Cellular effects of ionizing radiation. N Engl J Med. 1968;278:369-76 concl. doi:10.1056/NEJM196802152780705.

104. Little JB, Nagasawa H. Effect of confluent holding on potentially lethal damage repair, cell cycle progression, and chromosomal aberrations in human normal and ataxia-telangiectasia fibroblasts. Radiat Res. 1985;101:81–93.

105. Santis M de, Cesari E, Nobili E, Straface G, Cavaliere AF, Caruso A. Radiation effects on development. Birth Defects Res C Embryo Today. 2007;81:177–82. doi:10.1002/bdrc.20099.

106. Guan X, Gao J, Hu J, Hu W, Yang J, Qiu X, et al. The preliminary results of proton and carbon ion therapy for chordoma and chondrosarcoma of the skull base and cervical spine. Radiat Oncol. 2019;14:206. doi:10.1186/s13014-019-1407-9.

107. Grau C, Durante M, Georg D, Langendijk JA, Weber DC. Particle therapy in Europe. Mol Oncol. 2020;14:1492–9. doi:10.1002/1878-0261.12677.

108. Schulz-Ertner D, Tsujii H. Particle radiation therapy using proton and heavier ion beams. J Clin Oncol. 2007;25:953–64. doi:10.1200/JCO.2006.09.7816.

109. Durante M, Debus J. Heavy Charged Particles: Does Improved Precision and Higher Biological Effectiveness Translate to Better Outcome in Patients? Semin Radiat Oncol. 2018;28:160–7. doi:10.1016/j.semradonc.2017.11.004.
110. CERN. CERN Yellow Reports: Monographs, Vol 2 (2019): A Facility for Tumour Therapy and Biomedical Research in South-Eastern Europe. doi:10.23731/CYRM-2019-002.
111. Lohberger B, Barna S, Glänzer D, Eck N, Kerschbaum-Gruber S, Stasny K, et al. Cellular and Molecular Biological Alterations after Photon, Proton, and Carbon Ions Irradiation in Human Chondrosarcoma Cells Linked with High-Quality Physics Data. Int J Mol Sci 2022. doi:10.3390/ijms231911464.
112. Hayden PJ, Harbell JW. Special review series on 3D organotypic culture models: Introduction and historical perspective. In Vitro Cell Dev Biol Anim. 2021;57:95–103. doi:10.1007/s11626-020-00500-2.
113. Gurkan UA, Kishore V, Condon KW, Bellido TM, Akkus O. A scaffold-free multicellular three-dimensional in vitro model of osteogenesis. Calcif Tissue Int. 2011;88:388–401. doi:10.1007/s00223-011-9467-3.
114. Moran CJ, Ramesh A, Brama PAJ, O'Byrne JM, O'Brien FJ, Levingstone TJ. The benefits and limitations of animal models for translational research in cartilage repair. J Exp Orthop. 2016;3:1. doi:10.1186/s40634-015-0037-x.
115. Simon F, Oberhuber A, Schelzig H. Advantages and Disadvantages of Different Animal Models for Studying Ischemia/Reperfusion Injury of the Spinal Cord. European Journal of Vascular and Endovascular Surgery. 2015;49:744. doi:10.1016/j.ejvs.2015.03.041.
116. Shamir ER, Ewald AJ. Three-dimensional organotypic culture: experimental models of mammalian biology and disease. Nat Rev Mol Cell Biol. 2014;15:647–64. doi:10.1038/nrm3873.
117. Humpel C. Organotypic brain slice cultures: A review. Neuroscience. 2015;305:86–98. doi:10.1016/j.neuroscience.2015.07.086.
118. Srinivasaiah S, Musumeci G, Mohan T, Castrogiovanni P, Absenger-Novak M, Zefferer U, et al. A 300 µm Organotypic Bone Slice Culture Model for Temporal Investigation of Endochondral Osteogenesis. Tissue Eng Part C Methods. 2019;25:197–212. doi:10.1089/ten.TEC.2018.0368.
119. Abubakar AA, Noordin MM, Azmi TI, Kaka U, Loqman MY. The use of rats and mice as animal models in ex vivo bone growth and development studies. Bone Joint Res. 2016;5:610–8. doi:10.1302/2046-3758.512.BJR-2016-0102.R2.

120. Gothard D, Smith EL, Kanczler JM, Rashidi H, Qutachi O, Henstock J, et al. Tissue engineered bone using select growth factors: A comprehensive review of animal studies and clinical translation studies in man. Eur Cell Mater. 2014;28:166-207; discussion 207-8. doi:10.22203/ecm.v028a13.

121. Chagin AS, Karimian E, Sundström K, Eriksson E, Sävendahl L. Catch-up growth after dexamethasone withdrawal occurs in cultured postnatal rat metatarsal bones. J Endocrinol. 2010;204:21–9. doi:10.1677/JOE-09-0307.

122. Marino S, Staines KA, Brown G, Howard-Jones RA, Adamczyk M. Models of ex vivo explant cultures: applications in bone research. Bonekey Rep. 2016;5:818. doi:10.1038/bonekey.2016.49.

123. Johnson S, Rabinovitch P. Ex vivo imaging of excised tissue using vital dyes and confocal microscopy. Curr Protoc Cytom. 2012;Chapter 9:Unit 9.39. doi:10.1002/0471142956.cy0939s61.

124. Goodhew PJ, Humphreys J, editors. Electron Microscopy and Analysis: CRC Press; 2000.

125. Alturkistani HA, Tashkandi FM, Mohammedsaleh ZM. Histological Stains: A Literature Review and Case Study. Glob J Health Sci. 2015;8:72–9. doi:10.5539/gjhs.v8n3p72.

126. Fischer AH, Jacobson KA, Rose J, Zeller R. Hematoxylin and eosin staining of tissue and cell sections. CSH Protoc. 2008;2008:pdb.prot4986. doi:10.1101/pdb.prot4986.

127. Sun Y, Helmholz H, Willumeit-Römer R. Multicolor Histochemical Staining for Identification of Mineralized and Non-Mineralized Musculoskeletal Tissue: Immunohistochemical and Radiological Validation in Decalcified Bone Samples. Bioengineering (Basel) 2022. doi:10.3390/bioengineering9100488.

128. Torzewski M. Die Movat-Pentachromfärbung – eine farbenprächtige Darstellung verschiedener zellulärer und extrazellulärer Gewebskomponenten. MK. 2015;2:204–8. doi:10.5414/MKX0060.

129. Banaszkiewicz PA, Kader DF, editors. Chemical Basis for the Histological Use of Safranin O in the Study of Articular Cartilage. London: Springer; 2014.

130. Kahveci Z, Minbay FZ, Cavusoglu L. Safranin O staining using a microwave oven. Biotech Histochem. 2000;75:264–8. doi:10.3109/10520290009085130.

131. Zinck N, Franz-Odendaal TA. Accurate whole-mount bone and cartilage staining requires acid-free conditions. Anat Rec (Hoboken). 2021;304:958–60. doi:10.1002/ar.24526.

132. Frith JC, Mönkkönen J, Blackburn GM, Russell RG, Rogers MJ. Clodronate and liposome-encapsulated clodronate are metabolized to a toxic ATP analog, adenosine 5'-

(beta, gamma-dichloromethylene) triphosphate, by mammalian cells in vitro. J Bone Miner Res. 1997;12:1358–67. doi:10.1359/jbmr.1997.12.9.1358.

133. Magaki S, Hojat SA, Wei B, So A, Yong WH. An Introduction to the Performance of Immunohistochemistry. Methods Mol Biol. 2019;1897:289–98. doi:10.1007/978-1-4939-8935-5_25.

134. Dabbs DJ, editor. Diagnostic Immunohistochemistry E-Book: Theranostic and Genomic Applications. 6th ed. Philadelphia: Elsevier; 2023.

135. Higuchi R, Fockler C, Dollinger G, Watson R. Kinetic PCR analysis: real-time monitoring of DNA amplification reactions. Biotechnology (N Y). 1993;11:1026–30. doi:10.1038/nbt0993-1026.

136. Heid CA, Stevens J, Livak KJ, Williams PM. Real time quantitative PCR. Genome Res. 1996;6:986–94. doi:10.1101/gr.6.10.986.

137. Stock M, Georg D, Ableitinger A, Zechner A, Utz A, Mumot M, et al. The technological basis for adaptive ion beam therapy at MedAustron: Status and outlook. Z Med Phys. 2018;28:196–210. doi:10.1016/j.zemedi.2017.09.007.

138. Ruangchan S, Knäusl B, Fuchs H, Georg D, Clausen M. Experimental benchmarking of RayStation proton dose calculation algorithms inside and outside the target region in heterogeneous phantom geometries. Phys Med. 2020;76:182–93. doi:10.1016/j.ejmp.2020.07.010.

139. Erickson CB, Shaw N, Hadley-Miller N, Riederer MS, Krebs MD, Payne KA. A Rat Tibial Growth Plate Injury Model to Characterize Repair Mechanisms and Evaluate Growth Plate Regeneration Strategies. J Vis Exp 2017. doi:10.3791/55571.

140. Karlsson C, Thornemo M, Henriksson HB, Lindahl A. Identification of a stem cell niche in the zone of Ranvier within the knee joint. J Anat. 2009;215:355–63. doi:10.1111/j.1469-7580.2009.01115.x.

141. Shapiro F, Holtrop ME, Glimcher MJ. Organization and cellular biology of the perichondrial ossification groove of ranvier: a morphological study in rabbits. J Bone Joint Surg Am. 1977;59:703–23.

142. Muruganandan S, Pierce R, Teguh DA, Perez RF, Bell N, Nguyen B, et al. A FoxA2+ long-term stem cell population is necessary for growth plate cartilage regeneration after injury. Nat Commun. 2022;13:2515. doi:10.1038/s41467-022-30247-1.

143. Matsushita Y, Nagata M, Kozloff KM, Welch JD, Mizuhashi K, Tokavanich N, et al. A Wnt-mediated transformation of the bone marrow stromal cell identity orchestrates skeletal regeneration. Nat Commun. 2020;11:332. doi:10.1038/s41467-019-14029-w.

144. Coleman RM, Phillips JE, Lin A, Schwartz Z, Boyan BD, Guldberg RE. Characterization of a small animal growth plate injury model using microcomputed tomography. Bone. 2010;46:1555–63. doi:10.1016/j.bone.2010.02.017.

145. Planka L, Srnec R, Rauser P, Stary D, Filova E, Jancar J, et al. Nanotechnology and mesenchymal stem cells with chondrocytes in prevention of partial growth plate arrest in pigs. Biomed Pap Med Fac Univ Palacky Olomouc Czech Repub. 2012;156:128–34. doi:10.5507/bp.2012.041.

146. Planka L, Gal P, Kecova H, Klima J, Hlucilova J, Filova E, et al. Allogeneic and autogenous transplantations of MSCs in treatment of the physeal bone bridge in rabbits. BMC Biotechnol. 2008;8:70. doi:10.1186/1472-6750-8-70.

147. Foster BK, Hansen AL, Gibson GJ, Hopwood JJ, Binns GF, Wiebkin OW. Reimplantation of growth plate chondrocytes into growth plate defects in sheep. J Orthop Res. 1990;8:555–64. doi:10.1002/jor.1100080412.

148. Fukuda S, Matsuoka O. Maturation process of secondary ossification centers in the rat and assessment of bone age. Jikken Dobutsu. 1979;28:1–9. doi:10.1538/expanim1978.28.1_1.

149. Fukuda S, Matsuoka O. Comparative studies on maturation process of secondary ossification centers of long bones in the mouse, rat, dog and monkey. Jikken Dobutsu. 1980;29:317–26. doi:10.1538/expanim1978.29.3_317.

150. Fan M, Wang Y, Liu Y, Qiang L, Guo R, Zhuang H, Zheng P. A New Method for Modeling Rabbit Growth Plate Injury for the Study of Tissue Engineering Scaffolds. Tissue Eng Part C Methods. 2022;28:489–97. doi:10.1089/ten.TEC.2022.0105.

151. Su Y-W, Chim SM, Zhou L, Hassanshahi M, Chung R, Fan C, et al. Osteoblast derived-neurotrophin-3 induces cartilage removal proteases and osteoclast-mediated function at injured growth plate in rats. Bone. 2018;116:232–47. doi:10.1016/j.bone.2018.08.010.

152. Musumeci G, Castrogiovanni P, Loreto C, Castorina S, Pichler K, Weinberg AM. Post-traumatic caspase-3 expression in the adjacent areas of growth plate injury site: a morphological study. Int J Mol Sci. 2013;14:15767–84. doi:10.3390/ijms140815767.

153. Lee MA, Nissen TP, Otsuka NY. Utilization of a Murine Model to Investigate the Molecular Process of Transphyseal Bone Formation. J Pediatr Orthop. 2000;20:802–6. doi:10.1097/01241398-200011000-00021.

154. Hajdu S, Schwendenwein E, Kaltenecker G, László I, Lang S, Vécsei V, Sarahrudi K. The effect of drilling and screw fixation of the growth plate--an experimental study in rabbits. J Orthop Res. 2011;29:1834–9. doi:10.1002/jor.21463.

155. Martin EA, Ritman EL, Turner RT. Time course of epiphyseal growth plate fusion in rat tibiae. Bone. 2003;32:261–7. doi:10.1016/s8756-3282(02)00983-3.

156. Basener CJ, Mehlman CT, DiPasquale TG. Growth disturbance after distal femoral growth plate fractures in children: a meta-analysis. J Orthop Trauma. 2009;23:663–7. doi:10.1097/BOT.0b013e3181a4f25b.

157. Sailhan F, Chotel F, Guibal A-L, Gollogly S, Adam P, Bérard J, Guibaud L. Three-dimensional MR imaging in the assessment of physeal growth arrest. Eur Radiol. 2004;14:1600–8. doi:10.1007/s00330-004-2319-z.

158. Newton PT, Li L, Zhou B, Schweingruber C, Hovorakova M, Xie M, et al. A radical switch in clonality reveals a stem cell niche in the epiphyseal growth plate. Nature. 2019;567:234–8. doi:10.1038/s41586-019-0989-6.

159. Bertrand J, Held A. Role of Proteoglycans in Osteoarthritis:63–80. doi:10.1007/978-3-319-45803-8_4.

160. Siffert RS. The effect of trauma to the epiphysis and growth plate. Skeletal Radiol. 1977;2:21–30. doi:10.1007/BF00364625.

161. Yasui N, Ono K, Konomi H, Nagai Y. Transitions in collagen types during endochondral ossification in human growth cartilage. Clin Orthop Relat Res. 1984:215–8.

162. Aigner T, Stöve J. Collagens--major component of the physiological cartilage matrix, major target of cartilage degeneration, major tool in cartilage repair. Adv Drug Deliv Rev. 2003;55:1569–93. doi:10.1016/j.addr.2003.08.009.

163. Gudmann NS, Karsdal MA. Type X Collagen:73–6. doi:10.1016/B978-0-12-809847-9.00010-6.

164. Kim HJ, Kirsch T. Collagen/annexin V interactions regulate chondrocyte mineralization. J Biol Chem. 2008;283:10310–7. doi:10.1074/jbc.M708456200.

165. Ballock RT, O', Keefe RJ. The Biology of the Growth Plate. JBJS. 2003;85:715. doi:aspx.

166. Stickens D, Behonick DJ, Ortega N, Heyer B, Hartenstein B, Yu Y, et al. Altered endochondral bone development in matrix metalloproteinase 13-deficient mice. Development. 2004;131:5883–95. doi:10.1242/dev.01461.

167. MacLean JJ, Lee CR, Alini M, Iatridis JC. The effects of short-term load duration on anabolic and catabolic gene expression in the rat tail intervertebral disc. J Orthop Res. 2005;23:1120–7. doi:10.1016/j.orthres.2005.01.020.

168. Pichler K, Herbert V, Schmidt B, Fischerauer EE, Leithner A, Weinberg A-M. Expression of matrix metalloproteinases in human growth plate chondrocytes is enhanced at high levels of mechanical loading: A possible explanation for overuse

injuries in children. Bone Joint J. 2013;95-B:568–73. doi:10.1302/0301-620X.95B4.30639.

169. Kozhemyakina E, Lassar AB, Zelzer E. A pathway to bone: signaling molecules and transcription factors involved in chondrocyte development and maturation. Development. 2015;142:817–31. doi:10.1242/dev.105536.

170. Tsukasaki M, Komatsu N, Negishi-Koga T, Huynh NC-N, Muro R, Ando Y, et al. Periosteal stem cells control growth plate stem cells during postnatal skeletal growth. Nat Commun. 2022;13:4166. doi:10.1038/s41467-022-31592-x.

171. Tao D, Zhang L, Ding Y, Tang N, Xu X, Li G, et al. Primary cilia support cartilage regeneration after injury. Int J Oral Sci. 2023;15:22. doi:10.1038/s41368-023-00223-6.

172. Zou S, Chen T, Wang Y, Tian R, Zhang L, Song P, et al. Mesenchymal stem cells overexpressing Ihh promote bone repair. J Orthop Surg Res. 2014;9:102. doi:10.1186/s13018-014-0102-7.

173. Chen L, Liu G, Li W, Wu X. Chondrogenic differentiation of bone marrow-derived mesenchymal stem cells following transfection with Indian hedgehog and sonic hedgehog using a rotary cell culture system. Cell Mol Biol Lett. 2019;24:16. doi:10.1186/s11658-019-0144-2.

174. Chen H, Ghori-Javed FY, Rashid H, Adhami MD, Serra R, Gutierrez SE, Javed A. Runx2 regulates endochondral ossification through control of chondrocyte proliferation and differentiation. J Bone Miner Res. 2014;29:2653–65. doi:10.1002/jbmr.2287.

175. Su Y-W, Wong DSK, Fan J, Chung R, Wang L, Chen Y, et al. Enhanced BMP signalling causes growth plate cartilage dysrepair in rats. Bone. 2021;145:115874. doi:10.1016/j.bone.2021.115874.

176. Jing J, Hinton RJ, Jing Y, Liu Y, Zhou X, Feng JQ. Osterix couples chondrogenesis and osteogenesis in post-natal condylar growth. J Dent Res. 2014;93:1014–21. doi:10.1177/0022034514549379.

177. Tang W, Yang F, Li Y, Crombrugghe B de, Jiao H, Xiao G, Zhang C. Transcriptional regulation of Vascular Endothelial Growth Factor (VEGF) by osteoblast-specific transcription factor Osterix (Osx) in osteoblasts. J Biol Chem. 2012;287:1671–8. doi:10.1074/jbc.M111.288472.

178. Behonick DJ, Xing Z, Lieu S, Buckley JM, Lotz JC, Marcucio RS, et al. Role of matrix metalloproteinase 13 in both endochondral and intramembranous ossification during skeletal regeneration. PLoS One. 2007;2:e1150. doi:10.1371/journal.pone.0001150.

179. Marenzana M, Arnett TR. The Key Role of the Blood Supply to Bone. Bone Res. 2013;1:203–15. doi:10.4248/BR201303001.

180. Portal-Núñez S, Lozano D, Esbrit P. Role of angiogenesis on bone formation. Histol Histopathol. 2012;27:559–66. doi:10.14670/HH-27.559.

181. Chung R, Foster BK, Xian CJ. The potential role of VEGF-induced vascularisation in the bony repair of injured growth plate cartilage. J Endocrinol. 2014;221:63–75. doi:10.1530/JOE-13-0539.

182. Erickson CB, Newsom JP, Fletcher NA, Yu Y, Rodriguez-Fontan F, Weatherford SA, et al. Anti-VEGF antibody delivered locally reduces bony bar formation following physeal injury in rats. J Orthop Res. 2021;39:1658–68. doi:10.1002/jor.24907.

183. Lorenzo J. The many ways of osteoclast activation. J Clin Invest. 2017;127:2530–2. doi:10.1172/JCI94606.

184. Pichler K, Musumeci G, Vielgut I, Martinelli E, Sadoghi P, Loreto C, Weinberg A-M. Towards a better understanding of bone bridge formation in the growth plate - an immunohistochemical approach. Connect Tissue Res. 2013;54:408–15. doi:10.3109/03008207.2013.828715.

185. Henriksen K, Bollerslev J, Everts V, Karsdal MA. Osteoclast activity and subtypes as a function of physiology and pathology--implications for future treatments of osteoporosis. Endocr Rev. 2011;32:31–63. doi:10.1210/er.2010-0006.

186. Boyle WJ, Simonet WS, Lacey DL. Osteoclast differentiation and activation. Nature. 2003;423:337–42. doi:10.1038/nature01658.

187. Romeo SG, Alawi KM, Rodrigues J, Singh A, Kusumbe AP, Ramasamy SK. Endothelial proteolytic activity and interaction with non-resorbing osteoclasts mediate bone elongation. Nat Cell Biol. 2019;21:430–41. doi:10.1038/s41556-019-0304-7.

188. Frade BB, Dias RB, Gemini Piperni S, Bonfim DC. The role of macrophages in fracture healing: a narrative review of the recent updates and therapeutic perspectives. Stem Cell Investig. 2023;10:4. doi:10.21037/sci-2022-038.

189. Birkl D, Quiros M, García-Hernández V, Zhou DW, Brazil JC, Hilgarth R, et al. TNFα promotes mucosal wound repair through enhanced platelet activating factor receptor signaling in the epithelium. Mucosal Immunol. 2019;12:909–18. doi:10.1038/s41385-019-0150-8.

190. Majeed H, Gupta V. StatPearls: Adverse Effects of Radiation Therapy. Treasure Island (FL); 2023.

191. Park SH, Kang JO. Basics of particle therapy I: physics. Radiat Oncol J. 2011;29:135–46. doi:10.3857/roj.2011.29.3.135.

192. Kuess P, Böhlen TT, Lechner W, Elia A, Georg D, Palmans H. Lateral response heterogeneity of Bragg peak ionization chambers for narrow-beam photon and proton dosimetry. Phys Med Biol. 2017;62:9189–206. doi:10.1088/1361-6560/aa955e.

193. Lohberger B, Glänzer D, Eck N, Stasny K, Falkner A, Leithner A, Georg D. The ATR Inhibitor VE-821 Enhances the Radiosensitivity and Suppresses DNA Repair Mechanisms of Human Chondrosarcoma Cells. Int J Mol Sci 2023. doi:10.3390/ijms24032315.

194. Yamada S, Takiyama H, Isozaki Y, Shinoto M, Makishima H, Yamamoto N, Tsuji H. Carbon-ion Radiotherapy for Colorectal Cancer. J Anus Rectum Colon. 2021;5:113–20. doi:10.23922/jarc.2020-082.

195. Ghaderi N, Jung J, Brüningk SC, Subramanian A, Nassour L, Peacock J. A Century of Fractionated Radiotherapy: How Mathematical Oncology Can Break the Rules. Int J Mol Sci 2022. doi:10.3390/ijms23031316.

196. Saito T, Yamaguchi K, Toya R, Oya N. Single- Versus Multiple-Fraction Radiation Therapy for Painful Bone Metastases: A Systematic Review and Meta-analysis of Nonrandomized Studies. Adv Radiat Oncol. 2019;4:706–15. doi:10.1016/j.adro.2019.06.003.

197. Peters C, Vandewiele J, Lievens Y, van Eijkeren M, Fonteyne V, Boterberg T, et al. Adoption of single fraction radiotherapy for uncomplicated bone metastases in a tertiary centre. Clin Transl Radiat Oncol. 2021;27:64–9. doi:10.1016/j.ctro.2021.01.004.

198. Pacheco R, Stock H. Effects of radiation on bone. Curr Osteoporos Rep. 2013;11:299–304. doi:10.1007/s11914-013-0174-z.

199. Krasin MJ, Constine LS, Friedman DL, Marks LB. Radiation-related treatment effects across the age spectrum: differences and similarities or what the old and young can learn from each other. Semin Radiat Oncol. 2010;20:21–9. doi:10.1016/j.semradonc.2009.09.001.

200. Hartley KA, Li C, Laningham FH, Krasin MJ, Xiong X, Merchant TE. Vertebral body growth after craniospinal irradiation. Int J Radiat Oncol Biol Phys. 2008;70:1343–9. doi:10.1016/j.ijrobp.2007.08.085.

201. Mizumoto M, Oshiro Y, Pan H, Wang F, Kaste SC, Gajjar A, et al. Height after photon craniospinal irradiation in pediatric patients treated for central nervous system embryonal tumors. Pediatr Blood Cancer. 2020;67:e28617. doi:10.1002/pbc.28617.

202. Margulies BS, Horton JA, Wang Y, Damron TA, Allen MJ. Effects of radiation therapy on chondrocytes in vitro. Calcif Tissue Int. 2006;78:302–13. doi:10.1007/s00223-005-0135-3.

203. Chen H, Tan X-N, Hu S, Liu R-Q, Peng L-H, Li Y-M, Wu P. Molecular Mechanisms of Chondrocyte Proliferation and Differentiation. Front Cell Dev Biol. 2021;9:664168. doi:10.3389/fcell.2021.664168.

204. Garrison P, Yue S, Hanson J, Baron J, Lui JC. Spatial regulation of bone morphogenetic proteins (BMPs) in postnatal articular and growth plate cartilage. PLoS One. 2017;12:e0176752. doi:10.1371/journal.pone.0176752.

205. Nilsson O, Parker EA, Hegde A, Chau M, Barnes KM, Baron J. Gradients in bone morphogenetic protein-related gene expression across the growth plate. J Endocrinol. 2007;193:75–84. doi:10.1677/joe.1.07099.

206. Matsuoka K, Park K-A, Ito M, Ikeda K, Takeshita S. Osteoclast-derived complement component 3a stimulates osteoblast differentiation. J Bone Miner Res. 2014;29:1522–30. doi:10.1002/jbmr.2187.

207. Donaubauer A-J, Deloch L, Becker I, Fietkau R, Frey B, Gaipl US. The Influence of Radiation on Bone and Bone Cells-Differential Effects on Osteoclasts and Osteoblasts. Int J Mol Sci 2020. doi:10.3390/ijms21176377.

208. Ota N, Takaishi H, Kosaki N, Takito J, Yoda M, Tohmonda T, et al. Accelerated cartilage resorption by chondroclasts during bone fracture healing in osteoprotegerin-deficient mice. Endocrinology. 2009;150:4823–34. doi:10.1210/en.2009-0452.

209. Xiong J, Onal M, Jilka RL, Weinstein RS, Manolagas SC, O'Brien CA. Matrix-embedded cells control osteoclast formation. Nat Med. 2011;17:1235–41. doi:10.1038/nm.2448.

210. Wang B, Jin H, Shu B, Mira RR, Di Chen. Chondrocytes-Specific Expression of Osteoprotegerin Modulates Osteoclast Formation in Metaphyseal Bone. Sci Rep. 2015;5:13667. doi:10.1038/srep13667.

211. Kearns AE, Khosla S, Kostenuik PJ. Receptor activator of nuclear factor kappaB ligand and osteoprotegerin regulation of bone remodeling in health and disease. Endocr Rev. 2008;29:155–92. doi:10.1210/er.2007-0014.

212. Huang W, Yang S, Shao J, Li Y-P. Signaling and transcriptional regulation in osteoblast commitment and differentiation. Front Biosci. 2007;12:3068–92. doi:10.2741/2296.

213. Chandra A, Lin T, Tribble MB, Zhu J, Altman AR, Tseng W-J, et al. PTH1-34 alleviates radiotherapy-induced local bone loss by improving osteoblast and osteocyte survival. Bone. 2014;67:33–40. doi:10.1016/j.bone.2014.06.030.

214. Chandra A, Lin T, Zhu J, Tong W, Huo Y, Jia H, et al. PTH1-34 blocks radiation-induced osteoblast apoptosis by enhancing DNA repair through canonical Wnt pathway. J Biol Chem. 2015;290:157–67. doi:10.1074/jbc.M114.608158.

215. Guo C, Li C, Yang K, Kang H, Xu X, Xu X, Deng L. Increased EZH2 and decreased osteoblastogenesis during local irradiation-induced bone loss in rats. Sci Rep. 2016;6:31318. doi:10.1038/srep31318.